DISS. ETH No. 29154

High performance bifacial $Cu(In,Ga)Se_2$ solar cells with silver promoted low-temperature process

A thesis submitted to attain the degree of

DOCTOR OF SCIENCES of ETH ZURICH

(Dr. sc. ETH Zurich)

presented by

Shih-Chi Yang

M.Sc. in Electronics Engineering, National Taiwan University

born on 28.12.1989

citizen of Taiwan

accepted on the recommendation of

Prof. Dr. A. N. Tiwari, examiner

Prof. Dr. Marika Edoff, co-examiner

Prof. Dr. Jürg Leuthold, co-examiner

Dr. Romain Carron, co-examiner

2023

Contents

Abstract

The objective of this thesis is to develop high efficiency bifacial Cu(In,Ga)Se_2 (CIGS) thin film solar cells. Bifacial photovoltaics have a great potential to obtain higher annual energy yield by capturing the extra light reflected or diffused to the rear side. In addition, bifacial devices are attractive for a wide range of applications such as building-integrated photovoltaics (BIPV), vertically mounted bifacial PV (VBPV), and agrivoltaics. However, despite their potential, efficient bifacial CIGS devices have not yet been demonstrated, leaving their many applications in a state of stagnation, particularly in comparison to c-Si solar cells. Therefore, the development of efficient bifacial CIGS solar cells is critical for the advancement of these applications.

For CIGS solar cells in the monofacial configuration, opaque Mo back electrical contacts are commonly used. In a bifacial configuration, a transparent conducting oxide (TCO) is required to replace the Mo contact in order to collect the sunlight from the rear side. As a consequence, two major issues result in low efficiency in bifacial CIGS devices: first, the formation of the detrimental GaO_x interlayer at the CIGS/TCO interface during the high-temperature growth process of CIGS leads to a deterioration especially of the fill factor (FF). Second, the combination of the short diffusion length of carriers in CIGS absorbers and high recombination rate at the CIGS/TCO interface results in poor carrier collection under rear illumination, and therefore, low short circuit current density (J_{SC}). In this thesis, we develop a silver-promoted low-temperature growth process to tackle those long-standing challenges in bifacial CIGS devices.

Chapter 3 focuses on understanding the influence of [Ga]/([Ga] + [In]) (GGI) back grading height (ΔGGI) on open circuit voltage (V_{OC}) deficit and device performance of

the CIGS solar cells. We intentionally modified the Ga and In evaporation rates during the first stage of the multi-stage CIGS deposition process to tailor back grading profiles. Time-resolved photoluminescence (TRPL) carrier lifetime and V_{OC} deficit present a high dependency on ΔGGI. A ΔGGI value of around 0.5 is required to effectively suppress the back interface recombination, highlighting the importance of the grading control in high-performance CIGS solar cells.

Chapter 4 aims to reveal the influence of alloying Ag into CIGS on the absorber quality and device performance. The Ag precursor layer method was chosen for its simplicity and potential for easy implementation into existing CIGS co-evaporation equipment in research labs or in the industry. The thickness of Ag precursor layer is optimized based on the device performance. Different material characterization techniques were performed to correlate the device performance and the material properties of absorbers, including scanning electron microscopy (SEM), TRPL, secondary ion mass spectrometry (SIMS) and x-ray diffraction (XRD). By adding a small amount of Ag (less than 5% in [Ag]/([Ag] + [Cu])), larger grain size and enhanced inter-diffusion of group-III elements in CIGS absorbers were observed.

Chapter 5 focuses on reducing the absorber deposition temperature while maintaining high material quality of the CIGS absorbers. By adding a small amount of Ag (about 4% - 5% in AAC) with the precursor layer method, the process temperature window of high-quality absorber depositions is widened by around 50 °C. Power conversion efficiencies (PCEs) of 19.6% and 18.5% were achieved with nominal substrate temperatures (T_{sub}) of 353 °C and 303 °C, respectively (baseline T_{sub} in 450-600 °C range delivering efficiencies of about 20%). High PCEs for such low-temperature grown CIGS devices are mainly driven by less V_{OC} degradation. The role of Ag in widening deposition process window is investigated by characterization techniques such as TRPL, capacitance-voltage (CV), and SIMS.

Chapter 6 aims at the development of high performance bifacial CIGS solar cells. With the help of Ag alloying, an optimal T_{sub} of around 350 °C strikes a good balance between ITO/CIGS interface properties, absorber quality, suitable GGI gradient, and better optical

properties in ITO back contact. A record cell was obtained with efficiencies of 19.77% and 10.89% under front and rear one sun illumination, as independently certified by Fraunhofer ISE. Moreover, direct fabrication of bifacial CIGS solar cells on flexible substrates is demonstrated for the first time. The long-term impact of this work is illustrated by the demonstration of the first bifacial perovskite/CIGS tandem solar cell in a 4-terminal configuration, achieving a power generation density of 28.0 mW/cm^2 $BiFi_{300}$ with a gain of 8.9 mW/cm^2 as compared to the performance of the stand-alone CIGS cell.

In summary, this thesis presents an innovative approach to enhance power generation densities of bifacial CIGS solar cells, achieved through the use of a silver-promoted low-temperature process and a modified multi-stage co-evaporation process. The study delves extensively into the effects of Ga back gradings and Ag alloying on the material properties and device performance of CIGS solar cells. Additionally, it explores various bifacial architectures, including flexible bifacial and bifacial perovskite/CIGS tandem devices, which hold promise for the development of the next generation of bifacial thin-film devices. These findings pave the way for future advancements in the field of solar technology.

Zusammenfassung (Abstract in German)

Ziel dieser Arbeit ist die Entwicklung hocheffizienter bifazialer Cu(In,Ga)Se_2 (CIGS) Dünnschichtsolarzellen. Bifaciale Photovoltaik hat ein großes Potenzial, um eine höhere jährliche Energieausbeute zu erzielen, indem sie das zusätzliche Licht einfängt, das auf der Rückseite reflektiert oder gestreut wird. Darüber hinaus sind bifaciale Solarzellen für eine Vielzahl von Anwendungen attraktiv, wie z. B. gebäudeintegrierte Photovoltaik (BIPV), vertikal montierte bifaciale Photovoltaik (VBPV) und Agri-Photovoltaik. Trotz ihres Potenzials konnten effiziente bifaciale CIGS-Solarzellen jedoch noch nicht nachgewiesen werden, so dass ihre zahlreichen Anwendungen, insbesondere im Vergleich zu c-Si-Solarzellen, stagnieren. Daher ist die Entwicklung effizienter bifazialer CIGS-Solarzellen von entscheidender Bedeutung für die Weiterentwicklung dieser Anwendungen.

Für CIGS-Solarzellen in monofacialer Konfiguration werden in der Regel undurchsichtige elektrische Rückseitenkontakte aus Mo verwendet. In einer bifacialen Konfiguration ist ein transparentes leitendes Oxid (TCO) erforderlich, um den Mo-Kontakt zu ersetzen und das Sonnenlicht von der Rückseite zu sammeln. Infolgedessen führen zwei Hauptprobleme zu einem niedrigen Wirkungsgrad in bifacialen CIGS-Bauelementen: Erstens führt die Bildung der schädlichen GaO_x-Zwischenschicht an der CIGS/TCO-Grenzfläche während des Hochtemperatur-Wachstums von CIGS zu einer Verschlechterung insbesondere des Füllfaktors (FF). Zweitens führt die Kombination aus der kurzen Diffusionslänge von Ladungsträgern in CIGS-Absorbern und der hohen Rekombinationsrate an der CIGS/TCO-Grenzfläche zu einer schlechten Ladungsträgersammlung bei rückwärtiger Beleuchtung und damit zu einer niedrigen Kurzschlussstromdichte (J_{SC}). In dieser Arbeit entwickeln wir ein mittels Silber gefördertes Niedertemperatur-Wachstumsverfahren, um

diese seit langem bestehenden Probleme in bifacialen CIGS-Bauelementen zu lösen.

Kapitel 3 konzentriert sich auf Einflusses des [Ga]/([Ga] + [In]) (GGI) Gradienten am Rückkontakt (ΔGGI) auf das Leerlaufspannungsdefizit (V_{OC}) und die Bauelementleistung der CIGS-Solarzellen. Wir haben die Ga- und In-Verdampfungsraten während der ersten Stufe des mehrstufigen CIGS-Abscheidungsprozesses absichtlich verändert, um den Gradienten am Rückkontakt anzupassen. Die zeitaufgelöste Photolumineszenz (TRPL), die Lebensdauer der Ladungsträger und das V_{OC} Defizit zeigen eine starke Abhängigkeit von ΔGGI. Ein ΔGGI-Wert von etwa 0,5 ist erforderlich, um die Rekombination an der hinteren Grenzfläche wirksam zu unterdrücken, was die Bedeutung der Gradierungssteuerung in Hochleistungs-CIGS-Solarzellen unterstreicht.

Kapitel 4 zielt darauf ab, den Einfluss der Ag-Legierung in CIGS auf die Absorberqualität und die Solarzellenleistung zu untersuchen. Die Ag-Precursor-Schicht-Methode wurde aufgrund ihrer Einfachheit und ihres Potenzials für eine einfache Implementierung in bestehende CIGS-Co-Verdampfungsanlagen in Forschungslaboratorien oder in der Industrie verwendet. Die Dicke der Ag-Precursor-Schicht wird auf der Grundlage der Bauelementleistung optimiert. Es wurden verschiedene Materialcharakterisierungstechniken durchgeführt, um die Geräteleistung und die Materialeigenschaften der Absorber zu korrelieren, einschließlich Rasterelektronenmikroskopie (SEM), TRPL, Sekundärionenmassenspektrometrie (SIMS) und Röntgenbeugung (XRD). Durch Zugabe einer geringen Menge Ag (weniger als 5% in [Ag]/([Ag]+[Cu])) wurden eine größere Korngröße und eine verbesserte Interdiffusion von Elementen der Gruppe III in CIGS-Absorbern beobachtet.

Kapitel 5 konzentriert sich auf die Senkung der Absorberabscheidungstemperatur unter Beibehaltung der hohen Materialqualität der CIGS-Absorber. Durch die Zugabe einer geringen Menge Ag (ca. 4% - 5% in AAC) mit der Precursor-Schicht-Methode wird das Prozesstemperaturfenster für hochwertige Absorberabscheidungen um ca. 50 °C vergrößert. Bei nominalen Substrattemperaturen (T_{sub}) von 353 °C bzw. 303 °C wurden Energieumwandlungswirkungsgrade (PCEs) von 19,6% bzw. 18,5% erreicht (Basis-T_{sub} im Bereich von 450-600 °C liefert Wirkungsgrade von etwa 20%). Hohe PCEs für solche bei niedrigen Temperaturen gewachsenen CIGS-Bauelemente sind hauptsächlich auf eine geringere V_{OC}-

Degradation zurückzuführen. Die Rolle von Ag bei der Erweiterung des Abscheidungsfensters wird durch Charakterisierungstechniken wie TRPL, Kapazitäts-Spannungs (CV) und SIMS untersucht.

Kapitel 6 zielt auf die Entwicklung leistungsstarker bifazialer CIGS-Solarzellen ab. Mit Hilfe einer Ag-Legierung wird mit einem optimalen T_{sub} von etwa 350 °C ein gutes Gleichgewicht zwischen ITO/CIGS-Grenzflächeneigenschaften, Absorberqualität, geeignetem GGI-Gradienten und besseren optischen Eigenschaften im ITO-Rückkontakt erreicht. Es wurde eine Rekordzelle mit Wirkungsgraden von 19,77% und 10,89% bei Beleuchtung mit einer Sonne von vorne und hinten erzielt, was vom Fraunhofer ISE unabhängig bestätigt wurde. Darüber hinaus wurde erstmals die direkte Herstellung von bifacialen CIGS-Solarzellen auf flexiblen Substraten zum ersten Mal gezeigt. Die langfristige Auswirkung dieser Arbeit wird veranschaulicht durch die Demonstration der ersten bifacialen Perowskit/CIGS -Tandemsolarzelle in einer 4-Terminal Tandemsolarzelle in einer 4-Terminal-Konfiguration, die eine Stromerzeugungsdichte von 28,0 mW/cm^2 $BiFi_{300}$ mit einer Verstärkung von 8,9 mW/cm^2 im Vergleich zur Leistung der eigenständigen CIGS-Zelle.

Zusammenfassend wird in dieser Arbeit ein innovativer Ansatz zur Erhöhung der Stromerzeugungsdichte von bifazialen CIGS-Solarzellen vorgestellt, der durch den Einsatz eines silbergeförderten Niedertemperaturprozesses und eines modifizierten mehrstufigen Co-Verdampfungsprozesses erreicht wird. Die Studie befasst sich eingehend mit den Auswirkungen von unterschiedlichen Ga Rückgradienten und Ag-Legierungen auf die Materialeigenschaften und die Leistung von CIGS-Solarzellen. Darüber hinaus werden verschiedene bifaziale Architekturen untersucht, darunter flexible bifaziale und bifaziale Perowskit/CIGS-Tandem-Bauelemente, die vielversprechend für die Entwicklung der nächsten Generation von bifazialen Dünnschicht-Bauelementen sind. Diese Erkenntnisse ebnen den Weg für künftige Fortschritte im Bereich der Solartechnik.

List of abbreviations

AM1.5G	Reference global spectrum at air mass 1.5
ARC	Anti reflective coating
CBD	Chemical bath deposition
CGI	Absorber [Cu]/([Ga]+[In]) ratio
CIGS	CuIn1-xGaxSe2
CV	Capacitance-voltage
EQE	External quantum efficiency
FWHM	Full width half maximum
GGI	Absorber [Ga]/([Ga]+[In]) ratio
IQE	Internal quantum efficiency
ICP-MS	Inductively coupled plasma mass spectrometry
JV	Current density-voltage
PV	Photovoltaics
PDT	Post deposition treatment
PI	Polyimide
SEM	Scanning electron microscopy
SLG	Soda-lime glass
SIMS	Secondary-ion mass spectrometry
TEM	Transmission electron microscopy

TCO	Transparent conductive oxide
XPS	X-ray photoelectron spectroscopy
XRF	X-ray fluorescence

1 Introduction

1.1 The need for renewable energy

The goal of limiting global warming to 1.5°C above pre-industrial levels and reducing greenhouse gases to net zero by 2050 is well-recognized [1]. The transition to energy production by renewable sources is seen as a necessary phase of human development. Photovoltaics (PV) is an important source of renewable energy because it allows generating electricity from a clean, abundant, and renewable source: the sun. Figure 1.1 shows the expected energy supply from International Energy Agency (IEA) for net-zero emission scenario by 2050 [2]. PV is expected to play an important role in facilitating the transition to a low-carbon economy, mitigating climate change, and meeting energy demands [3].

PV market has grown rapidly, and between 2008 and 2020 the global solar PV power generation increased from 11.9 TWh to 821 TWh [4]. Currently Si based PV technology is clearly dominating the PV market, however thin film technologies based on absorbers such as CdTe, Kesterite, and $Cu(In, Ga)Se_2$ (CIGS) have distinct advantages over silicon-based technologies. They are potentially low cost because of lower amount of materials needed, and compatible with scalable high-throughput deposition methods like sputtering and evaporation.

As a leading thin film technology, CIGS offers excellent durability and manufacturability. Of particular relevance is the possibility to deposit CIGS on flexible substrates, which enables the production of lightweight and flexible modules by roll-to-roll manufacturing [5]. The current world record for laboratory-scale small area CIGS solar cells is 23.35% on glass substrates by using two-step high temperature sulfurization after selenization (SAS)

process from the Japanese company Solar Frontier [6]. An efficiency of 22.6% was obtained by using a high temperature multi-stage co-evaporation process from ZSW [6]. The highest large-area module efficiency is 19.8% with aperture area of 665 cm^2 by Avancis [7]. The record efficiency for low-temperature co-evaporated CIGS on a flexible substrate is 22.2% [8] by Empa.

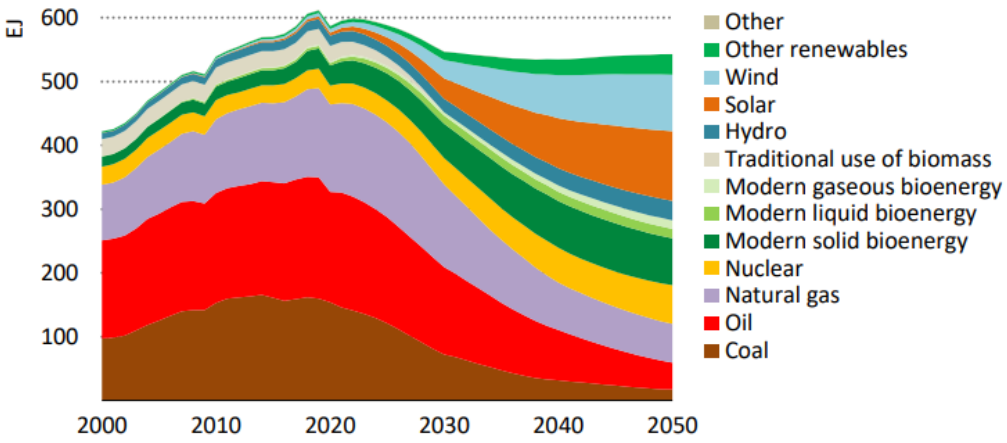

Figure 1.1: Global historical and projected data of energy supply for the Net-Zero Emissions by 2050 scenario. Reproduced from IEA [2].

1.2 CIGS solar cells

1.2.1 Architecture of CIGS solar cells

Solar cells with a CIGS absorber layer typically have a substrate configuration. The basic architecture of a CIGS solar cell is shown in Figure 1.2. The structure is composed of a rigid or flexible substrate, a Mo or ITO back electrical contact, the CIGS absorber layer, a thin n-type wide-bandgap semiconductor layer, transparent front contacts and metal grids, and optionally a MgF_2 anti-reflective coating. The total thickness excluding the substrates is about $3-5\,\mu m$

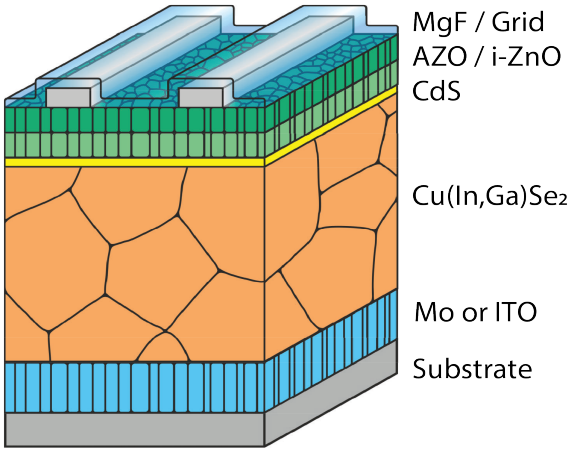

Figure 1.2: Device structure of CIGS solar cells in a monofacial (with Mo back electrical contact) and a bifacial (with ITO back electrical contact) configuration in this thesis.

1.2.2 Crystal structure, phase and defect chemistry

CIGS semiconductor belongs to a ternary system since In and Ga share the same site in the lattice. As a result, phase diagrams of Cu-In-Se and Cu-Ga-Se show similar existence ranges of phases with the same crystal structures and comparable temperature dependencies [9], despite some differences. For the purposes of the simplification, the Cu-In-Se system is discussed in this section.

Figure 1.3 shows the ternary Cu-In-Se phase diagram (adatpted from various sources and [10]). The isopleth along the Cu_2Se-In_2Se_3 line corresponds to the situation in which Cu has an oxidation state of I and In has an oxidation state of III. The phase mainly used for PV applications is α-$CuInSe_2$ with a chalcopyrite crystal structure, which also belongs to the Cu_2Se-In_2Se_3 isopleth.

The Cu_2Se-In_2Se_3 isopleth is a pseudobinary system [11], i.e. along this line three-phase equilibria are reduced at all temperatures to two-phase equilibria, whereby each composition along the system can be represented as linear combination of two boundary compositions, which is known as the level rule. A simplified phase diagram constructed by the temperature dependence along this line is shown in Figure 1.4.

The α-$CuInSe_2$ phase lying at the center of the phase diagram belongs to a tetragonal

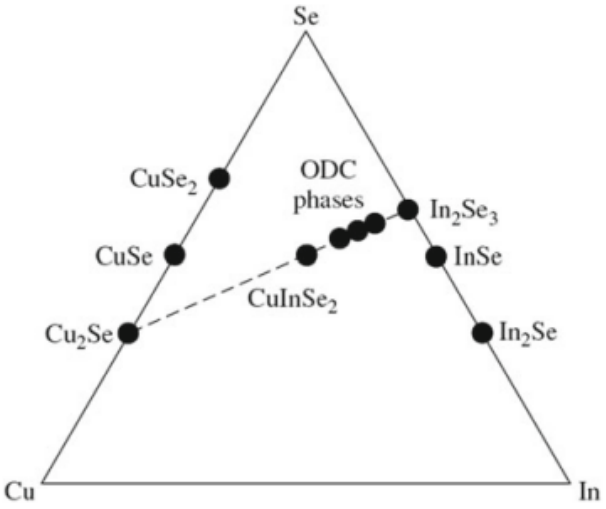

Figure 1.3: Ternary phase diagram of the Cu-In-Se system with a cut along the Cu_2Se - In_2Se_3 isopleth. Reproduced from Zhong et al. [10]

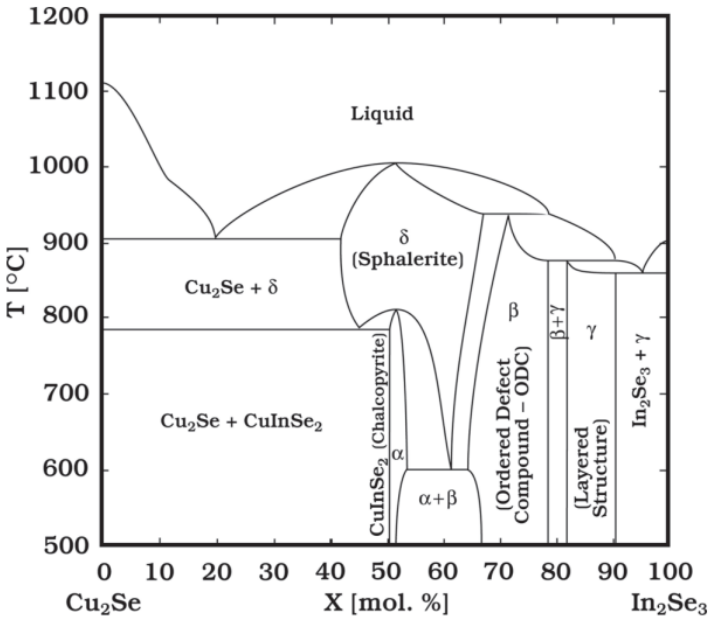

Figure 1.4: Phase diagram constructed on the Cu_2Se-In_2Se_3 pseudobinary line. Reproduced from Stanbery et al. [12]

crystal system (Figure 1.5) where each Se atom is bound tethraedrically to two Cu and two In atoms, and each metal atom is bound to four Se atoms [12, 13]. Since Se has a larger electronegativity than both Cu and In, the negative charge are partially shifted away from the metal [14]. As a result, Se is referred to as the chalcogen anion and Cu and In as the

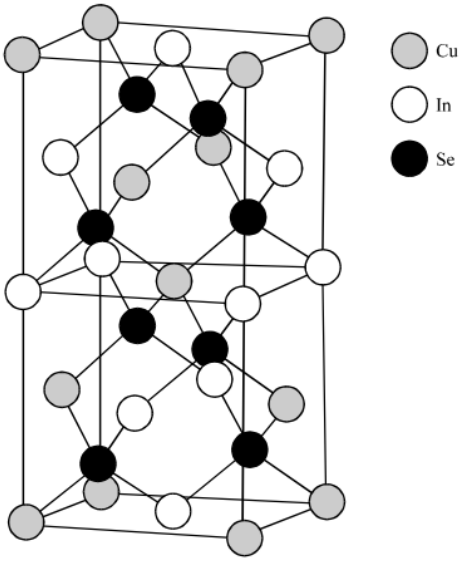

Figure 1.5: Unit cell of Cu_2Se. Reproduced from Amin et al. [13]

metal cations. The α-$CuInSe_2$ and α-$CuGaSe_2$ phases exhibit complete miscibility in a wide range of Ga to In ratios [15, 16].

As shown in Figure 1.4, the α phase is maintained in a certain narrow range of Cu poor compositions. The α phases can tolerate large amounts of Cu deficiency due to the relative weakness of the Cu-Se bond as respect to the In-Se bond [17]. The β phases corresponds to Cu-poor compositions and maintains the tetragonal crystal of the α phase, but includes a large number of point defects accommodating the lack of Cu atoms. Such defects are Cu vacancies V_{Cu}, In_{Cu} antisites and defect complexes formed by two negatively charged V_{Cu}^{-} and one positively charged In_{Cu}^{2+}[17]. A periodic arrangement of this defect complex leads to phases typically reported in literature as "ordered defect compound"(ODC) [18]. ODCs have, by definition, a well defined set of Cu-poor composition with stoichiometries defined by the concentration of the $2(V_{Cu}^{-})$-In_{Cu}^{2+} defect complex. It was however noted that, at least when $CuInSe_2$ is alloyed with $CuGaSe_2$, Cu-poor CIGS phases do not always have such well defined compositions, but rather a smooth transition from stoichiometric to Cu-poor [16]. Below a certain Cu threshold concentration, corresponding to approximately 9 at.% (i.e. the composition of the ODC $CuIn_3Se_5$), the structure turns to hexagonal layered (phase), similar to the one of pure In_2Se_3 [19].

The existence of the α phase is limited to an upper bound of Cu concentration about 24.5 at.%. A higher Cu concentration results in the segregation of $Cu_{2-x}Se$ phases [20]. The segregation of $Cu_{2-x}Se$ is possible even below the stoichiometric Cu concentration of 25 at.%, which can be explained by the spontaneous creation of $2(V_{Cu}^{-})$-In_{Cu}^{2+} defect complexes (with very low or even negative formation energies [18]).

Since copper vacancy V_{Cu} in CIGS has a very low formation energy and is a shallow acceptor (20-30 meV above the valence band) [17], it is thus considered the main responsible defect for p-type doping of CIGS. On the other hand, In_{Cu} antisite is the main compensating donor [21] in CIGS. A large concentration of $2(V_{Cu}^{-})$-In_{Cu}^{2+} complexes, as well as other charged defects, results in a high degree of compensation. However, the p-type doping is typically dominant due to the lower formation energy of the V_{Cu}.

1.2.3 Optoelectronic properties

CIGS is a direct bandgap semiconductor with both the valence band maximum (VBM) and the conduction band minimum (CBM) located at the Γ-point. The VBM is composed of Cu 3d and Se 4p anti-bonding orbitals. Group-III states are located deeper into the VB. Therefore, the VBM is thus only marginally affected by the [Ga]/([Ga]+[In]) ratio (GGI). On the other hand, the CBM is mainly composed of group-III 5s and Se 4p bonding orbitals. As a consequence, GGI has a strong impact on the CBM position, which in turn affects the bandgap energy E_g [22, 23, 24]. Carron et al. [25] have proposed a relation between E_g and the composition, expressed by the following equation:

$$E_g = 1.004 \times (1 - \mathrm{GGI}) + 1.663 \times \mathrm{GGI} - 0.033 \times \mathrm{GGI} \times (1 - \mathrm{GGI}) \tag{1.1}$$

In addition, the dispersion relation of the VB (and to a lower extent also the CB) deviates from a parabolic behavior [26]. Therefore, the dependency of the absorption coefficient α on the photon energy $h\nu$ can be approximated with a square-root relation ($\alpha \propto \sqrt{h\nu - Eg}$) only in a very narrow energy range of approximately 0.15 eV above E_g. Absorption coefficients have values of 10^3 cm^{-1} to 10^4 cm^{-1} in a range of ±0.1 eV around

E_g, and beyond 10^4 cm^{-1} at photon energies 0.4 eV above E_g [25]. Moreover, CIGS absorbs in wide exponential (Urbach) tails below the bandgap energy (the exact value may also depend on the choice of the experimental method used for quantification [25]).

1.2.4 CIGS by co-evaporation methods: a brief history

The first deposition of $CuInSe_2$ thin films by evaporation aiming to develop solar cells was reported in 1976 by Kazmerski et al. [27]. The method involves the single-source evaporation of a $CuInSe_2$ powder precursor and further annealing in H_2Se. Later a refinement of the co-evaporation process was introduced by BOEING in 1980 [28]. The process consisted in the evaporation of slightly copper-rich material followed by copper-poor material (bi-layer process) as long as needed in order to obtain an overall Cu-poor composition. Further results revealed that the advantages of the bi-layer process were related to film growth in the presence of segregated Cu-Se phases, which promote the formation of polycrystalline films with large grains with a low density of structural defects [29]. In 1982, Ga was added to the BOEING recipe (see [30] and references herein). The bi-layer process was used for more than one decade for the growth of highly efficient thin films. In 1994, for the first time Gabor et al. [31] introduced the three-stage deposition process. It consisted of a first co-evaporation of $(In, Ga)_2Se_3$ precursors (first stage), an addition of copper selenide until the film turned Cu-rich (second stage), and a final addition of $(In, Ga)_2Se_3$ to make the overall composition again Cu-poor (third stage). The three-stage deposition process resulted in a decreased film roughness and an improved *GGI* grading.

A method for in-situ control of the film stoichiometry was introduced by Kohara et al. [32], who found that the temperature of the film decreased at the first Cu-poor to Cu-rich transition. This was later explained by the change in thermal emissivity of the film due to the surface segregation of Cu-Se phases [33]. In-situ stoichiometry control is thus possible by monitoring the change in substrate temperature at the first Cu-poor to Cu-rich transition, which is known as "end-point detection". The discovery of the end-point-detection method paved the way for the development of more complex deposition sequences [34, 35]. For instance, the multi-stage co-evaporation processes employed at

Empa involves an additional Ga evaporation in the second stage, in order to improve the indium to gallium grading profiles for processes at low deposition temperatures [36].

1.2.5 Evolution of crystalline phase during three-stage processes

The evolution of phases and microstructure during three-stage co-evaporation has been widely studied by the group of Mainz et al. [37] using in-situ analysis by various X-ray based methods during growth. The schematic representation of a three-stage deposition process is shown in Figure 1.6. During the first deposition stage, In and Ga are evaporated in a Se overpressure environment with substrate temperatures between 300 °C and 400 °C. The phase formed is $(In, Ga)_2Se_3$ and its crystal structure depends on the relative amount of Ga. In case of Ga-free films, γ-In_2Se_3 (hexagonal layered) is formed. Pure Ga_2Se_3 crystallizes in the α phase, which has a cubic Se sublattice [37]. $(In, Ga)_2Se_3$ may grow as a mixture of the two phases [38].

During the second deposition stage, the substrate temperature is increased, the In and Ga evaporation is strongly reduced or even interrupted, and Cu is evaporated on the film surface. Cu diffuses into the $(In, Ga)_2Se_3$ and a phase transformation gradually occurs. The phase evolution follows the $(In, Ga)_2Se_3$-Cu_2Se pseudobinary line, until the formation of tetragonal α-$Cu(In, Ga)Se_2$. The structure of Ga_2Se_3 is not substantially modified, having already a cubic Se sublattice, and only the lattice spacing increases as a consequence of the addition of Cu. The structure of In_2Se_3 is strongly modified following the evolution γ-In_2Se_3 (hexagonal layered) - γ-$CuIn_5Se_8$ (hexagonal layered, Cu conc. 10 at.%) - β-$CuIn_3Se_5$ (defect tetragonal, Cu conc. 18 at.%) - α-$CuInSe_2$ (tetragonal, Cu conc. 25 at.%) [37]. These structural transformations result in the accumulation of a high density of planar defects (stacking faults) and of compressive stress in the final α-$CuInSe_2$ [37, 39].

Further Cu addition beyond a concentration of approximately 25 at.% results in the segregation of cubic $Cu_{2-x}Se$. The segregation of Cu-Se phases on the surface is controlled by the end-point detection. The Cu-poor to Cu-rich transition is also accompanied by a re-crystallization of the CIGS film, i.e. the formation of larger, differently oriented grains with a lower defect density [34]. The specific mechanism for the growth of larger grains

does not appear to be fully understood.

Another major feature of the re-crystallization process is the decrease of the density of planar defects accumulated in the film during the second stage [37, 40]. The features indicating a high density of stacking faults, as measured by in-situ X-ray diffraction, disappear upon the re-crystallization at the Cu-poor to Cu-rich transition. This has also been proven by complementary ex-situ TEM measurements [39]. The reduction of the density of planar defects is achievable only in Cu-rich material independently of the substrate temperature. During the third stage, the Cu flux is interrupted and In and Ga are evaporated again on the film until the Cu-Se phases are consumed and the targeted integrated under-stoichiometric Cu concentration is reached.

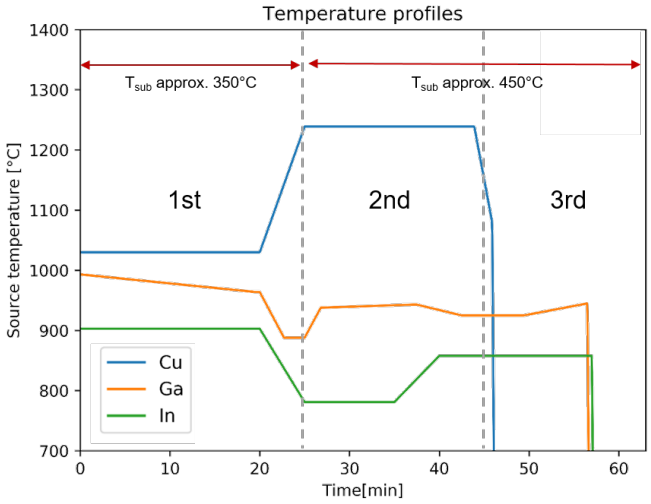

Figure 1.6: Schematic representation of a multi-stage deposition process with Cu, In, Ga and Se evaporation rates. Different stages of the three-stage process are marked by the dashed vertical lines.

1.2.6 Ga grading

State-of-the-art CIGS absorbers grown by co-evaporation normally have a varying In to Ga ratio throughout the thickness, implying a varying bandgap across the absorber. The concept of Ga back grading was first introduced by Contreras *et al.* [41]. Since this breakthrough, Ga back grading was widely investigated by both simulations and experiments.

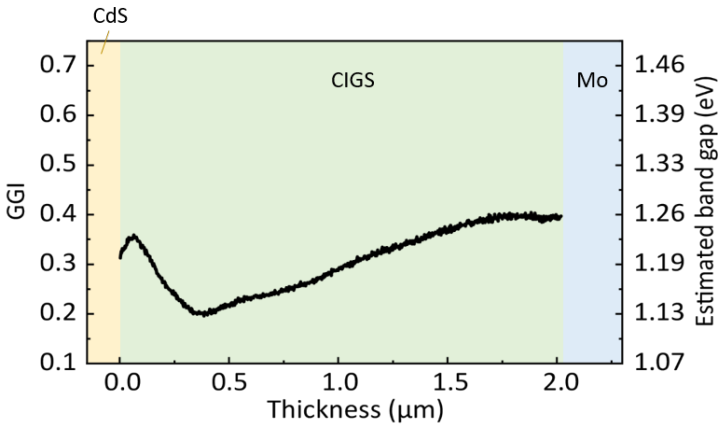

Figure 1.7: Typical double-graded GGI and bandgap profiles of a highly efficient CIGS solar cell, with larger GGIs towards the front and the back surfaces and a low-GGI region in the center-front. The region around the GGI minimum is referred to as grading notch.

A typical double-graded CIGS absorbers, the Ga concentration first decreases from the CdS/CIGS interface to a minimum inside the absorber, which is known as 'notch', and then increases towards the CIGS/Mo back interface. Figure 1.7 shows the GGI value change and the corresponding bandgap in a double-graded absorber from the standard three-stage co-evaporation process. How the grading and the notch are built will be detailed in Sec 2.1.3. The main advantage of a Ga grading towards the back surface is to assist the drift of free electrons towards the front junction. It suppresses back interface recombination and results in a significant enhancement in the open circuit voltage (V_{OC}) [42]. In addition, it was also shown that longer free carrier lifetimes as well as improved carrier collection and the open-circuit voltage can be achieved by introducing a single Ga back grading in the completed CIS devices [43]. One the other hand, the presence of a low bandgap notch region close to the front surface is important for the absorption of low-energy photons. And the the front gradings is crucial for better junction quality. A small conduction band offset (<0.03 eV) at the CdS/CIGS junction is reportedly beneficial for the interface quality, although a larger offset could result in a potential barrier for electrons and lead to increased interface recombination [44, 45, 46].

Following studies also showed the instrumental influence of notch position, the ratio of back and front grading heights [47, 48], and explored different defect models and doping concentrations [49].

1.2.7 Ag-alloyed CIGS

Recently, it has been extensively reported that Ag alloying in CIGS to form ACIGS can offer many interesting properties. First, it cahanges the opto-electronic properties of the chalcopyrite material by lowering both the valence band edge and the conduction band edge [50, 51], as shown in Figure 1.8(a). Second, silver chalcopyrites exhibit bandgaps about 0.2 eV wider than their Cu counterparts, as shown in Figure 1.8(b) [52]. It offers the potential of improving the device performance by the enhanced V_{OC}. Third, the melting points of silver chalcopyrites are about 200 °C lower than their Cu counterparts, suggesting that substitution of Cu by Ag in CIGS can lower the synthetic temperature. As a result, it improves crystallization [53], surface morphology, and thus resulting in better film quality of the absorber layer. In addition, less structural defect, and less sub-bandgap disorder [54] in ACIGS are also reported, which are linked to a lower melting point and enhanced elemental interdiffusion [55] with the presence of Ag. The resulting high V_{OC} and reduced V_{OC} deficit have drawn a lot of attention because of the potential for high efficiency ACIGS solar cells [56, 57, 58].

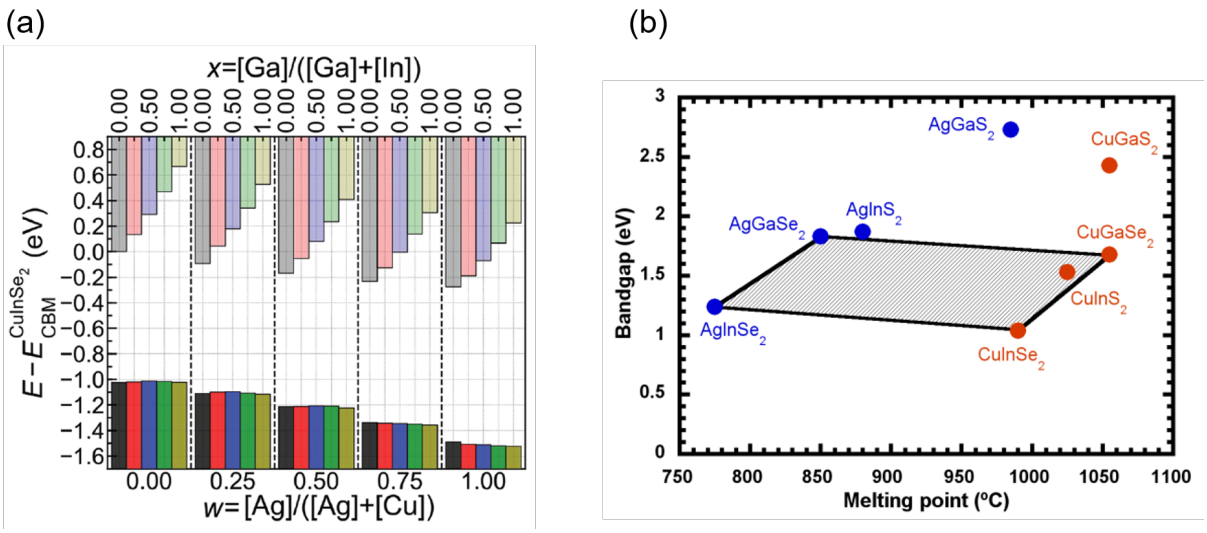

Figure 1.8: (a) Computed CBM and VBM levels of the ACIGS alloys with respect to CBM level of $CuInSe_2$. Reproduced from Ref. [51] (b) Bandgaps and melting points of ternary Ag- and Cu-chalcopyrites. Reproduced from Ref. [52]

1.2.8 Low-temperature CIGS deposition process

High efficiency CIGS solar cells typically require a substrate temperature ≥550 °C or higher for absorber depositions. High substrate temperature hinders the use of many types of flexible substrates because of their thermal stability, such that PI is the substrate of choice owing to its lightweight and compatibility to the process temperature up to about 450 °C.

Low temperature CIGS deposition process is compatible with the roll-to-roll processing, which is attractive for high-throughput manufacturing. By further reducing the process temperature, it shows the potentials of reducing the manufacturing costs and reducing the thermal-induced stress. Nevertheless, the best performance of CIGS solar cells grown at very low temperatures (≤400 °C) with the common three-stage process are so far not competitive (18.0 % at 390 °C [59], 12.4 % at 350 °C [60]). It is mainly because the thermal energy is needed for Cu diffusion, as well as to promote grain growth and annihilate defects [39, 60, 61]. Although single-stage low-temperature pulsed electron deposition (LTPED) can yield efficiencies up to 17.0 % at 250 °C [62, 63], this technique presents scale-up challenges and technical issues like the presence of micrometer-sized particle [64]. A simpler method with low temperature procress offering high performance and a potential for transferring from laboratory to manufacturing is therefore needed.

1.3 Basic model for pn-junction based PV devices.

Measurements of the current density as a function of the applied voltage (J-V) give access to the most relevant characteristic of a solar cell, the *conversion efficiency*. The efficiency is a measure for the share of irradiated power that is converted into electric power. The most conventional approach to estimate the device efficiency consists of a J-V measurement under simulated standard test conditions i.e. under a spectrum similar to the solar AM 1.5G spectrum with 1000 W/m^2 at a fixed temperature of 25 °C. Efficiencies measured under standardized conditions allow to compare measurements and to extrapolate the performance that can be expected under real world conditions. Figure 1.9 displays a typical J-V curve as measured on a CIGS thin film solar cell.

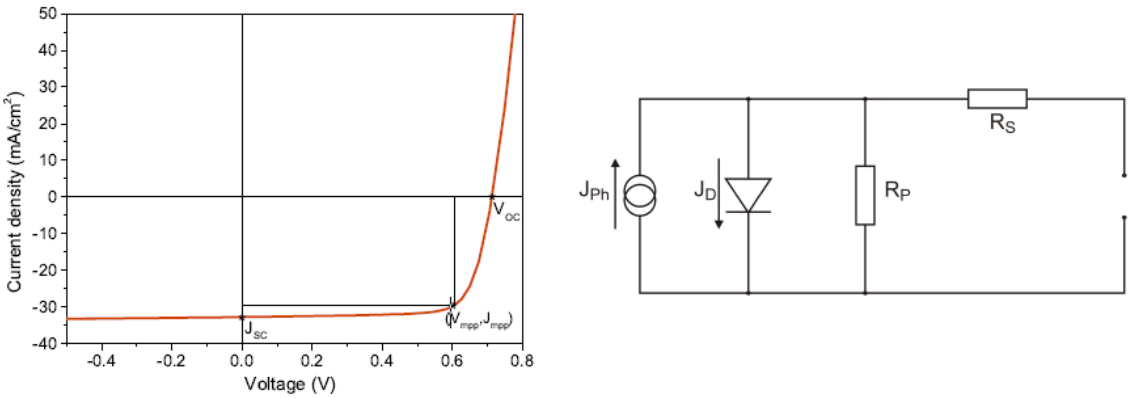

Figure 1.9: Left: Typical current density-voltage (J-V) measurement of a thin film $Cu(In, Ga)Se_2$ solar cell. The most relevant curve parameters i.e. short circuit current J_{SC}, open circuit voltage V_{OC}, maximum power point (mpp) voltage V_{mpp} and current J_{mpp} are indicated. Right: Single diode model describing the illuminated solar cell. Figures adapted from Ref. [65]

The J-V curve can be directly parametrized by a number of key parameters. Most importantly, it can be seen that at a voltage V_{mpp} and current density J_{mpp} the power provided by the device $P_{mpp} = V_{mpp} \times J_{mpp}$ reaches a maximum value. The efficiency is consequently defined as the P_{mpp} divided by the irradiated power (for AM 1.5G 100 $mWcm^{-2}$). Also the current density at closed circuit conditions J_{SC} (no potential drop between contacts) and the voltage at open circuit conditions V_{OC} (no net current measured) can be directly extracted from the measurement. A more rectangular JV curve allows a higher output power for which the fill factor $FF = P_{mpp}/(V_{OC} \times J_{SC})$ provides a simple measure.

More refined analysis of the J-V curves can be required not only to compare more subtle properties of the device, but also to compare to theoretically derived models for the diode behavior. In a basic approach the device is modeled by the so called single diode model as schematically shown in Figure 1.9. The J-V relation as measured on the electrodes can be approximately described by the expression:

$$J = J_0 \left(\exp\left(\frac{q(V - JR_s)}{Ak_BT} \right) - 1 \right) + \frac{V - JR_s}{R_p} - J_{ph}(V) \tag{1.2}$$

The parameters introduced so far, could be directly read from the J-V measurement. By further fitting of Eq. 1.2, additional parameters that characterize the device can be estimated. The parallel resistance R_{p} accounts for residual ohmic conduction and can be estimated from a non-illuminated measurement near zero bias. The series resistance R_{s} accounts for non-exponential increase of the device current in forward bias e.g. an ohmic resistance in the front contact can become the dominant contributor to the differential resistance at sufficient forward bias. There are other important parameters including the diode ideality factor A, the dark saturation current J_0 and the photo current J_{ph}.

1.4 Bifacial PV

1.4.1 Monofacial vs. bifacial

Increasing the power output per unit area of solar panels at low additional manufacturing costs is crucial for further lowering the PV-generated electricity price. One of the simplest strategies for increasing the power output density of a solar panel is to harvest the reflected and diffuse sunlight from the ground and the surroundings by employing bifacial designs, as shown in Figure 1.10. Compared with conventional monofacial-based PV systems, bifacial PVs have a strong potential to obtain higher annual energy yield. The benefits are especially attractive in applications such as building-integrated photovoltaics (BIPV) [66], vertically mounted bifacial PV (VBPV) [67], and agrivoltaics [68], which offer both low-carbon emission and low levelized cost of electricity (LCOE) [69, 70].

The concept of bifacial solar cells can date back to the 1960s, but the momentum to bring bifacial solar panels to the market has been gradually realized in the last decade as one of the latest technological advances in PV manufacturing [71]. The mainstream crystalline silicon (c-Si) PV module manufacturers are now producing bifacial silicon solar modules based on different cell technologies. The trend shows that bifacial solar cells and modules are increasingly important in today's PV market and may soon become the cost-effective PV standard. According to the International Technology Roadmap of PV (ITRPV), bifacial PV could capture 40% of the PV market by 2028 [70, 72].

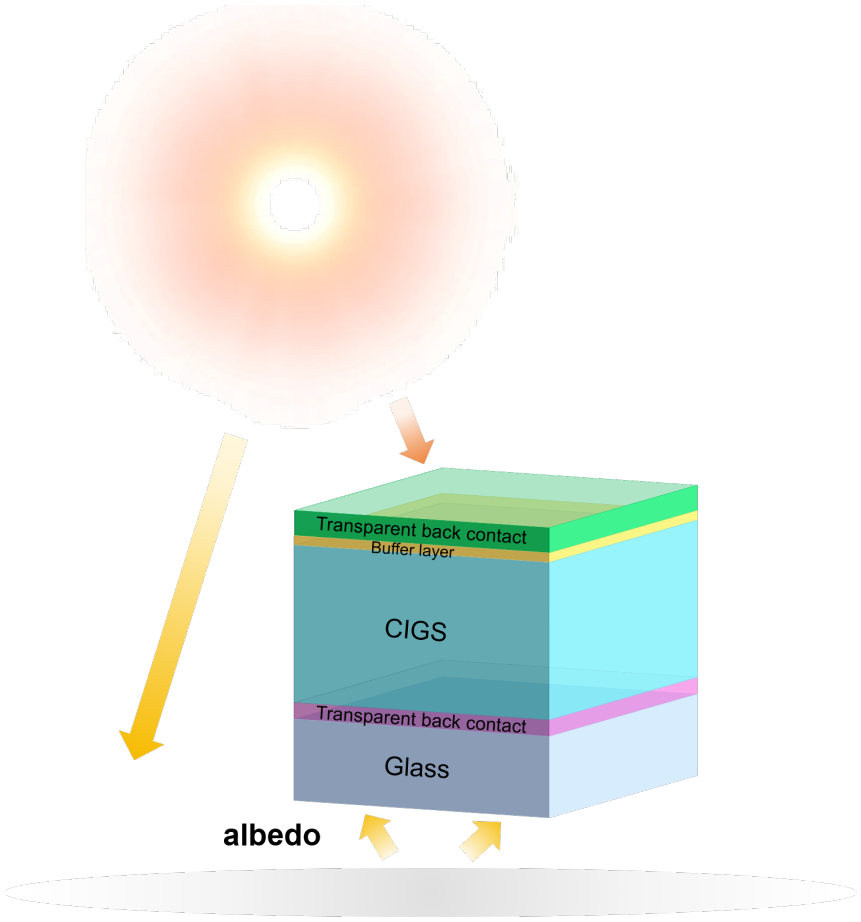

Figure 1.10: A schematic of a bifacial CIGS solar cell and the direct and albedo lights.

1.4.2 Challenges of bifaical CIGS solar cells

Si wafer based bifacial PV has reached industrial maturity and is widely used, while some preliminary research efforts have been made for bifacial thin-film solar cells. Unfortunately, the efficiency of bifacial CIGS thin-film solar cells has remained rather low whereas mono-facial CIGS cells with record efficiency of 23.35% [6] have been achieved on rigid glass substrates. The highest efficiency under one sun rear illumination doesn't exceed 7.1% and its efficiency under front illumination is just 9.0%.[73] As a consequence, bifacial CIGS solar cells and their various applications are still unattractive despite their great potential.

To collect the sunlight from the rear side, a transparent conductive oxide (TCO) is required to replace the conventionally used opaque Mo back contact in the mono-facial

configurations. However, the detrimental GaO_x is commonly formed at the CIGS/TCO interface during high-temperature growth process for absorber deposition. GaO_x is highly resistive and may form a reverse, second p-n junction at the back contact, which deteriorates especially the FF [74, 75]. Many efforts have been dedicated to suppressing GaO_x formation, but none of them were successful when it comes to device performance [75, 76, 77]. The highest reported efficiency with TCO back contact under front illumination is limited to merely 16.1% [77]. Therefore, the development of TCO-based devices including bifacial, semi-transparent, and ultra-thin rear-back-contact (RBC) devices remained stagnant.

On the other hand, very low efficiencies under rear illumination in bifacial CIGS devices are attributed to short diffusion length of carriers and high rear interface recombination. Commonly introduced Ga back gradients in CIGS absorbers can suppress the back interface recombination [78], but the required high Ga content results in poor absorber quality, and aggravates the formation of GaO_x interlayer. Moreover, the high-temperature CIGS deposition process also prevents strong Ga gradients due to increased elemental inter-diffusion. As a result, the bifaciality in CIGS devices is usually low. The use of ultra-thin absorbers can slightly mitigate the problem by bring the front interface closer to the space-charge region under rear illumination, but the efficiencies under front illumination are strongly compromised because of incomplete absorption of photons and higher impact of back interface recombination.

1.5 Aim of the thesis

The aim of this thesis is to develop high performance CIGS solar cells with low-temperature deposition process. It ensures the compatibility to the flexible substrates and opens the possibilities of different device architectures. In particular, four topics are covered:

- **Suppression of the back interface recombination:** the goal is to suppress the back interface recombination by introducing steeper and higher Ga back gradings in CIGS absorbers without sacrificing the absorber bulk quality. The influence of

Ga back grading height on V_{OC} and device performance would be investigated. The knowledge gained here is crucial for suppressing carrier recombination at rear interface in bifacial structures.

- **Improving material quality of CIGS absorbers:** the goal is so as to improve the material properties and the device performance of CIGS solar cells by alloying CIGS absorbers with Ag. The influence of Ag-alloying is further investigated with different material analysis techniques, including scanning electron microscopy, time-resolved photoluminescence, secondary ion mass spectrometry, X-ray diffraction, and Raman spectroscopy.

- **Reduction of the deposition process temperature:** the focus is to develop silver promoted low-temperature process to reduce the absorber deposition temperature while maintaining high quality CIGS absorbers. The role of Ag in reducing depostion process temperature will be investigated. The knowledge gained here is crucial for suppressing the formation of the GaO_x interlayer at CIGS/TCO interface in bifacial structures.

- **Development of high performance bifacial CIGS solar cells:** the goal is to reach high power generation density of the bifacial CIGS solar cells. We aim to take advantage of the modified co-evaporation process and silver-promoted low-temperature process to strike a good balance between CIGS/TCO interface properties, absorber quality, suitable Ga gradient and better optical properties of ITO back contact in bifacial devices. On top of that, the proof-of-concept of other promising device architectures would also be demonstrated, e.g. four-terminal bifacial perovskite/CIGS tandem solar cell and flexible bifacial CIGS devices.

2 Methodology

2.1 Multi-stage co-evaporation of CIGS

2.1.1 Deposition chamber setup

The CIGS absorbers have been deposited by multi-stage co-evaporation in an experimental setup originally designed for molecular beam epitaxy. The deposition chamber is shown in **Figure 2.1**. In the upper part of the chamber, a 5×5 cm^2 substrate is loaded on a rotating sample holder. The substrate temperature is controlled by a non-contacting thermocouple and a resistance heater placed beneath the substrate. The heater is powered by a proportional-integral-derivative controller (PID-controlled) power source. In the lower part of the chamber, Knudsen evaporation sources are disposed concentrically pointing towards the sample holder. The upper and lower parts of the chamber are separated by a main shutter. The base pressure in the chamber is approximately 4×10^{-7} mbar.

There are six evaporation sources containing six elements or compounds: Cu, In, Ga, Se, NaF and RbF, which are contained in crucibles made of pyrolytic boron nitride (except for Se-steel, and RbF-graphite). The Cu, In and Ga sources have a dual filament design with separate lip and bottom heatings. The evaporation rate is mainly controlled by the bottom temperature. The lip temperature is kept 100 °C to 200 °C above the bottom temperature to avoid material re-deposition near the lip. The Cu, In, Ga bottoms and the

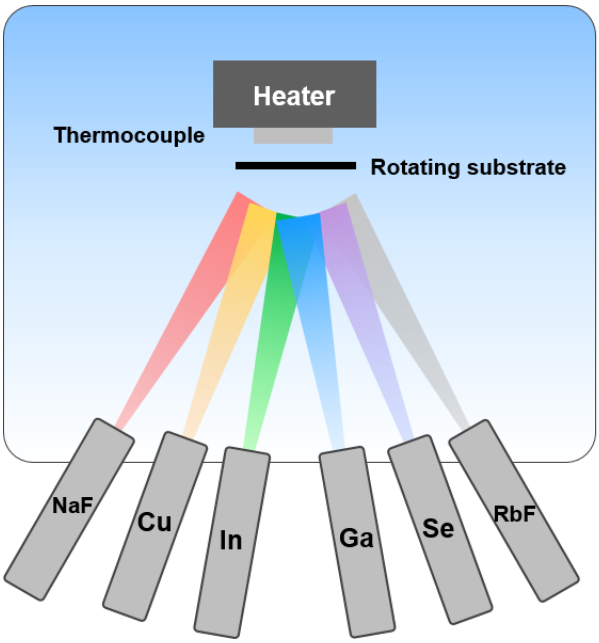

Figure 2.1: Schematic design of the deposition setup used for CIGS absorbers.

NaF source are heated by PID-controlled power sources while the Se, the RbF sources, and the lips are controlled by manually adjusting the current output of the power sources.

2.1.2 Source temperature vs. deposition rates

The temperature and the vapor pressures for each source can be related by the semi-empirical Antoine equation:

$$\log_{10} p = A - \frac{B}{C + T} \tag{2.1}$$

where p is the vapor pressure, T is the temperature, and A, B, C are three empirical parameters. Those empirical parameters were determined by fitting the pressure and temperature values available on the website of the producer of the sources. This allows to calculate the evolution of the vapor pressures throughout the process. The sought information is, however, the condensation rate at the surface of the growing film. This depends on the distance between each source and the rotating substrate, the lip temperatures, the sticking coefficient of each of the evaporated species, the source aperture geometry as well

as on possible systematic errors in the determination of the temperature of each source. The combined effect of these parameters is unknown. Therefore, the evaporation profiles were re-calibrated by imposing that the integral CGI and GGI ratios are equal to those measured by X-ray fluorescence (XRF) on the completed CIGS film. In this way, it is possible to estimate the Cu, In and Ga deposition rates at each point during the deposition. As shown in **Figure 2.2(b)**, the deposition rates are given in arbitrary units and have the aim of displaying the relative changes in the metals' evaporation profiles throughout a deposition.

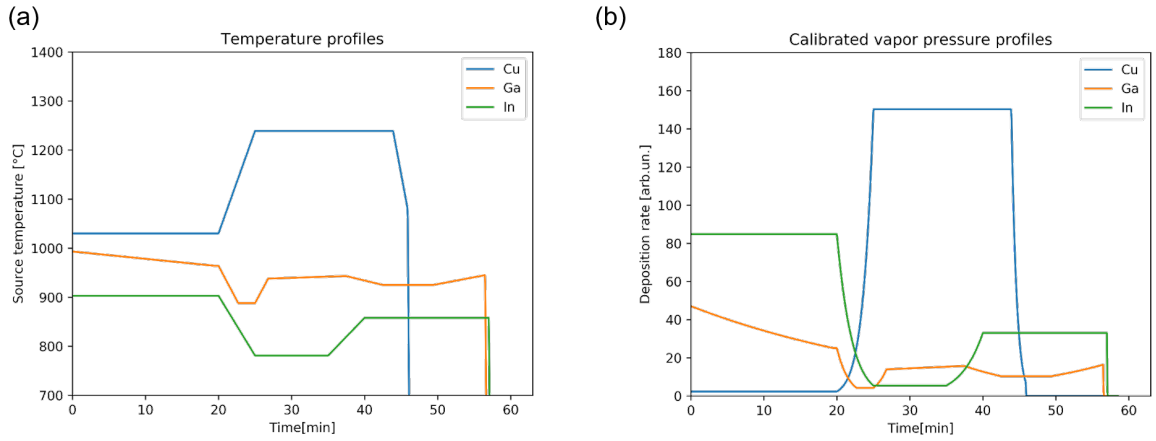

Figure 2.2: Evaporation source temperature profiles and vapor flux profiles of a standard multi-stage co-evaporation process.

2.1.3 Deposition sequence for baseline process

The evaporation source temperature profiles throughout the deposition and the resulting deposition rates are shown in **Figure 2.2**. The film is exposed to constant Se flux during different stages of the deposition.

During the first stage, In and Ga are evaporated in Se overpressure. The duration of the first stage is 20 min. The temperature of the Ga source is gradually decreased in order to obtain a GGI grading towards the Mo/CIGS interface. The substrate temperature during this stage is set to approximately 350 °C.

During the second stage, the Cu source temperature is strongly increased. And the In evaporation is strongly reduced whereas Ga is added in several sub-stages to avoid an excessively pronounced GGI grading. When the Cu source reaches its maximum temperature, the substrate temperature is increased to approximately 450 °C. As the Cu concentration in the growing film nears stoichiometry, the In source is increased again in order to obtain a slower Cu-poor to Cu-rich transition. The In rate at this stage is not sufficient to compensate for the Cu rate, and the film thus reaches a Cu-rich composition. The transition from Cu-poor to Cu-rich is identified by end-point detection, as described in Chapter 1. Afterwards, Cu is added in excess in order to reach an excess concentration of approximately 5% to 10% relative as compared to stoichiometric ratios. The Cu evaporation is then completely shut down.

During the third stage, only Ga and In are evaporated. The temperature of the Ga source is gradually increased to obtain a grading of the GGI towards the CIGS/CdS interface. Finally, the Ga evaporation is interrupted approximately 30 s before interrupting the In evaporation, to obtain a slightly indium-rich surface.

2.1.4 Post-deposition treatments

Post-deposition treatments (PDTs) have been performed at a substrate temperature of approximately 350 °C. Standard post-deposition treatments consist of the evaporation of NaF for 20 min followed by RbF for another 20 min, at a rate of 1-2 nm min^{-1}, under a constant Se flux. The temperature of the NaF source is maintained stable, and so is the expected evaporation rate during NaF PDT. The RbF source is controlled by the current and its temperature gradually decreases during PDT at a rate of approximately 0.7 °C min^{-1}. The evaporation rate decreases by approximately a factor 2 with a temperature reduction of 20 °C. The process temperatures of the NaF and RbF sources are periodically adjusted in order to obtain the best P-V parameters for the completed solar cells.

After PDT, the sample is extracted from the deposition chamber and rinsed in diluted ammonia right before chemical bath deposition (CBD).

2.1.5 Actual substrate temperature vs. nominal temperature

From Chapter 3 to Chapter 6 in this thesis, unless explicitly stated otherwise, the term "temperature" for the substrates shall primarily refer to the nominal temperature during depositions. It is imperative to maintain awareness that the actual substrate temperature is about 30 - 50 °C higher than nominal temperature.

2.2 Additional layers and processing

2.2.1 SiO_x diffusion barrier and Mo back contact

A silicon oxide barrier layer of about 180 nm was deposited by pulsed DC magnetron sputtering onto the soda-lime glass to prevent uncontrolled diffusion of alkali elements from the galss. A triple layer of molybdenum is DC sputtered onto the silicon oxide coated soda-lime glass as the back contact. The approximate thickness of the Mo back contact is 0.5 µm.

2.2.2 ITO back electrical contact layer

For bifacial devices on glass substrates, commercial ITO glass substrates with a sheet resistance of about 10 Ω/sq. are used. It consist of a 200 nm ITO layer and a 200 nm SiO_x barrier layer. For bifacial devices on flexible substrates, ITO-coated PI foils are used, which consist of a 200 nm ITO layer deposited with DC sputtering at a flow rate of 59.4 sccm Ar and 0.6 sccm O_2 (0.4 Pa during deposition).

2.2.3 Ag precursor layer

The precursor layer method was chosen to alloy Ag into the CIGS absorbers. A 15 nm Ag layer (monitored by a quartz crystal) was deposited by thermal evaporation on the ITO/glass and Mo/glass substrates before absorber deposition. The deposition rate was controlled between 0.6 Å and 0.8 Å. After deposition of Ag, the substrates were exposed

to the air shortly before loading into the CIGS deposition chamber.

2.2.4 CdS buffer layer

Buffer layers with thicknesses of about 30 nm were deposited by chemical bath deposition (CBD). CdS CBD is performed in a cadmium acetate ($Cd(CH_3CO_2)_2$, 1.56 mM) and thiourea ($SC(NH_2)_2$, 22.4 mM) acqueous solution with diluted ammonia (NH_3, 2.5 M). The ammonia and Cd acetate solution is initially pre-heated in an immersion heater at 70 °C for 2 min. Then, thiourea is added together with the CIGS samples. Typical CBD durations are 23 min for CIGS films treated with only NaF PDT and 14 min for samples treated with additional RbF PDTs. The samples are subsequently rinsed in water, dried and annealed for 2 min at 180 °C.

2.2.5 TCOs, metal grids and anti-reflective coating

Intrinsic zinc oxide (i-ZnO) and aluminum doped zinc oxide (AZO) were deposited by RF-magnetron sputtering (13.56 MHz). i-ZnO was deposited from a ZnO target using a power density of 1.85 Wcm^{-2}, in Ar atmosphere (with additional O_2 1 mol.%). The final i-ZnO thicknesses are approximately 50 nm. AZO was deposited from a Al:ZnO target (Al_2O_3 2 wt.%) using a power density of 2.46 Wcm^{-2}, in an Ar atmosphere (with additional O_2 0.05 mol.%). The final AZO thicknesses are approximately 200 nm resulting in a sheet resistance of 100 Ω/sq. to 150 Ω/sq., which is considered sufficient for the cell size and metal grid geometry.

Ni/Al grids were deposited by electron-beam evaporation with thicknesses of 50 nm and 4000 nm respectively, monitored by a quartz crystal. The grid shape is defined by a mask pressed on the sample surface. The geometry of the metal grid has been designed to minimize the distance between the grid fingers and each point in the area of cells with an approximate size of 0.57 cm^2.

MgF_2 anti-reflective coatings (ARC) were deposited to reduce reflection losses. The MgF_2 layers were deposited by electron-beam evaporation monitored by a quartz crystal

with a final thickness of 105 nm.

2.2.6 Cell definition

Cells on opaque Mo back contact were defined by mechanical scribing with approximately 0.57 cm^2 area.

Cells with ITO back contacts on flexible PI substrates were defined by laser scribing. First, a 135 mW picosecond-pulsed NIR laser (20 kHz, 3 repetitions) was used to define the cell area (0.40 cm^2) by top TCO isolation. Then, adjacent to the cell area, laser scribes with a pulse of 1.9 W was applied to create a trench to contact the bottom ITO electrode with silver paste.

2.2.7 AlO_x passivation layer

A 30 nm Al_2O_3 passivation layer was deposited on the back side of the CIGS absorbers by the atomic layer deposition (ALD) to modify the back interface recombination by the atomic layer deposition after Mo delamination in Chapter 3. The process was performed at a substrate temperature of 200°C with Ar as carrier gas at a pressure of 25 Pa in a Fiji G2 system (Veeco Instruments Inc.). The precursors were trimethylaluminium (TMA) and H_2O. The growth rate was determined by ellipsometry on Si (100) reference substrates and linear growth was observed with a rate of 0.99 Å $cycle^{-1}$.

2.3 Perovskite top cell for tandem devices

Perovskite top cells were fabricated by another member of the group (Huagui Lai).

2.3.1 Perovskite material preparation

Prepatterned ITO coated polyethylene naphthalate (PEN) (12 ohm/sq) were purchased from Advanced Election Technology Co., Ltd. Lead(II) iodide (PbI_2, 99.99%), cesium iodide (CsI2, 99%), formamidinium iodide (FAI, ≥99.99%), formamidinium bromide (FABr,

≥99%), methylammonium bromide (MABr, ≥98%), [2-(9H-Carbazol-9-yl)ethyl]phosphonic Acid (2PACz, >98%) were purchased from Tokyo Chemical Industry Co., Ltd. Dimethylformamide (DMF, anhydrous, 99.8%), dimethyl sulfoxide (DMSO, anhydrous, ≥99.9%), diethyl ether (anhydrous, ≥99.9%), chloroform (CF, anhydrous, 99.8%), isopropanol (IPA, anhydrous, ≥99.9%), lead(II) bromide ($PbBr_2$, 99.999%) were purchased from Sig-ma-Aldrich Pty Ltd. Ethanol (anhydrous, ≥99.9%) was purchased from VWR International, LLC. [6,6]-Phenyl-C61-butyric acid methyl ester (PCBM) was purchased from Xi'an Polymer Light Technology Corp. Zinc oxide nanoparticles (ZnO, 2.5 wt% in IPA) were purchased from Avantama AG. All the materials were used as received. 2-thiopheneethylammonium chloride (TEACl) was synthesized according to ref [79].

2.3.2 Perovskite top cell fabrication

The pre-patterned PEN/ITO substrates were first cleaned with ethanol and dried with N_2 flow. Then the substrates were further cleaned by UV/Ozone treatment (Jelight Company Inc.) for 20 min. 2PACz precursor (0.3 mg mL^{-1} in ethanol) was spin-coated onto the cleaned ITO sub-strates at 3000 rpm for 30 s after 1 min resting on the substrate, followed by an annealing at 100°C for 5 min to remove the solvent.

After cooling, perovskite solution was spin-coated on-to the substrate by a two-step spin-coating. The first step is 2000 rpm for 10 s with a ramp-up of 200 rpm s^{-1} and the second step is 6000 rpm for 40 s with a ramp-up of 2000 rpm s^{-1}. Diethyl ether (300 μL) was dropped onto the spinning substrate at the 20 s of the second step. The substrate was then annealed at 60°C for 2 min and 100°C for 7 min. The perovskite precursors were prepared by dissolving MABr (21.50 mg), CsI (74.83 mg), FABr (95.98 mg), FAI (198.11 mg), $PbBr_2$ (352.33 mg) and PbI_2 (663.85 mg) into a mixed solvent of DMF (1600 μL) and DMSO (400 μL). TEACl postdeposition treatment was carried out by dissolving TEACl in IPA with a concentration of 0.5 mg mL^{-1} and spin-coating onto the perovskite film at 3000 rpm for 30 s, followed by an annealing at 100°C for 3 min. After cooling, PCBM (20 mg mL^{-1} in chloroform) was spin-coated at 3000 rpm for 50 s, followed by annealing at 100°C for 10 min. Thereafter, ZnO nanoparticles was spin-coated at 5000 rpm for 50

s, followed by annealing at 100°C for 1 min. All the spin-coating procedures were carried out in N_2-filled glove box.

The substrates were then transferred to sputter chamber for the deposition of IZO electrode at a pulsed DC power of 200 W. The active areas of the devices were defined using a patterned mask.

2.4 Optical and electronic characterization

2.4.1 *J-V* characterization

2.4.1.1 Monofacial solar cells

The solar cell photovoltaic parameters were characterized by means of current-voltage (IV) measurements in 4-terminal configuration under simulated AM 1.5G conditions at 25 °C using a Keithley 2400 source-meter and a LOT solar simulator with ABA specifications. The intensity was adjusted to meet a power density of $1000\,\mathrm{W/m^2}$ using a certified Si reference cell. The calibration shows a slight mismatch to the current measured with EQE measurements. Further parameters from the JV measurement are extracted by fitting the one diode model in Eq. 1.2.

2.4.1.2 Bifacial solar cells

In bifacial configuration, the total irradiation the device is subjected to is more than 1-sun per unit area in the presence of the albedo. The albedo is defined as the ratio between the diffuse reflections from the ground with respect to the direct front irradiation:

$$albedo = \frac{\text{the reflected light } (\mathrm{W/m^2})}{\text{the incident light } (\mathrm{W/m^2})} \tag{2.2}$$

Therefore, PCE, which is defined as the ratio of the power output over the incident power per area, is no longer a proper way to report the device performance in bifacial configuration. The correct way to report the bifacial performance is by using the BiFi

factor. For instance, a power generation density of 25 mW/cm^2 $BiFi_{200}$ means that the 25 mW are generated per cm^2 of device area, when the device is simultaneously subjected to 1-sun irradiance at the front and 0.2-sun irradiance at the rear.

For bifacial device measurements in this thesis, in addition to one sun illumination from the front side, an additional illumination was provided to the rear side with a light-emitting diode (LED) lamp. The illumination intensity from LED lamp was calibrated with the J_{SC} of the device by controlling the distance between the LED lamp and the device. For example, when targeting 0.2-sun, we turned around the device and illuminated the front side of the device with the LED lamp. If the device has an J_{SC} of 37 mA/cm^2 in standard configuration, we adjusted the distance between the LED lamp and the device until we get an J_{SC} of 7.4 mA/cm^2.

2.4.1.3 Perovskite/CIGS tandem solar cells

The tandem devices in the four-terminal configuration were characterized using a perovskite filter (PEN/ITO/HTL/Perovskite/ETL/ZnO/IZO).

2.4.2 External quantum efficiency

The external quantum efficiency (EQE) response of a solar cell determines the probability that an incident photon with a specific wavelength results in the extraction of a electron-hole pair out of the device. The EQE can be defined at each wavelength as the ratio between the photon flux Φ and the photocurrent. By integrating the product of EQE and the solar photon flux density over all relevant wavelengths, the solar cell current at measurement voltage can be calculated (typically short circuit conditions):

$$J_{SC} = q \cdot \int_{-\infty}^{\infty} EQE(\lambda) \cdot \Phi_{(AM1.5G)}(\lambda) \cdot d\lambda \tag{2.3}$$

In the experiments, the EQE response was measured at zero bias with an inhouse-built system equipped with a halogen lamp and a monochromator (triple grating), chopped with a frequency of 260 Hz. The measurements were carried out under bias illumination with

an intensity of approximately 100 Wm^{-2}. The solar cell temperature was kept constant at 25 °C using PID-controlled Peltier heat pumps. The spectra calibration was performed by comparing the spectral response of the cell with that of a silicon cell with a certified spectral response from Fraunhofer ISE.

2.4.3 Temperature and illumination dependent I-V

A temperature controlled stage placed in a cryostat implementing liquid nitrogen cooling and resistive heating allows the measurement of IV curves at different temperatures. Measurements are done in 4-terminal sensing, using a Keithley 2400 source meter. The illumination for those measurements is provided by a halogen light source equipped with a neutral density filter wheel. These measurements allow to collect information about potential barriers within the solar cells, as well as a determination of the diode saturation current density J_0, the temperature dependence of the diode ideality factor A and the activation energy of the primary recombination pathway E_A [80].

2.4.4 Admittance spectroscopy

Admittance measurements in capacitance vs. frequency (Cf) and capacitance vs. voltage (CV) mode are carried out on the same temperature controlled stage as the T-IV measurements, using an Agilent E4980A LCR meter with 4-terminal sensing. Test signal oscillation level is 30 mV. Before measurement all cells are relaxed at 50 °C in the dark for 1 hour. For some capacitance steps in the Cf measurements an activation energy is extracted by the method described by Walter [81]. For CV measurements, the frequency is chosen in a region of flat capacity-frequency behavior over all temperatures investigated, unless otherwise notified at 1kHz. The voltage sweep typically covers the range from -1.5 V to 0.5 V. From this data the apparent doping is extracted using the Mott-Schottky representation [82].

2.4.5 Transmittance-reflectance spectroscopy

The transmittance-reflectance spectra measurements were performed with a UV-3600 Shimadzu UV-VIS-NIR spectrophotometer equipped with an integrating sphere. Absorbance was evaluated using the function:

$$A_{\text{abs}} = 1 - T_{\text{abs}} - R_{\text{abs}} \tag{2.4}$$

where T_{abs}, R_{abs}, and A_{abs} are spectral-dependent transmittance, reflectance, and absorbance.

2.4.6 Internal quantum efficiency

The internal quantum efficiency (IQE) response is defined here as the EQE corrected for reflections, shading and and parasitic absorption in the layers above the CIGS absorber. It gives indications on the combined transmission and collection losses.

The IQE under front and rear illumination are calculated here as:

$$IQE_{front} = \frac{EQE_{front}}{(1 - A_{TCO,CdS})(1 - C_g)(1 - R_{front})} \tag{2.5}$$

$$IQE_{rear} = \frac{EQE_{rear}}{(1 - A_{ITO})(1 - R_{rear})} \tag{2.6}$$

where $A_{\text{TCO,CdS}}$ is the combined absorptance from the buffer and window layers, A_{ITO} is absorptance from ITO back contacts in bifacial configuration, R_{front} and R_{rear} are the reflectance of the full device measured from the front the rear side, and Cg is a constant accounting for the grid coverage, estimated to be 1.5% of the total area. IQEs were calculated by measuring EQEs, reflectance spectra of completed solar cells and absorptance spectra of window and buffer layers.

2.5 Material characterization

2.5.1 Compositional profiling: SIMS and XRF measurements

The integral absorber metal ratios GGI, [Cu]/([Ga]+[In]) (CGI), and thickness were estimated by means of XRF from the intensities of the Kα Ga, In an Cu emission lines. The yields were scaled based on measurements of a calibrated sample.

Compositional depth profiles were measured by time-of-flight secondary ion mass spectrometry (SIMS, ION-TOF GmbH TOF SIMS5). Thereby a $O_2{}^+$ secondary sputter gun was used for depth profiling and a primary Bi^+ ion gun for analysis. As the GGI ratio determines the local band gap, a GGI depth profile allows to estimate local carrier generation and can be used as input for device simulation including the effects of the graded band gap on charge carrier transport. In order to obtain a GGI depth profile from a SIMS measurement, the leading and trailing edges of the absorber layer were defined to be at the sputter times where the SIMS count rate for Ga reaches half plateau values. Within that range, the Ga/In SIMS yield ratio γ was scaled until the GGI ratio of integrated Ga and In in SIMS counts reached the GGI value obtained from XRF.

$$GGI_{\text{int,SIMS}} = \frac{\sum Ga}{\sum Ga + \gamma \sum In} \tag{2.7}$$

Then with the determined γ value the local GGI is calculated according to

$$GGI_{\text{local}} = \frac{Ga}{Ga + \gamma In} \tag{2.8}$$

For scaling of the depth axis, the layer thickness was measured by SEM cross-sectional measurements on a regularly recalibrated instrument. Notably, very similar gradings are obtained if layer boundaries are derived from Cu or Se half maximum positions instead of Ga, in analogous manner.

2.5.2 Transmission electron microscopy

TEM and STEM characterizations were performed by Tzu-Ying Lin from National Tsing Hua University in Taiwan. Transmission electron microscopy (TEM) cross-sectional samples were prepared by the FEI Helios Nanolab 600i system. High-resolution high-angle annular dark field scanning transmission electron microscope (HAADF-STEM) imaging and selected-area electron diffraction have been carried out using a spherical-aberration corrected field emission TEM, JEM-ARM200FTH. Chemical composition analysis by STEM-EDS has been carried out using a F200 HRTEM and Talos F200X.

2.5.3 Scanning electron microscopy

SEM top-view and cross-sectional micrographs were obtained using a Hitachi S-4800 unit with electron acceleration voltage of 5 keV and a working distance of 4 mm. The sample cross section was prepared by cleaving the sample and substrate stack just before the measurement. For the top-view measurements, an approximately 1 nm Pt coating was deposited by DC magnetron sputtering prior to the measurements to avoid sample charging.

2.5.4 X-ray diffraction (XRD)

X-ray diffraction was used to compare structural properties related to the crystalline quality of the CIGS films at different growth stages. XRD was measured in a Bragg-Brentano configuration from 10 to 60° (2θ) and 0.0167° step intervals with a X'Pert PRO θ-2θ scan using Cu-K_{α_1} radiation.

2.5.5 X-ray residual stress analysis (RSA)

X-ray residual stress analysis (RSA) is performed to obtain the residual stress in CIGS absorbers. By measuring the d-spacing variations of crystals at different tilt angles between their crystallographic plane and sample surface (ψ), the residual stress (σ) of the sample

in the goniometer plane can be derived, given the Young's Modulus (E_{hkl}) and Poisson ratio ν_{hkl}. For instance, in-plane tensile stress would result in a larger d-spacing when tilting angle increases, as shown in Figure 2.3.

In this thesis, X-ray RSA was carried out in the side inclination mode (χ scan) with a symmetric coupled scan, where the ψ angles are equal to tilting angle χ, as shown in Figure 2.4. The residual stress is calculated by Eq. 2.9 to Eq. 2.11.

$$\epsilon_{\psi}^{hkl} = \frac{1}{2} S_2^{hkl} \sigma \sin^2 \psi + 2 S_1^{hkl} \sigma \tag{2.9}$$

$$S_1^{hkl} = -\frac{\nu_{hkl}}{E_{hkl}} \tag{2.10}$$

$$\frac{1}{2} S_2^{hkl} = \frac{1 + \nu_{hkl}}{E_{hkl}} \tag{2.11}$$

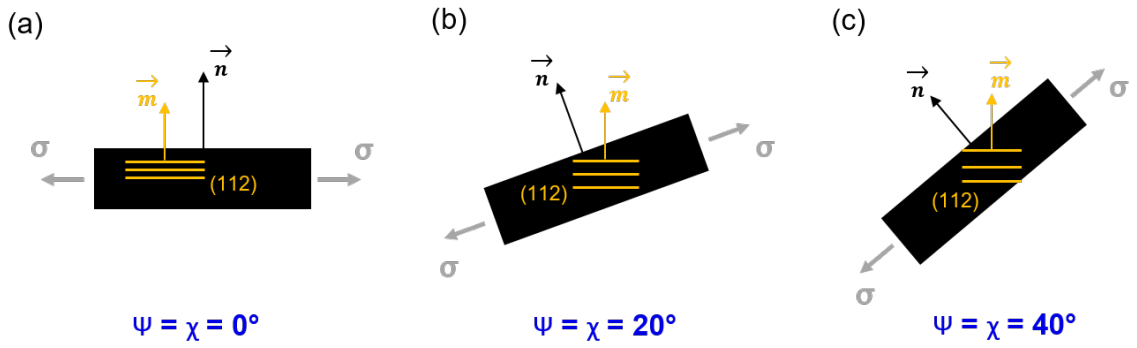

Figure 2.3: Illustration (side view) of how in-plane tensile stress (σ) changes the d-spacing (112) with different tilting angle in side inclination mode. ψ is the angle between vector **n** and vector **m**.

2.5.6 Time resolved photoluminescence (TRPL)

TRPL measurements were performed using a 639 nm diode laser with 100 ps pulse duration as excitation source, and an InGaAs photomultiplier in combination with a PicoQuant

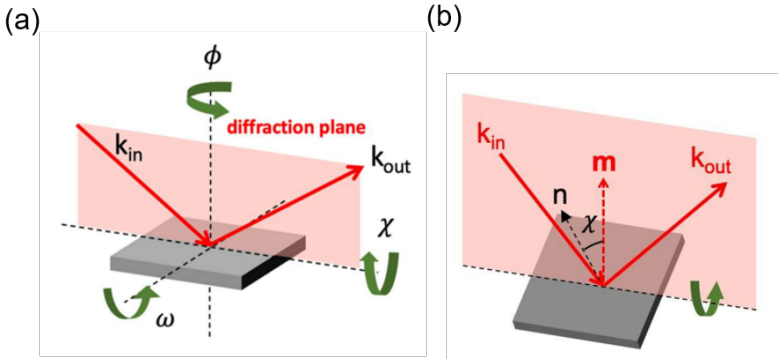

Figure 2.4: (a) Definition of the three sample rotation axes (b) Residual stress analysis with χ scan (side inclination mode). Vector **n** normal to the sample surface and vector **m** normal to the lattice plane lie in the diffraction plane Reproduced from [83]

time correlated single photon counting electronics for signal acquisition. Pulse repetition rates were chosen depends on the lifetime and in a range of 0.1 MHz to 0.4 MHz. The illumination spot size was around 130 μm diameter. The corresponding photon density was around 7×10^{11} cm^{-2} per pulse. The collection spot size is 2.5 μm diameter, considerably smaller than the the escitation spot size to compensate for the diffusion of photogenerated carriers in and out of the collection spot. Before TRPL measurements, the window layers were etched away in acetic acid, leaving a thin CdS layer on the absorbers.

2.5.7 Raman spectroscopy

Raman Spectroscopy is a non-destructive chemical analysis technique which provides information about chemical structure, phase and polymorphy, crystallinity and molecular interactions. It is based on the Raman effect, which is the inelastic scattering of light by molecules when they are excited by a laser beam. By analyzing the frequency of the scattered light, it is possible to determine the vibrational, rotational, and other structural characteristics of the molecules to further identify the chemical bonds and the chemical composition of the sample.

3 Influence of Ga back gradings on device performance

This chapter is adapted from the publication:

Yang, S. C., Ochoa, M., Hertwig, R., Aribia, A., Tiwari, A. N., and Carron, R. (2021). *Influence of Ga back grading on voltage loss in low-temperature co-evaporated Cu(In,Ga)Se_2 thin film solar cells*, Progress in Photovoltaics: Research and Applications, 29(6), 630-637. [84]

My own contribution to this publication consisted in: design of the experiments, deposition of CIGS thin films, completion of working solar cells, measurement and analysis of: SIMS, XRF, J-V, EQE, TRPL, and data interpretation. ALD deposition was done by Ramis Hertwig and Abdessalem Aribia. Numerical simulation was performed by Mario Ochoa.

3.1 Introduction

While the Ga back grading plays a vital role in minimizing the recombination at the CIGS/Mo interface in monofacial structure, Ga grading is even more important when it comes to the performance under rear illumination in bifacial structure. Normally, very low

J_{SC} under rear illumination were obtained in bifacial CIGS devices due to short diffusion length of carriers and high rear interface recombination.

Despite diverse research results about the back gradings [6, 85, 86, 87], there is no conclusive agreement about minimum required back grading heights. Moreover, the quality of state-of-the-art absorbers considerably improved following breakthroughs and developments of the past ten years, leading to longer diffusion length [88]. It makes the control of back interface recombination become even more critical. A quantitative assessment of the impact of ΔGGI on the electrical losses is therefore required. However, experimental investigations are not straightforward, because tuning the ΔGGI value generally also affects the elemental distributions in the notch and front regions, introducing other dependencies in the electrical loss difficult to disentangle.

In this chapter, we take advantage of a low-temperature CIGS deposition process (≈450 °C) to modify the back grading. Less pronounced In-Ga inter-diffusion at low temperature allows an improved control and steeper slopes of the GGI grading [89]. It also allows for almost unchanged grading in the notch and front region. We compare the experimental V_{OC} deficit (E_g/q - V_{OC}) and changes in V_{OC} calculated from TRPL transients in absorbers with different back grading heights. We modify the back surfaces of CIGS absorbers to assess the influence of back surface recombination as a limiting factor for higher V_{OC}. Furthermore, numerical simulations of voltage loss for absorbers with different ΔGGI and diffusion lengths are also performed, and further compared with experimental data. Our work provides direct guidelines to design graded absorbers with reducing voltage loss for high efficiency CIGS solar cells.

3.2 Ga back grading modification

Ga back gradings were tuned by changing the evaporation rates of In and Ga during the first coevaporation stage, as shown in Figure 3.1. Solid lines show the evaporation rates of our reference process, estimated from the sources temperature setpoints. Three different approaches are investigated to modify the back gradings. The corresponding samples are identified with R, G, I and O letters, representing reference, Ga series, In series and early

stage In-free series (O series). More detailed process sequences and heating/cooling rates in the first stage for each sample can be found in Table 3.1.

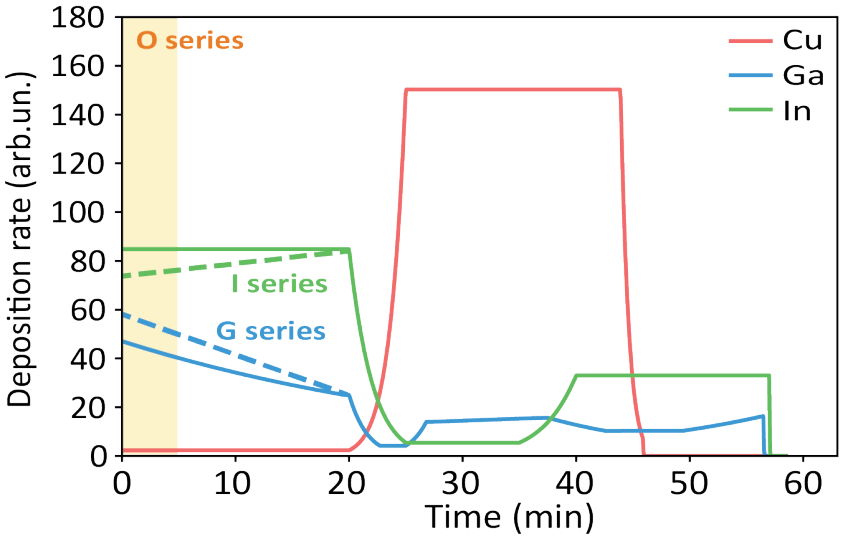

Figure 3.1: Schematic representation of a multi-stage deposition with indicative Cu, In, Ga evaporation rates. The solid lines represent the baseline process (R). The dashed lines and orange block show three different approaches to modify the back grading (I, G, O).

Table 3.1: Evaporation ramping rates for Gallium and Indium in the first stage of CIGS absorber deposition.

Sample	ΔGGI	Ga cooling rate at first stage (°C/min)	In heating rate at first stage (°C/min)	In shutter close period (min)
R1	0.20	1.5	0.0	0
R2	0.20	1.5	0.0	0
G1	0.21	2.0	0.0	0
G2	0.23	3.0	0.0	0
I1	0.26	1.5	2.5	0
I2	0.25	1.5	3.0	0
I3	0.32	1.5	6.0	0
I4	0.29	1.5	6.0	0
O1	0.41	1.5	6.0	3
O2	0.43	10	6.0	4
O3	0.50	10	6.0	5

Figure 3.2 - Figure 3.4 show the GGI depth profiles of sample sereis G,I and O, determined by scaling the elemental traces in SIMS measurements with integral GGI values obtained from XRF. For comparison, the depth profile of reference R1 is shown in all the figures as a reference. The height of the back grading is defined by the quantity ΔGGI,

which is the difference between the minimum GGI value in the notch and its maximum near the back interface. The equivalent E_g energy is calculated by Eq. 6.1 [90].

$$E_g = 1.004(1 - \mathrm{GGI}) + 1.663\mathrm{GGI} - 0.033\mathrm{GGI}(1 - \mathrm{GGI}) \tag{3.1}$$

In the first (G) and second (I) approach we implemented steeper gallium source cooling rates (dashed blue line G in Figure 3.1), and steeper indium source heating rates (dashed green line I in Figure 3.1) in the first stage. However, the attempts only resulted in moderate changes in the corresponding composition profiles shown in Figure 3.2 and Figure 3.3.

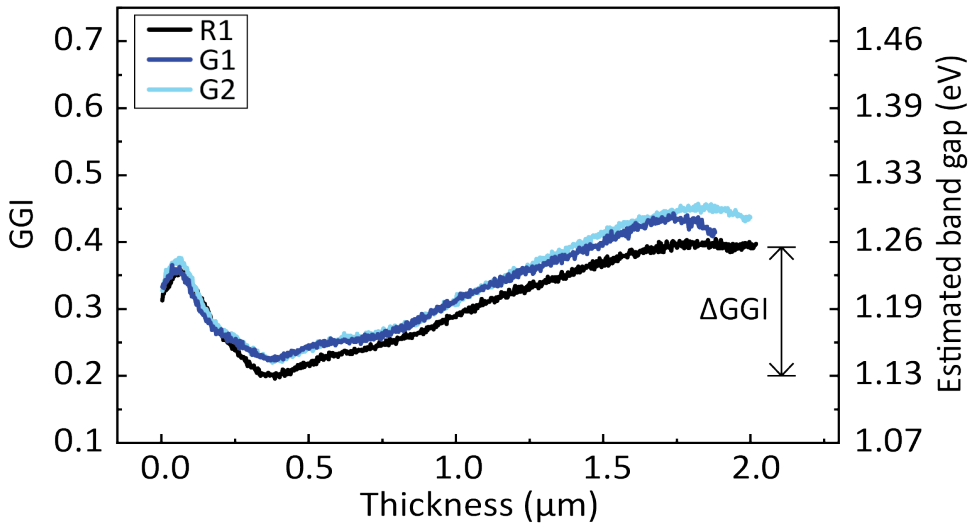

Figure 3.2: GGI and E_g depth profiles for different Ga source cooling rates.

A third approach (O) was developed to further increase ΔGGI: the indium shutter is kept closed during the initial minutes of the deposition process, as illustrated by an orange block (O) in Figure 3.1. Therefore, the absorber is In-free during the initial minutes of the deposition process. The corresponding depth profiles are shown in Figure 3.4. With this

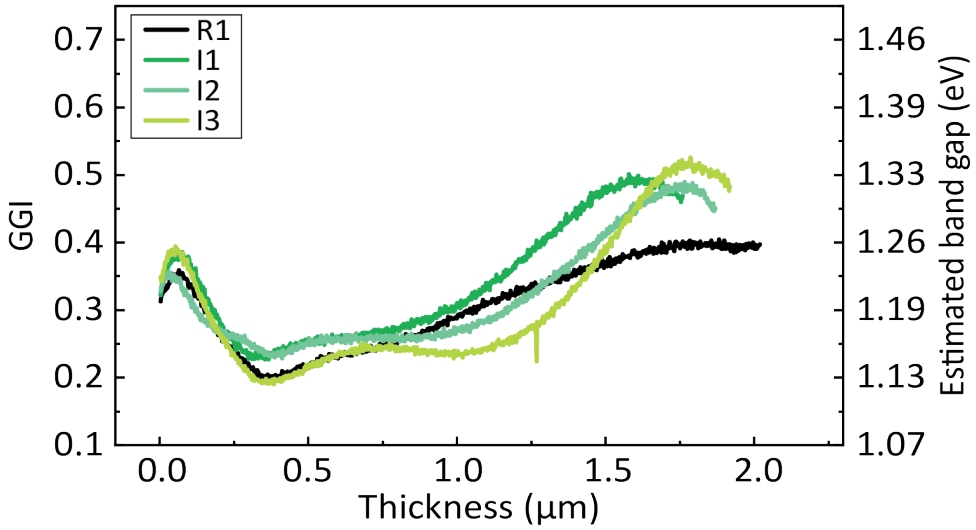

Figure 3.3: GGI and E_g depth profiles for different In source heating rates.

approach, the highest ΔGGI value of 0.5 was obtained, equivalent to about 0.33 eV. In the different deposition runs, Ga and In source temperatures were adjusted by small constant offsets over the whole process, in order to compensate for drifts in the source evaporation yields and achieve similar integrated GGI and optical bandgaps.

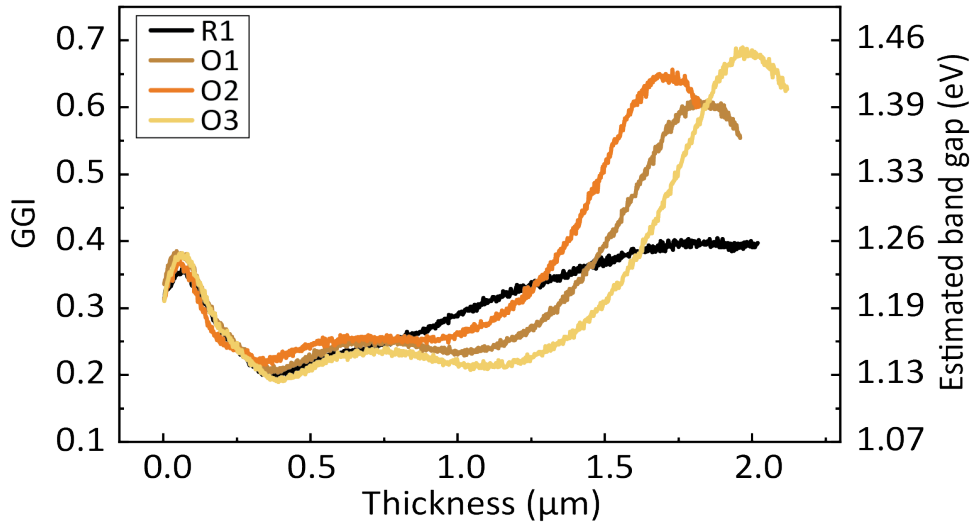

Figure 3.4: GGI and E_g depth profiles for different In-free periods in early stage In-free series.

Table 3.2 compares the J-V parameters of solar cells with different ΔGGI investigated in this study. GGI values for those samples range from 0.28 to 0.35 and CGI values

are almost within the confidence interval of the composition measurements. Short-circuit current density (J_{SC}) is in good agreement with calculated EQE currents and the fill factor (FF) is similar for all samples. The most sensitive parameter is the V_{OC}, which is analyzed and discussed in the following.

Table 3.2: Composition of CIGS absorbers with different ΔGGI and the corresponding J-V parameters.

Sample	GGI	CGI	E_g(eV)	ΔGGI	Photovoltaic parameters				V_{OC} deficit (V)
					V_{OC} (V)	J_{SC} (mA cm^{-2})	*FF* (%)	PCE (%)	
R1	0.31	0.86	1.144	0.20	0.686	35.3	77.6	18.8	0.458
R2	0.32	0.87	1.142	0.20	0.679	36.3	77.5	19.1	0.463
G1	0.33	0.88	1.138	0.21	0.687	35.2	77.1	18.7	0.451
G2	0.34	0.90	1.140	0.23	0.695	35.6	76.9	19.0	0.445
I1	0.34	0.88	1.147	0.26	0.703	35.0	76.8	19.0	0.444
I2	0.32	0.91	1.137	0.25	0.693	35.6	77.1	19.0	0.444
I3	0.31	0.88	1.123	0.32	0.697	35.8	76.4	19.1	0.429
I4	0.28	0.88	1.121	0.29	0.685	36.7	77.4	19.5	0.436
O1	0.34	0.89	1.132	0.41	0.707	36.0	77.0	19.6	0.425
O2	0.35	0.90	1.150	0.43	0.723	35.2	77.5	19.7	0.427
O3	0.34	0.87	1.135	0.50	0.716	35.4	76.2	19.3	0.419

3.3 Effect of ΔGGI on microstructure

In addition to the composition profiles, the microstructure in the front and notch was investigated by cross-section SEM to identify possible deterioration of the microstructure. As shown in Figure 3.5, the grain size is similar for all the absorbers in the front and notch regions. A decrease in grain size is only observed towards the back, especially for absorbers with high ΔGGI. This observation is consistent with existing reports describing a decrease in grain size with increased Ga content [91].

Apart from changes in the microstructure, the presence of structural and electronic defects is also investigated through the Urbach tails [92]. The Urbach energy (E_U) is estimated from the quasi-exponential decay in the long wavelength edge in the EQE curves [85]. As shown in Figure 3.6, there is no clear trend of E_U with ΔGGI. The precision on the values is not better than ±1 meV due to the presence of interference fringes in the EQE spectra. The values derived from EQE measurements are typically slightly larger than those derived from PL, due to the higher energy range for which the fit is performed.

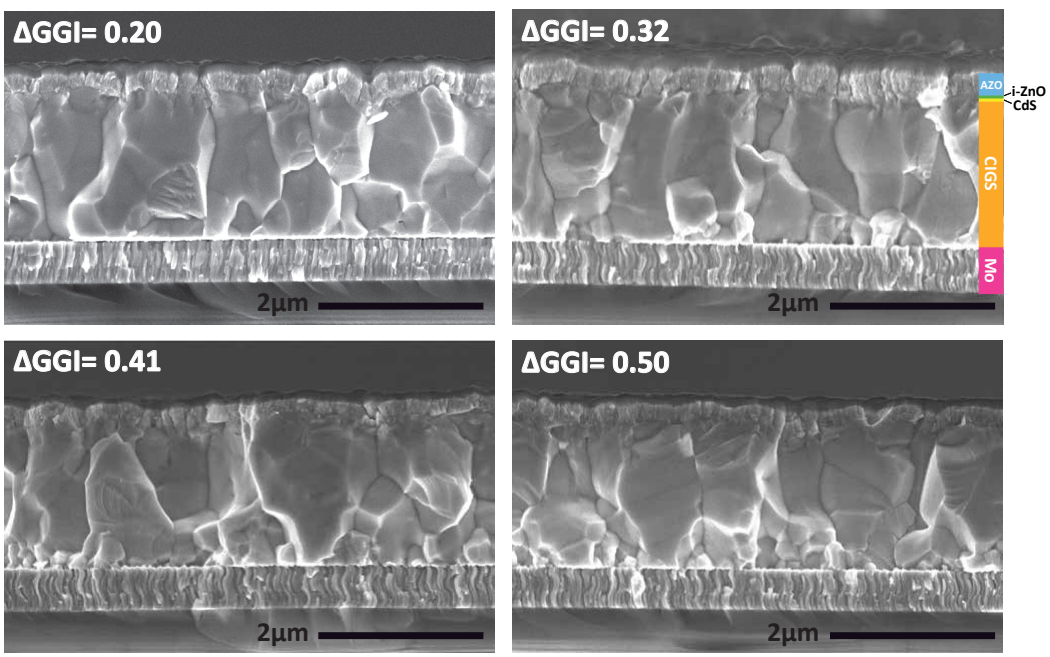

Figure 3.5: SEM cross-section images for solar cells (R1, I3, O1 and O3) with different ΔGGI. Increased GGI towards the back of the absorber leads to reduced grain size at back region, while the microstructure in the front and notch regions appear unchanged.

GGI depth profiles, SEM cross-sectional images and extracted E_U show no noticeable impact on the front and notch regions from increased ΔGGI at least up to 0.5. Therefore, different electrical loss between samples is mostly caused by different back recombination, instead of changed properties either in the front or notch regions of the absorbers.

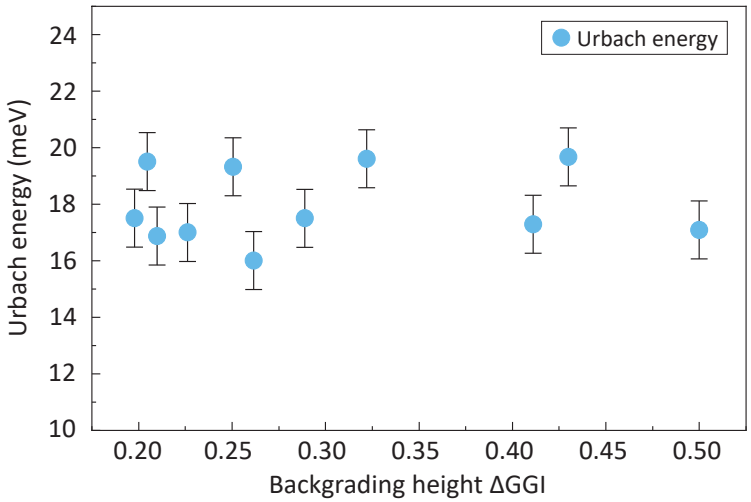

Figure 3.6: Urbach energy (E_U) versus different ΔGGI. No clear correlation is evidenced between E_U and ΔGGI.

3.4 Effect of ΔGGI on V_{OC} deficit

To see the effect of ΔGGI on the electrical loss, $V_{OC,def}$ is also given in Table 3.2, which is calculated as the difference between the E_g energy and the V_{OC}. The E_g value was determined by linear extrapolation of the plot ((photon energy × EQE)^2 vs photon energy) for values between 25% and 75% of the EQE maximum.

Figure 3.7 shows the change of $V_{OC,def}$ values with different ΔGGI. An evident improvement in $V_{OC,def}$ with higher ΔGGI is observed. The $V_{OC,def}$ values improved by about 35 mV when ΔGGI is increased from 0.20 to 0.32. For ΔGGI increase from 0.32 to 0.50, an additional V_{OC} gain of 10 mV is observed. However, this 10 mV gain may also be explained by sample to sample variation, measurement uncertainty or E_g extraction. To obtain more solid evidence on the increased $V_{OC,def}$ in the full range of ΔGGI, TRPL measurements were conducted and are discussed in Section 3.5.

To illustrate this gain, J-V curves of two solar cells (G1 and O3) with similar E_g but different ΔGGI (0.21 and 0.50) are compared in Figure 3.8. The corresponding E_g extractions are shown in the inset. Sample O3 exhibits a strongly increased V_{OC} due to higher ΔGGI. The J_{SC} is comparable for both solar cells, consistent with their similar bandgaps. Due to the improvement in V_{OC}, photovoltaic conversion efficiency (PCE) is increased from 18.7% to 19.3%. PCE of the champion cell in this study is about 19.7%.

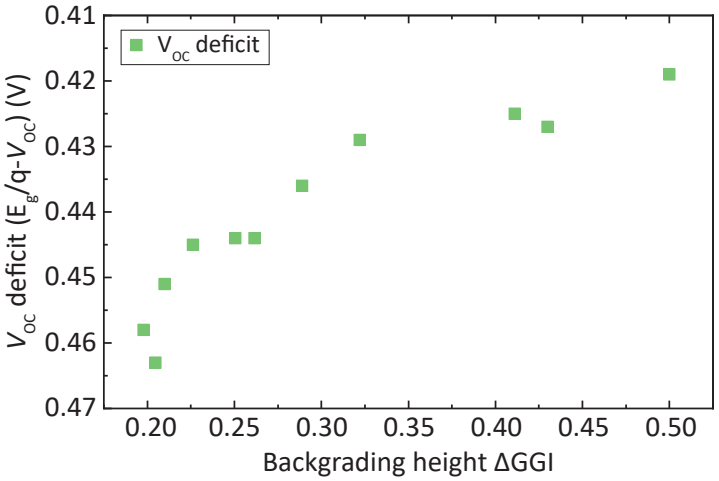

Figure 3.7: $V_{OC,def}$ of the investigated samples as a function of their ΔGGI values.

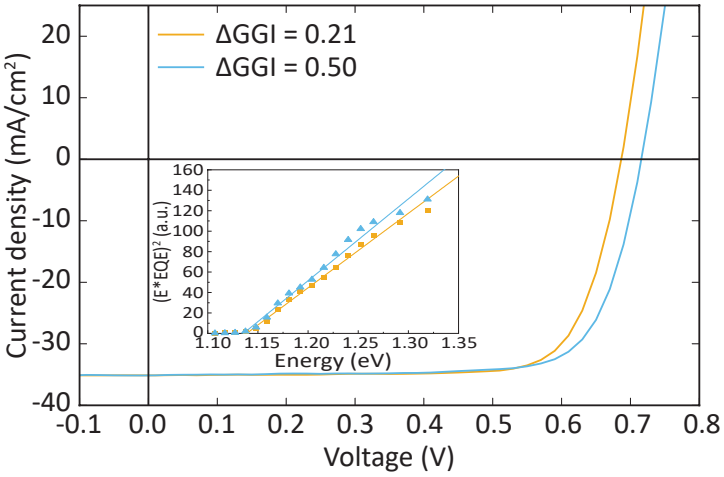

Figure 3.8: J-V curves and E_g extraction for two selected solar cells with similar E_g but different ΔGGI values.

3.5 Effect of ΔGGI on TRPL lifetime

$V_{OC,def}$ is a device parameter related to overall electrical loss at the device level, whereas TRPL decays provide direct information of carrier dynamics in the absorbers that can be linked to its material quality. Therefore, the relationship between TRPL lifetime and ΔGGI is investigated to see if high ΔGGI values up to at least 0.50 still contributes to reduction in electrical losses, as discussed in Section 3.4.

TRPL measurements were performed on selected absorbers covering different ΔGGI values as shown in Figure 3.9(a). The decays were fitted in the time window from 20 ns to 500 ns by a two-exponential formula (Eq. 3.2) with two time constants (τ_1 and τ_2) and two prefactors (A_1 and A_2). The effective lifetime τ_{eff} is calculated using Eq. 3.3. As visible in Figure 3.9(a) absorbers with high ΔGGI show considerably longer lifetimes as compared with low ΔGGI ones, suggesting a reduction in back interface recombination.

$$Y = A_1 \exp\left(-\frac{t}{\tau_1}\right) + A_2 \exp\left(-\frac{t}{\tau_2}\right) \tag{3.2}$$

$$\tau_{eff} = \frac{A_1\tau_1 + A_2\tau_2}{A_1 + A_2} \tag{3.3}$$

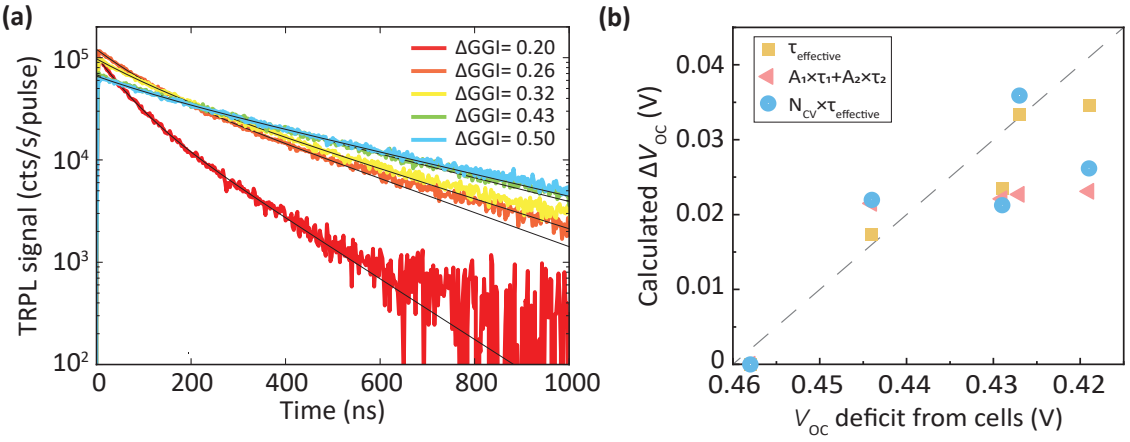

Figure 3.9: (a) TRPL transients of absorbers with different ΔGGI. The black lines are best 2-exponential fits to the data in the time window from 20 ns to 500 ns. (b) ΔV_{OC} calculated from different figures of merit using Eq. 3.5 as function of the experimental cell $V_{\mathrm{OC,def}}$.

We further calculated the theoretical change in V_{OC} based on TRPL decays. Eq. 3.4 describes the relationship between achievable V_{OC} and external light emitting-diode quantum efficiency ($\mathrm{EQE_{LED}}$) [93]. From this, the difference in achievable V_{OC} (ΔV_{OC}) of different samples is evaluated according to Eq. 3.5. Here we estimated the ratio of $\mathrm{EQE_{LED}}$ with the ratio of different figure of merits (FOMs) from the TRPL data. The absorber with a ΔGGI of 0.20 was chosen as the reference providing a ΔV_{OC} of 0 mV.

$$V_{\mathrm{OC,def}}^{\text{non-rad}} = V_{\mathrm{OC}}^{\mathrm{rad}} - V_{\mathrm{OC}} = -\frac{kT}{q}\ln(\mathrm{EQE_{LED}}) \tag{3.4}$$

$$\Delta V_{\mathrm{OC}} = V_{\mathrm{OC,def}}^{\text{non-rad}}{}_{\text{ref}} - V_{\mathrm{OC,def}}^{\text{non-rad}}{}_{\text{sample}} = -\frac{kT}{q}\ln\left(\frac{\mathrm{EQE_{LED,sample}}}{\mathrm{EQE_{LED,ref}}}\right) = -\frac{kT}{q}\ln\left(\frac{\mathrm{FOM_{sample}}}{\mathrm{FOM_{ref}}}\right) \tag{3.5}$$

Three different FOMs are established to compare the $\mathrm{EQE_{LED}}$ of different samples relatively: (1) τ_{eff}, (2) $A_1 \times \tau_1 + A_2 \times \tau_2$ and (3) $\mathrm{N_{CV}} \times \tau_{\mathrm{eff}}$. For τ_{eff}, it was assumed that the doping density is the same for all absorbers. For the second FOM, the prefactors (A_1 and A_2) were taken into account. The sum of prefactor terms are assumed to be proportional to the doping density of the absorbers. For the third FOM, the doping density $\mathrm{N_{CV}}$

extracted directly from C-V measurements at V=0 (Figure 3.10) is used instead of prefactors from TRPL decays. Figure 3.9(b) shows the relationship between calculated ΔV_{OC} from those three FOMs and $V_{OC,def}$ measured from cells. Among them, τ_{eff} gives a better correlation with $V_{OC,def}$ from cells. This can be tentatively explained by the non-uniform doping density distribution within a sample. While the bandgaps were always extracted from EQE measurement of the best cell in the sample, TRPL and C-V measurements were performed on the cells close to the best cell. To avoid the variations from the doping density, different calculated ΔV_{OC} will be further discussed in Section 3.7.

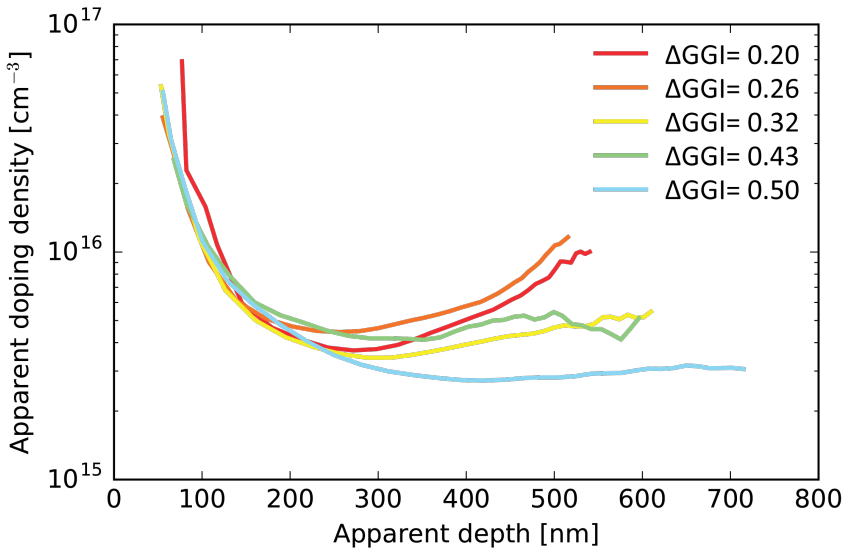

Figure 3.10: Apparent doping density profile calculated from capacitance-voltage measurements at 300K.

3.6 Back surface modification

In addition to back interface recombination, variations in TRPL decays may also arise from different non-radiative recombination rates elsewhere, e.g. within the bulk of the absorber. To extract the effect solely from the increasing ΔGGI, we further measured TRPL decays on the same series of samples after different modifications of the back interface. It also helps to understand how far high graded CIGS absorbers are from the ideal case (i.e. no back interface recombination).

After the initial measurement described in Section 3.5, the CIGS absorbers were mechanically delaminated from the molybdenum back contact with a transparent epoxy glue, as depicted in Figure 3.11. The exposed CIGS/air interface results in a lower back surface recombination velocity [94] than the CIGS/Mo contact. After TRPL characterization, the back surface was further passivated by 30 nm Al_2O_3 deposited by ALD. The concept of Al_2O_3 passivation was shown to effectively reduce recombination at CIGS/Mo [95] or CIGS/air interfaces [96]. According to the literature [94, 95, 96, 97], those three different back surfaces cover different values of surface recombination velocity, ranging from about 10^7 to 10^2 cm/s.

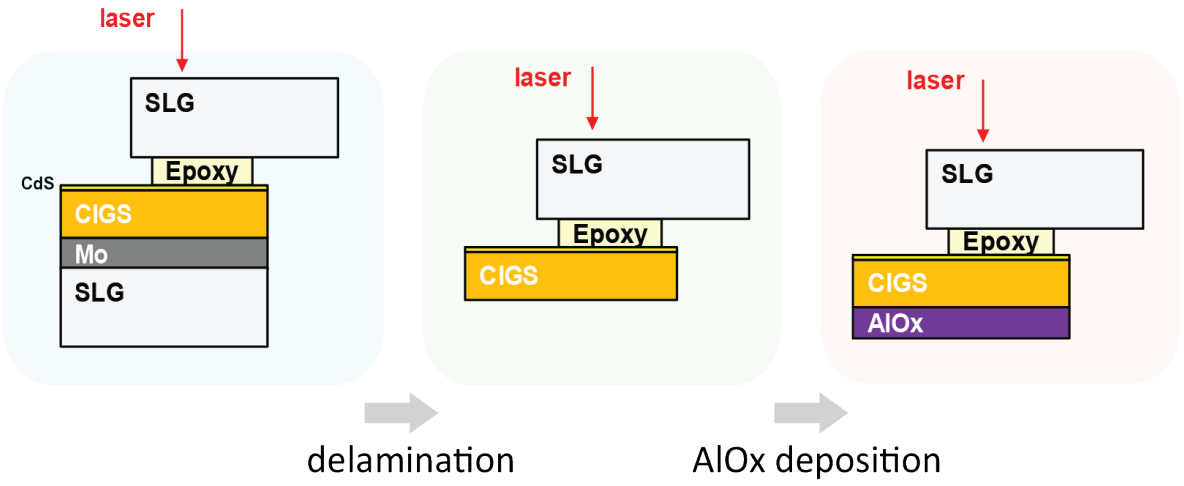

Figure 3.11: Schematics of back surface modification and the corresponding TRPL measurements.

Figure 3.12 displays the TRPL results obtained with different sample configurations. We observe an increase in lifetime after delamination, and a further increase after Al_2O_3 deposition. Improvements are especially significant for absorbers with low ΔGGI values, being three-fold for ΔGGI= 0.20 and only 1.25 times for ΔGGI = 0.50 after delamination. This is explained by the reduced electron density at the back with higher ΔGGI, resulting in a lesser sensitivity to the surface recombination velocity value. The three-fold increase for ΔGGI = 0.20 can be attributed to the difference of interface recombination velocity at CIGS/air (on the order of 10^3 cm/s) and CIGS/Mo (>10^6 cm/s). As example, Figure 3.13

shows TRPL decays for samples with low and high ΔGGI. The decays are very similar for high ΔGGI, while being very different for small ΔGGI. It suggests that back surface recombination is a strong limiting factor for V_{OC}, and that its effect can be observed with ΔGGI values up to 0.50. In addition, the τ_{eff} value is still slightly improved with increasing ΔGGI after 30 nm Al_2O_3 deposition. This can be explained by a low but non-negligible recombination at CIGS/air interface [94], further passivated by Al_2O_3.

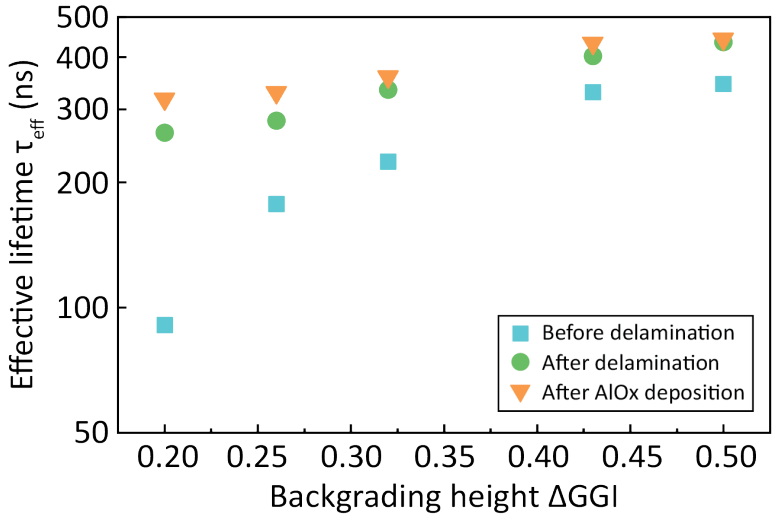

Figure 3.12: TRPL τ_{eff} for absorbers in three different sample configurations.

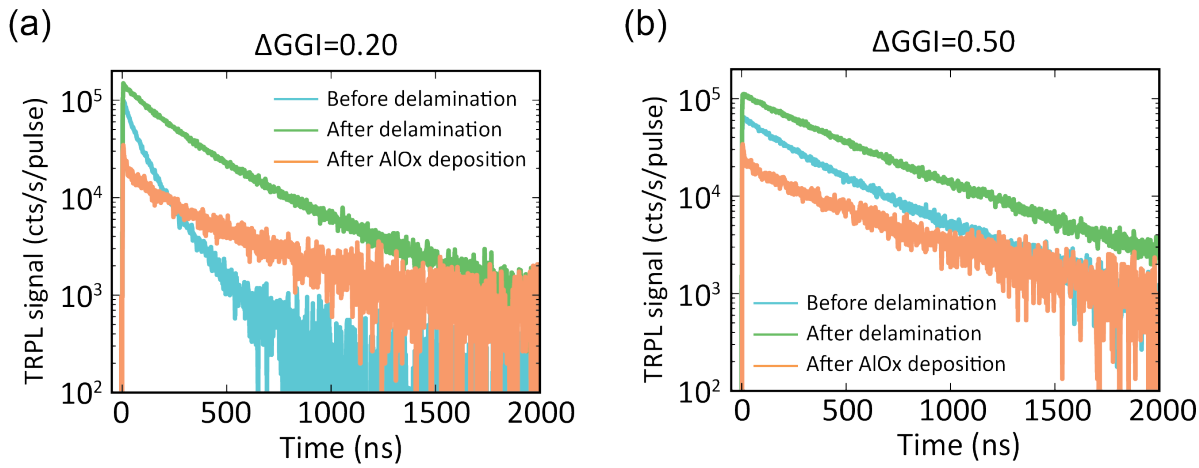

Figure 3.13: TRPL decays for the absorbers with ΔGGI = 0.20 and ΔGGI = 0.50.

3.7 Numerical simulation

To support the experimental findings of Section 3.6, we carried out finite element modelling simulations. The simulations were carried out within the framework of Sentaurus drift-diffusion simulator from Synopsis [98]. A double graded absorber with a thickness of 2 µm has been considered and divided into three different regions, namely the front grading, notch and back grading. The front grading and notch are kept constant whereas the back grading was modified to obtain several GGI profiles with ΔGGI ranging from 0 to approximately 0.8, as shown in Figure 3.14. More details and material parameters used can be found elsewhere [88].

Here we are interested in the effect of back recombination solely from varying ΔGGI and its implications on V_{OC}. Different bandgap profiles are implemented into 2 µm-thick absorbers, in which only the back grading has been modified to achieve ΔGGI values ranging from 0 to a maximum of 0.8. For simplicity, back recombination velocity is fixed to $S_b \gg 10^7$ cm s^{-1}. Other recombination velocities found at CIGS/Mo interface (e.g. 10^6 cms^{-1} in [94]) were tested and also delivered similar results in our simulation. Since back recombination is highly sensitive to the diffusion length of carriers, i.e. $L_d = \sqrt{\frac{kT}{q}\mu\tau}$, we consider a wide range of carrier mobility μ (12.5 $cm^2V^{-1}s^{-1}$ to 200 $cm^2V^{-1}s^{-1}$) and τ (approximately 100 ns to 800 ns) covering the range of values typically found experimentally. The ΔV_{OC} of a simulated device is calculated as the V_{OC} difference from that with highest ΔGGI of 0.80.

To compare with the experimnetal results, it is difficult to exclude effects on experimental V_{OC} arising from deviations in absorber doping concentration or bandgap that could occur between different growth runs. Thus, instead of Eq. 3.5, we compute the relative ΔV_{OC} before and after delamination (Eq. 3.6), for absorbers with different ΔGGI. By doing this, possible deviations in the aforementioned material properties (doping or E_g) are discriminated for the same absorber and the effect of ΔGGI can be analyzed.

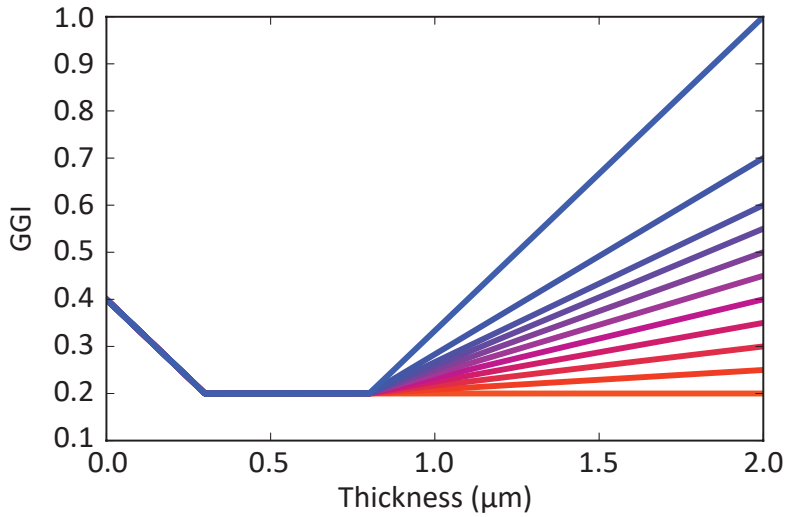

Figure 3.14: GGI profiles for simulations, with fixed front grading and notch while changing back gradings.

$$V_{\mathrm{OC}}\ \mathrm{loss} = -\frac{kT}{q}\ln\left(\frac{\tau_{\mathrm{eff,\ after\ del}}}{\tau_{\mathrm{eff,\ before\ del}}}\right) \tag{3.6}$$

Figure 3.15 shows simulation results for several L_d values as a function of ΔGGI, together with the experimental ΔV_{OC} calculated by Eq. 3.6 (orange circles) of the samples listed in Table 3.2. The V_{OC} loss is strongly dependent on the L_d value but almost insensitive to the actual combination of μ and τ used to obtain the L_d value. Two dashed lines in Figure 3.15 establish the upper and lower bound for L_d values that could reproduce the experimental results (L_d between 3.6 µm and 14.4 µm), which are in good agreement with other reports [86, 88, 94]. The solid lines are shown as extreme instances to exemplify the degree of V_{OC} loss sensitivity with respect to L_d. From Sec 3.6 and Figure 3.12, we expect a τ around 400 ns in our absorbers. By assuming a τ of 400 ns, mobilities in the range of 12.5 $\mathrm{cm^2V^{-1}s^{-1}}$ to 200 $\mathrm{cm^2V^{-1}s^{-1}}$ are suggested, with the best fit corresponding to μ=50 $\mathrm{cm^2V^{-1}s^{-1}}$ and L_d approximately 7 µm, which are in good agreement with [94]. Within this range of L_d values, simulations confirm that ΔGGI of 0.3 leads to a significant voltage loss about 7 mV to 20 mV. The voltage loss becomes insignificant ($<$ 5 mV) for ΔGGI around 0.5, independently of the L_d value. Hence, a ΔGGI $\geq$ 0.5 is needed to ensure a voltage loss below 5 mV, especially with high quality absorbers with long diffusion length.

Finally, we use the simulations to quantify the beneficial impact of the backgrading. We quantify a substantial voltage gain around 91±28 mV between ΔGGI of 0 and ΔGGI of 0.3, with deviations defined by the two dashed lines of Figure 3.15. This value is consistent with what is reported in [43] (114 mV) for low bandgap $CuInSe_2$ absorbers.

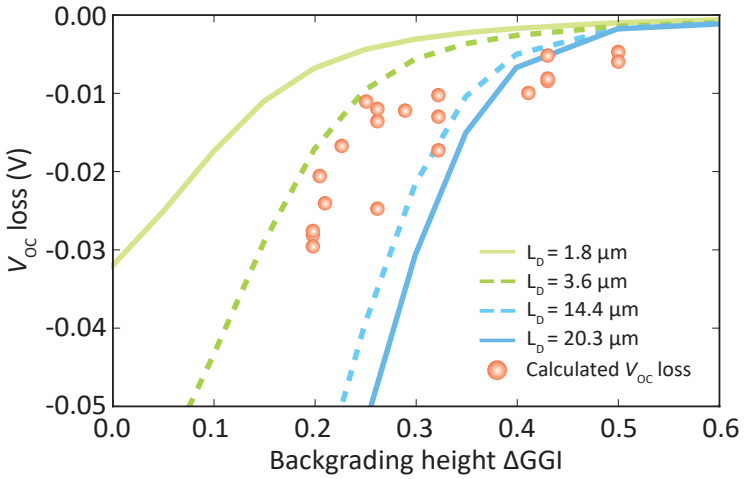

Figure 3.15: Experimental and simulation results for the estimation of V_{OC} loss. Orange circles are the V_{OC} loss calculated from experimental TRPL decays (Eq. 3.6) before and after delamination. For simulated absorbers, two solid curves depict the upper and lower limit of L_d (1.8 µm to 20.3 µm). Two dashed curves correspond to the range of L_d (3.6 µm to 14.4 µm) fitting best our experimental results (orange data points).

3.8 Conclusion

We have successfully modified the height of the compositional back gradings in CIGS absorbers. The combination of low substrate temperature and early stage In-free coevaporation allows to widely tune the ΔGGI value without significant changes in microstructure and structural disorder in the low bandgap notch and front regions of the absorber, as indicated by SEM cross-sectional images and Urbach energy values. This allows a more rigorous comparison between cells with different ΔGGI in this study.

The $V_{OC,def}$ improves up to a ΔGGI value of about 0.50, and TRPL τ_{eff} shows a similar trend with increased ΔGGI. We observe a strong correlation between $V_{OC,def}$ calculated from cells and voltage losses ΔV_{OC} estimated from TRPL τ_{eff}. In addition, absorbers

with high ΔGGI show less sensitivity of the TRPL decays to modifications of the back surface properties, i.e. different recombination velocity. We conclude that back surface recombination affects device performance in a measurable manner up to a ΔGGI of 0.50. Furthermore, we also quantify the impact of diffusion length on the voltage loss from the back interface with numerical simulations. Reasonable parameter sets yield V_{OC} loss trends in good agreement with our experimental results. The impact of back recombination is more severe in high quality absorbers with long diffusion lengths resulting from improved mobility or lifetime values. We believe our results will provide useful guidelines for designing GGI profiles for high-performance CIGS solar cells fabricated at low temperature. The proposed In-free process step makes it easier to optimize ΔGGI for existing baseline processes while maintaining almost unchanged composition and properties in the front and notch.

3.9 Sample references

Internal sample names for the samples in **Table 3.2**:

R1	R2	G1	G2	I1	I2	I3	I4	O1	O2	O3
TL3106	TL3111	TL3107	TL3108	TL3109	TL3110	TL3113	TL3112	TL3114	TL3115	TL3116

Table 3.3: Sample naming for CIGS solar cells in Chapter 3

4 Silver-alloyed CIGS with precursor layer method

4.1 Introduction

As discussed in Section 1.2.7, alloying silver into CIGS absorbers can improve their material quality and shows the potential to achieve higher PCE in the solar cells. Therefore, in this chapter we aim to explore the effect of different amount of Ag alloyed on the material properties and the device performance of ACIGS solar cells. Among different techniques for alloying Ag into the CIGS absorbers, e.g. co-evaporation, precursor layer method [55, 99], post-deposition treatment [100, 101], we chose the Ag precursor layer method for its simplicity and potential for easy implementation into existing CIGS co-evaporation equipment in research labs or in the industry.

The microstructure, elemental distribution, and crystal structure of the absorbers were investigated by SEM, SIMS, and XRD. The back interface properties were analyzed with Raman spectroscopy. The completed cells were further characterized by J-V, EQE, and C-V. Other techniques like residual stress analysis were also performed to give insight of the in-plane stress in the absorbers, which is crutial when it comes to flexible applications. The developed process and the knowledge gained here will be the starting point of the following chapters.

4.2 Precursor layer method

4.2.1 The amount of silver

To alloy different amount of Ag into the aborbers, we deposited Ag precursor layers with different thickness by thermal evaporation, ranging from 1 nm to 30 nm, on standard Mo/SiO_x/SLG substrates. This amount of Ag in our 2 µm-thick absorbers is equivalent to about 0% to 10% ([Ag]/[Ag]+[Cu]) ratio. After that, the Ag-coated substrates underwent standard three-stage co-evaporation of CIGS, which is detailed in Chapter 2. The substrate temperatures during the deposition process are provided in Section 2.1.3.

4.2.2 End-point detection

Since three stage co-evaporation process was used for absorber deposition with precursor layer method, the end-point-detection (as described in Chapter 1) is used to control the stoichiometry of the absorbers. However, the first challenge that we encountered with the presence of Ag is that both temperature drop and the PID controller value change during Cu-poor to Cu-rich transition become less detectable, especially for high amount of Ag, as shown in **Fig. 4.1**. Normally when the PID controller value changed by 0.03 or when the temperature droped by 0.4°C, we started to ramp down the Cu source temperature followed by closing the shutter of Cu source. However, the delay time increases with high Ag content (shadows in **Fig. 4.1**), which results in higher [I]/[III] ratio. Too high [I]/[III] ratio can lead to degraded device performance. With more than 30 nm of Ag precursor layer, it becomes very difficult to detect the end-point during the process. This observation is in line with what has been reported [102], resulting from slower emissivity change in ACIGS during the transition from stoichiometry to group-I rich composition. Due to this limitation, we mainly focus on the absorbers with up to 15 nm Ag precursor layer ($\leq$ 5% ([Ag]/[Ag]+[Cu])) for devices in this study.

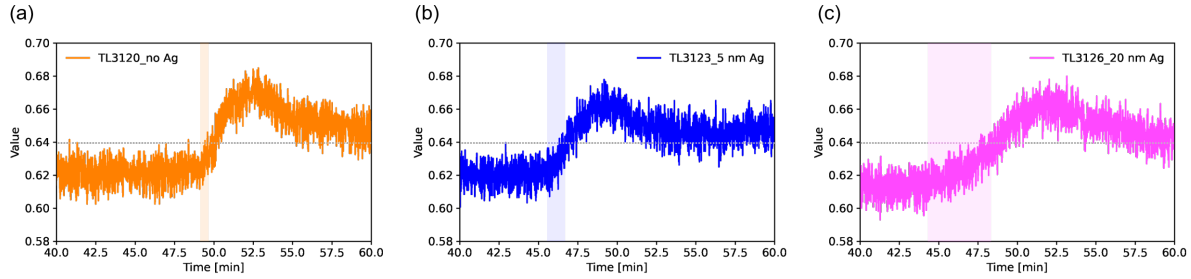

Figure 4.1: PID controller value change during the transition from Cu-poor to Cu-rich when having different thickness of Ag precursor layer (a) 0 nm (b) 5 nm (c) 20 nm. The intersection of the horizontal dash lines and the output curves define the end of the shadow regions, which corresponds to the moment when the Cu source temperature is reduced.

4.3 Material characterization

4.3.1 Microstructure

Fig. 4.2 shows SEM cross-sectional images for CIGS solar cell fabricated by three-stage process employing Ag precursor layer of 0 to 15 nm thickness. With increased Ag amount, the grain size of the absorbers increases significantly, which can be correlated to enhanced elemental diffusion by Ag during the CIGS grain growth. In addition, smaller grain size commonly caused by high GGI ratio near the back interface (as discussed in Chapter 3) also disappeared when introducing enough Ag into the absorber. Less defect and reduced recombination can be expected in this region, which is beneficial when high Ga back grading is required. **Fig. 4.3** shows a lower magnification SEM cross-sectional image of the absorber with 15 nm Ag precursor layer, which confirms the larger grain size in long range.

4.3.2 Elemental distribution

Since Ag was introduced with precursor layer method instead of co-evaporation, the non-uniform distribution of Ag throughout the absorber depth might be a potential issue especially when the Ag amount increases. **Fig. 4.4** shows the distribution of Ag from the SIMS depth profiling. Ag is rather uniform throughout all the absorbers despite precursor

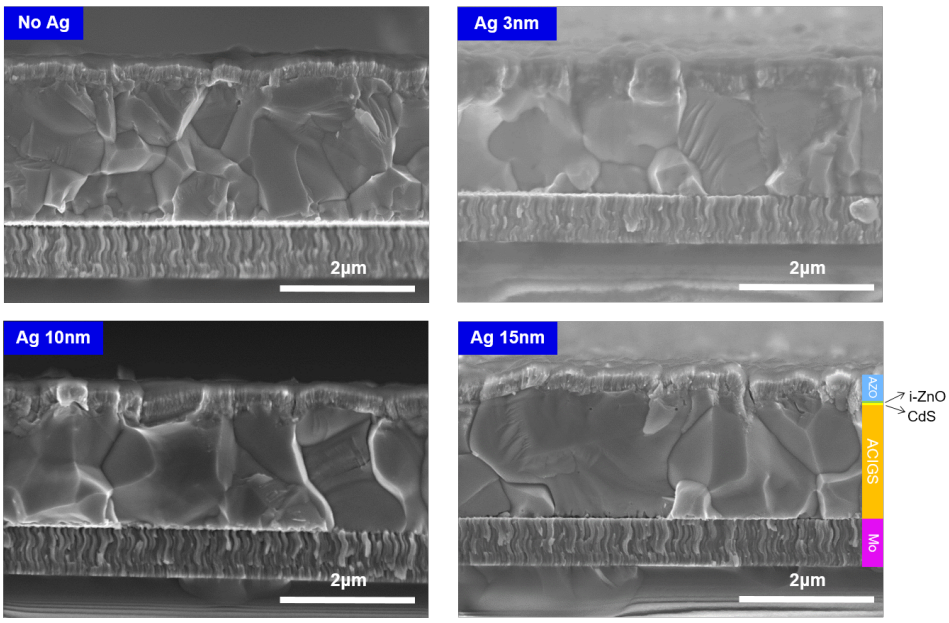

Figure 4.2: Cross-sectional images captured by SEM for the (A)CIGS devices with absorbers processed with different thickness (0 nm, 3 nm, 10 nm and 15 nm) of Ag precursor layer.

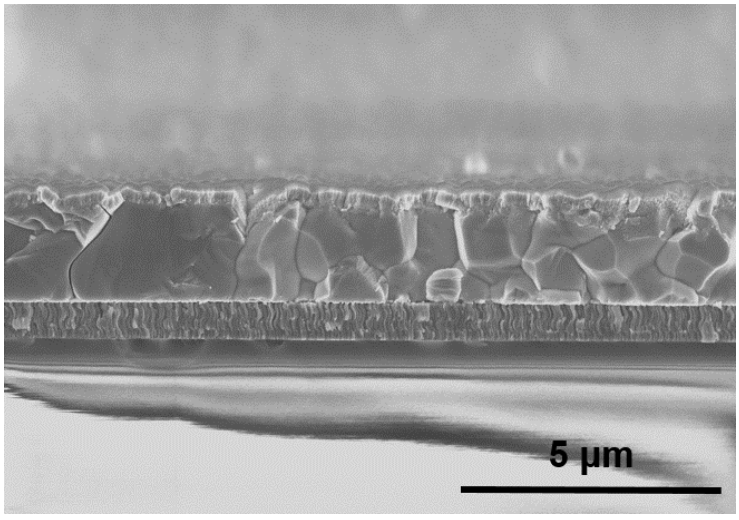

Figure 4.3: Cross-sectional images captured by scanning electron microscopy in low magnification of an ACIGS device with absorbers processed with 15 nm of Ag precursor layer.

layers being initially present as metal layers.

GGI gradings have a strong impact on the CIGS device performance as discussed in Chapter 3. Therefore, it is important to understand how the GGI gradings are modified when adding Ag. **Fig. 4.5** shows the GGI depth profiles for absorbers grown by the three-stage process employing Ag precursor layer of 0 to 30 nm. With increased Ag amount,

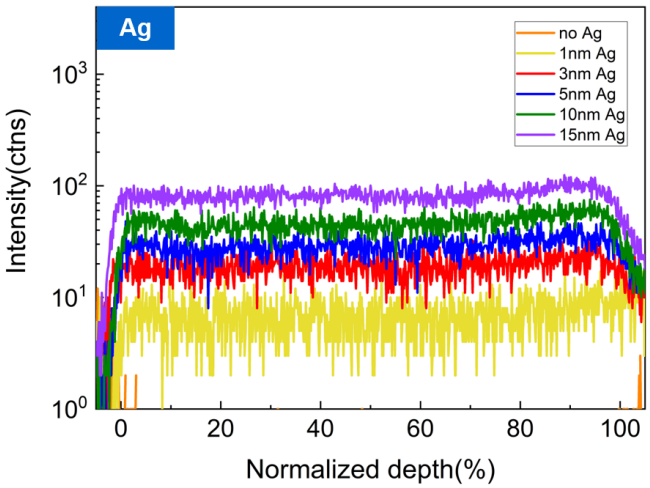

Figure 4.4: SIMS depth profiling of Ag for absorbers processed with different thickness (0 nm, 1 nm, 3 nm, 5 nm, 10 nm and 15 nm) of Ag precursor layers. The thickness of the absorbers are normalized (left: CdS, right: Mo).

both front and back gradings were slightly reduced because of increased inter-diffusiton. This observation is in line with what has been reported [55]. The V-shape notch evolves into wider flat-bottom notch when increasing Ag. With the SEM cross-sectional images shown before, it can be understood by the fact that the Ag precursor layer facilitated elemental diffusion during the CIGS deposition.

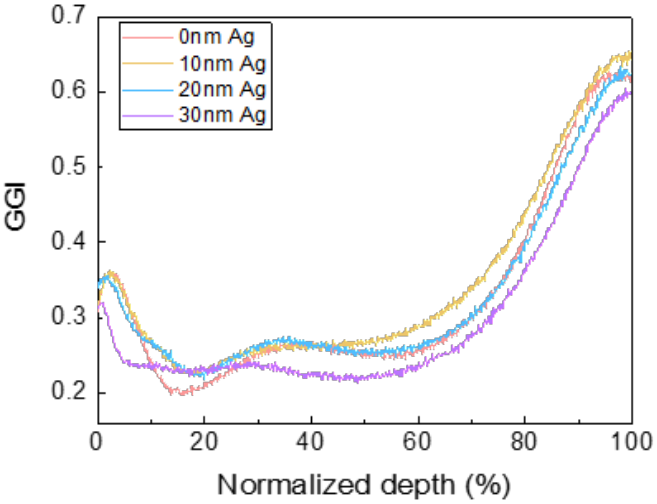

Figure 4.5: GGI depth profiles for (A)CIGS absorbers processed with different Ag precursor layer thickness (0 nm, 10 nm, 20 nm and 30 nm).The thickness of the absorbers are normalized (left: CdS, right: Mo).

Apart from GGI depth profiles, both Na and Rb distribution also play a vital role on device performance. **Fig. 4.6** shows Na and Rb distribution in the absorbers from SIMS profilings. With more Ag, the Na amount at front interface and in the bulk reduced, while remaining similar at back interface. This observation can be explained by larger grain size, i.e. less grain boundary, as observed in SEM images. On the other hand, the Rb amount at front interface and back interface increased while no clear trend was found in the bulk.

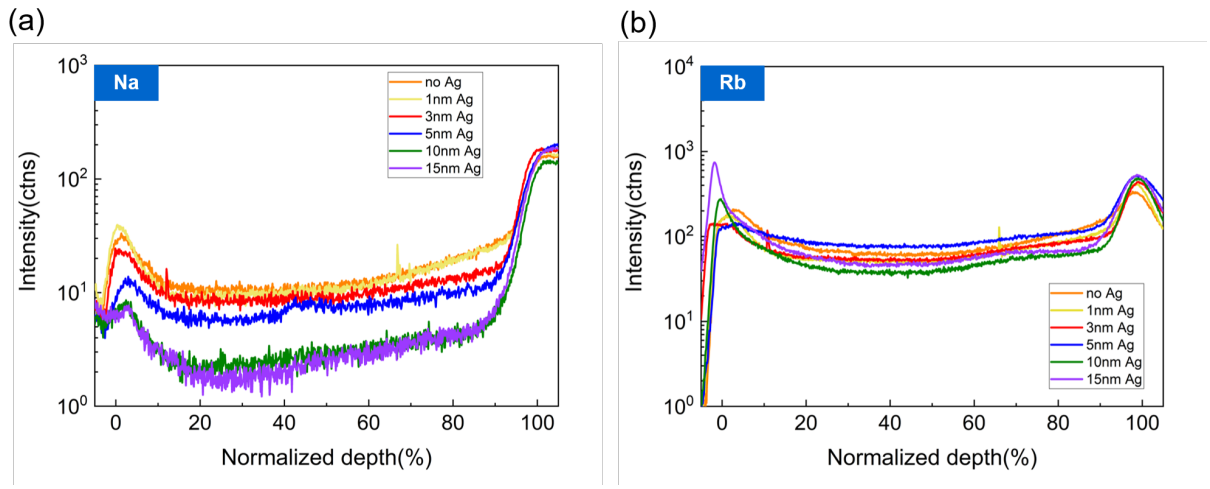

Figure 4.6: Na depth profilings for absorbers processed with different thickness (0 nm, 1 nm, 3 nm, 5 nm, 10 nm and 15 nm) of Ag precursor layer. The thickness of the absorbers are normalized (left: CdS, right: Mo).

4.3.3 Crystal structure and preferred orientation

Despite an uniform distribution of Ag throughout the absorber depth, it is not clear if Ag is actually alloyed into CIGS or just accumulated somewhere, for example, in the grain boundaries. Therefore, we performed XRD under θ-2θ mode on the absorbers to understand the influence of Ag on the changes in crystal structure and preferred orientation. As displayed in **Fig. 4.7**, all the absorbers exhibit a chalcopyrite structure, evidencing by presence of diffraction peaks of (112), (220)/(204), and (312)/(116) planes. No noticeable appearance of new peaks were spotted.

There are three main findings when adding more Ag: First, the preferred orientation of the grains was changed, as shown in **Fig. 4.8**. There must be a different growth mechanism

with the presence of Ag. Second, the (112) peak shifts to lower 2θ value, which corresponds to a larger (112) plane spacing and lattice constant and can be well explained by a larger radius of Ag than Cu. It proves that Ag alloys into CIGS crystal and occupies Cu lattice position instead of just accumulating somewhere else, e.g. grain boundaries. Third, the full width at half maximum (FWHM) of the (112) peak becomes narrower, as also shown in **Fig. 4.8**, which is consistent with larger grain size observed in the absorbers by SEM cross-sectional images.

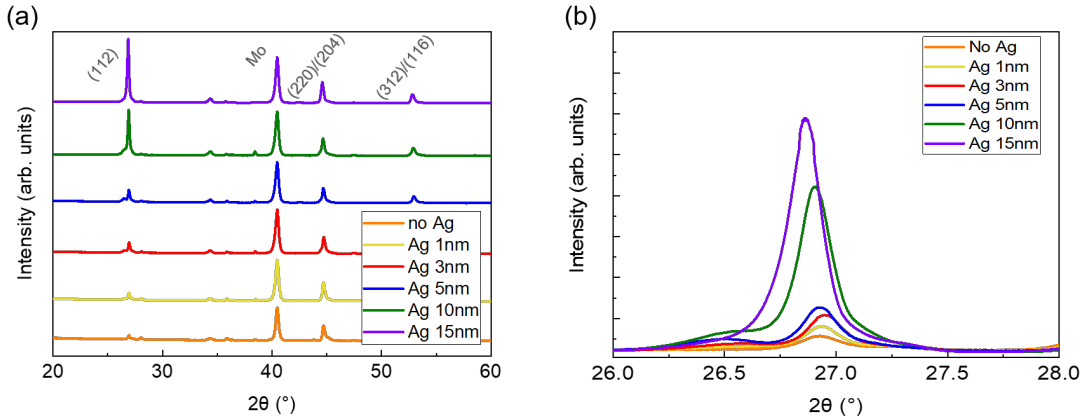

Figure 4.7: XRD measurements in θ-2θ mode for (a) broad scans and (b) fine scan of (112) peak for absorbers processed with different thickness (0 nm, 1 nm, 3 nm, 5 nm, 10 nm and 15 nm) of Ag precursor layer.

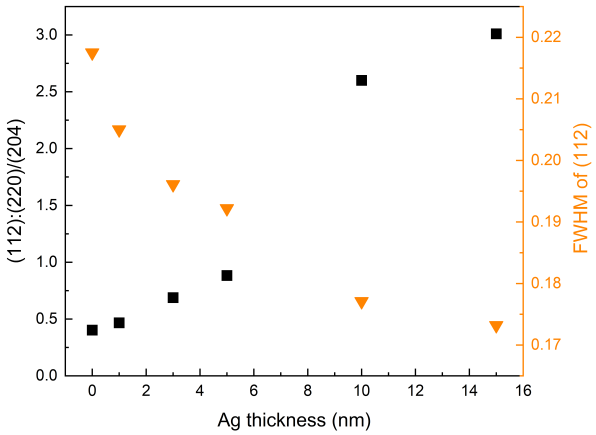

Figure 4.8: The peak intensity ratio (112):(220)/(204) and FWHM of (112) peak versus dufferent Ag precursor layer thickness in precursor layer method.

4.4 Device characterization

4.4.1 J-V parameters

The P-V parameters for devices fabricated with different thickness of Ag precursor layer are summarized in box plots, as shown in **Fig. 4.9**. The bar plot of the calculated V_{OC} deficit is also overlayed with V_{OC} box plot. Compared with the CIGS baseline devices (0 nm), the PCEs of the ACIGS devices were improved significantly, especially when 10 nm and 15 nm of the Ag precursor layer are used. The main driving force of higher PCE is reduced V_{OC} deficit and improved FF. Reduced V_{OC} deficit can be explained by larger grain size and better morphology observed in SEM cross-sectional images, which results in reduced defects and less recombination. The improvement in FF can be explained by the modified GGI profiles. If the notch is too deep, it can become a source of electron extraction barrier under light illumination, increasing the chance of carrier recombination. With less pronounced notch, the photoelectrons could be extracted effectively toward the TCO layer, giving rise to an increasing of FF. However, the change in J_{SC} is not clear and can be attributed to the drift of the bandgap between different absorbers. The J-V curves for the best cells with and without Ag are shown in **Fig. 4.10**. The PCE was improved by 1.5% by introducing 10 nm of Ag precursor layer.

4.4.2 Urbach energy

To understand the influence of Ag on the structural and electronic defects, the Urbach energy from the devices fabricated with different Ag thickness is also provided, as shown in **Fig. 4.11**. By increasing the thickness of Ag to 15 nm, Urbach energy is reduced from around 19 meV to 16 meV.

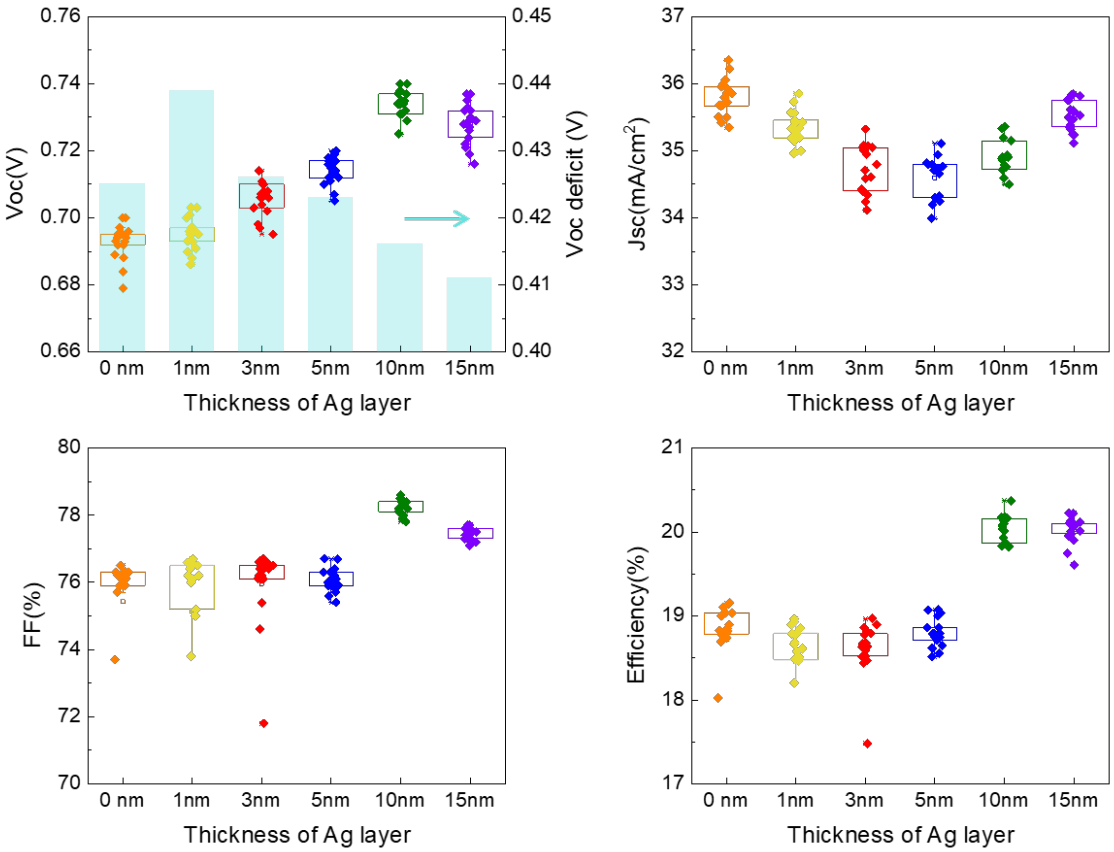

Figure 4.9: Box plots for J-V parameters of solar cells with absorbers fabricated with different thickness (0 nm, 1 nm, 3 nm, 5 nm, 10 nm and 15 nm) of precursor layer. The corresponding V_{OC} deficits are also displayed with a bar plot with the V_{OC} box plot

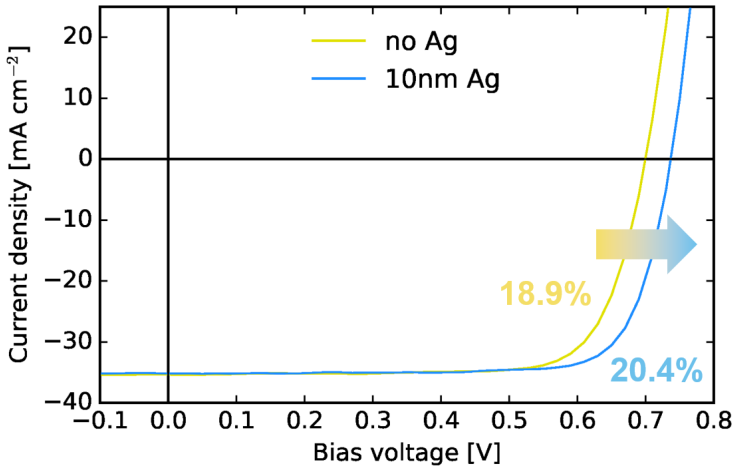

Figure 4.10: J-V curves for CIGS devices with and without Ag alloying.

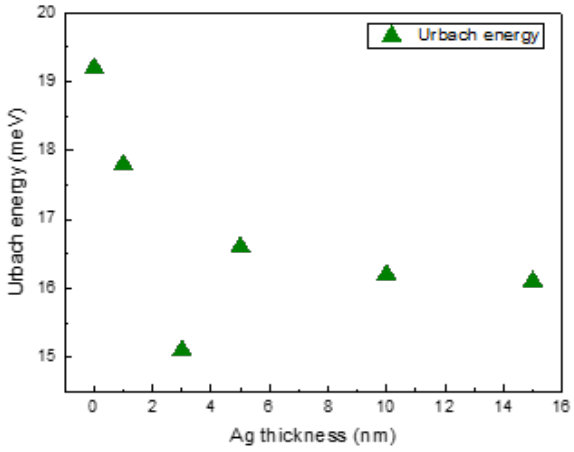

Figure 4.11: Urbach energy of solar cells with absorbers fabricated with different thickness (0 nm, 1 nm, 3 nm, 5 nm, 10 nm and 15 nm) of precursor layer.

4.5 Additional material and device characterization

4.5.1 In-plane stress analysis

The residual stress in the absorbers is an important parameter because of possible failure issues like cracking, buckling and delamination, especially for flexible applications. Herein, we performed residual stress analysis in XRD to evaluate how alloying with Ag changes the in-plane residual stress in the films. The analysis was carried out on the (112) reflection measured with different ψ angles, which is defined as the angle between the scattering vector and the sample's normal direction. The residual stress in the films is calculated from the magnitude and direction of the peak shifts. The details can be found in Section 2.5.5.

Fig. 4.12 illustrate how the (112) peak of ACIGS and CIGS absorbers shift as a function of the ψ angles. Peaks of both samples shift to high 2θ values with increasing ψ (compressive stress), but the shift is smaller for ACIGS than for CIGS absorbers. This indicates smaller compressive stress in ACIGS films. Our hypothesis for this behaviour is that Ag helps to release the residual stress by enhanced elemental diffusion and grain growth. This makes ACIGS absorbers even more promising for a variety of flexible PV applications, for which adhesion issues are critical.

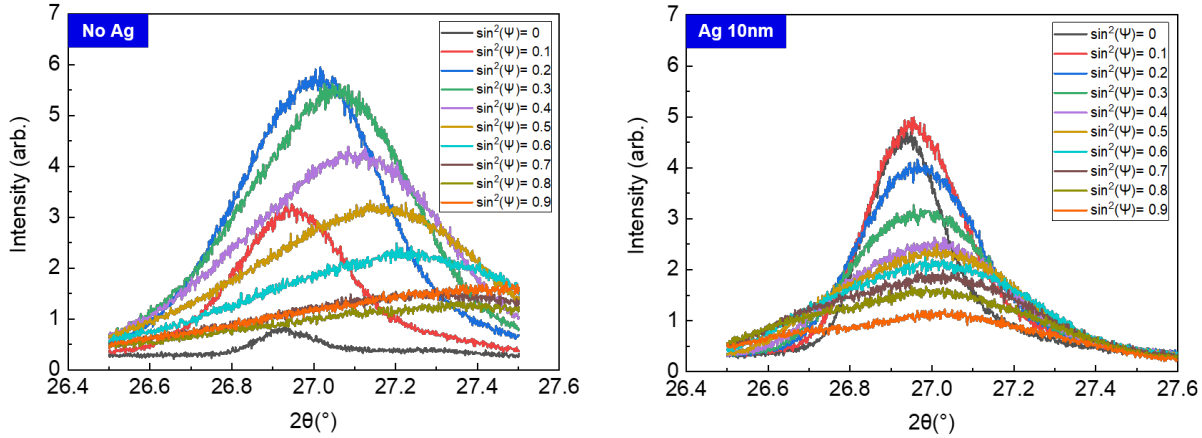

Figure 4.12: Residual stress measurement for absorbers with different thickness (0 nm and 10 nm) of Ag precursor layer.

4.5.2 Carrier concentration with C-V measurement

It has been reported that Ag-alloyed CIGS has a reduced carrier concentration [54, 103]. However, AAC ratios of more than 10% were used in most of those works. Here, we perform C-V measurement to see if reduced carrier concentration is also observed when AAC ratio is around 4-5%. As shown in **Fig. 4.13**, a 50% reduction in carrier concentration can be seen in ACIGS absorbers with an AAC of around 5%, as compared to regular CIGS. The width of the space charge region is also extended as expected from lower carrier concentration.

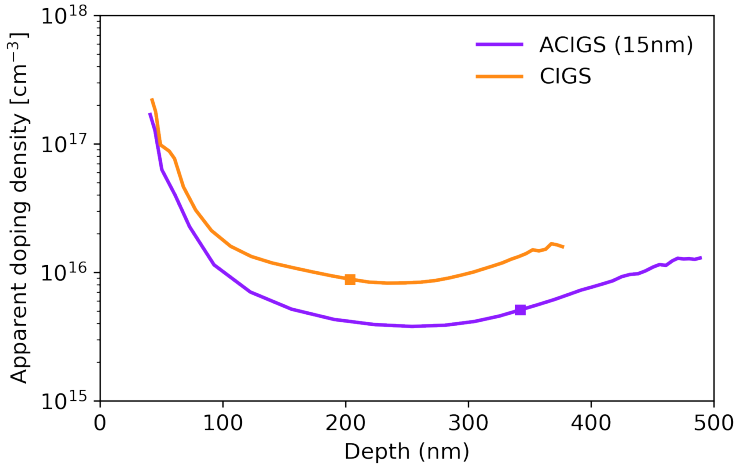

Figure 4.13: Apparent doping profiles from the C-V measurements.

4.5.3 Raman spectra for the formation of $MoSe_2$

For CIGS solar cells, a Schottky barrier for the holes is expected to form at the CIGS/Mo interface. However, such barrier is typically not observed in high performance Mo-based CIGS devices due to the formation of the $MoSe_2$ interlayer during the deposition. The presence of the thin $MoSe_2$ layer reshapes the barrier and allows the tunneling of the holes across the interface, turning Schottky barrier into a quasi-Ohmic contact [104]. However, using Ag precursor layer method raises the doubt if the presence of metallic Ag in the early stage of the co-evaporation would hinder the formation of $MoSe_2$.

$MoSe_2$ is a layered-material and can be detected by Raman spectroscopy. **Fig. 4.14** shows all the possible vibration modes in $MoSe_2$ films. Those vibrations can serve as the "fingerprint" for identifying $MoSe_2$. Therefore, we delaminated CIGS and ACIGS devices from Mo substrates and performed Raman measurements on each side to unveil the presence of $MoSe_2$ on either delaminated side.

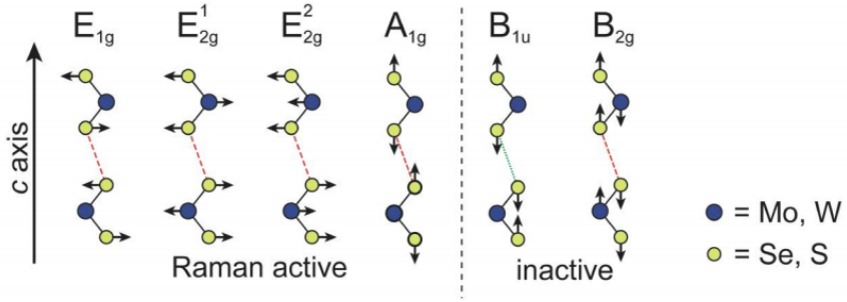

Figure 4.14: Raman active and inactive vibrations in (Mo,W) and (Se,S) two-dimentional layers. Reproduced from Tonndorf et al.[105]

After delamination, we performed Raman measurements on both Mo and ACIGS side, as shown in **Fig. 4.15**. We found all Raman active peaks on Mo substrate side for both CIGS and ACIGS while only A1 peak of CIGS was observed on delaminated absorbers. It shows that Ag precursor layer method at least with less than 15 nm doesn't hinder the formation of $MoSe_2$, explaining why we don't evidence transport issues from J-V curves.

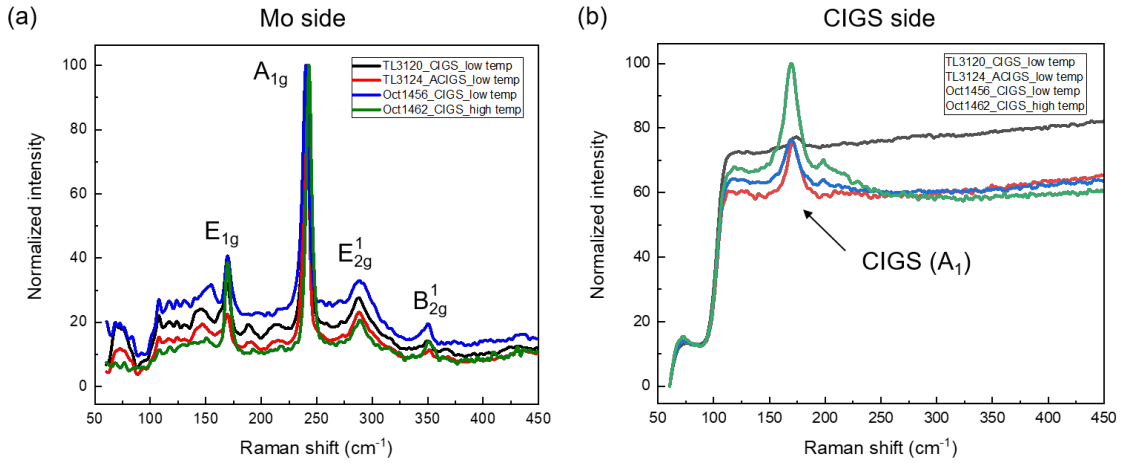

Figure 4.15: (a) Raman shifts on Mo substrates after delaminating CIGS and ACIGS devices. (b) Raman shifts on absorber side after delaminating CIGS and ACIGS devices.

4.6 Thermodynamic and kinetic stability

It has been reported that Ag-alloyed CIGS might suffer from the thermodynamic instability at room temperature, especially when GGI is high [106], as depicted in **Fig. 4.16**. However, phase separation not only depends on thermodynami instability but also kinetic instability. The decomposition can not occur in practice because of slow transformation kinetics at room temperatures. This is actually the case for CIGS absorbers. Even though Ag-free CIGS absorbers with a GGI of 0.3 at 50°C locates within spinodal lines in **Fig. 4.16** (thermaldynamic unstable), in reality the decomposition doesn't happen due to limited kinetics.

In previous sections, it has been shown that the presence of Ag promotes the elemental diffusion and grain growth during deposition, which raises the concern of changing the decomposition kinetics in ACIGS absorbers. Herein, we monitored the J-V performance of ACIGS solar cells for one year to understand the short-term stability uopn room temperature storage. As shown in **Fig. 4.17**, there is no obvious degradation in device performance, possibly because an AAC of 5% barely change the decomposition kinetics. However, it is still worthy to investigate its long-term stability in the future.

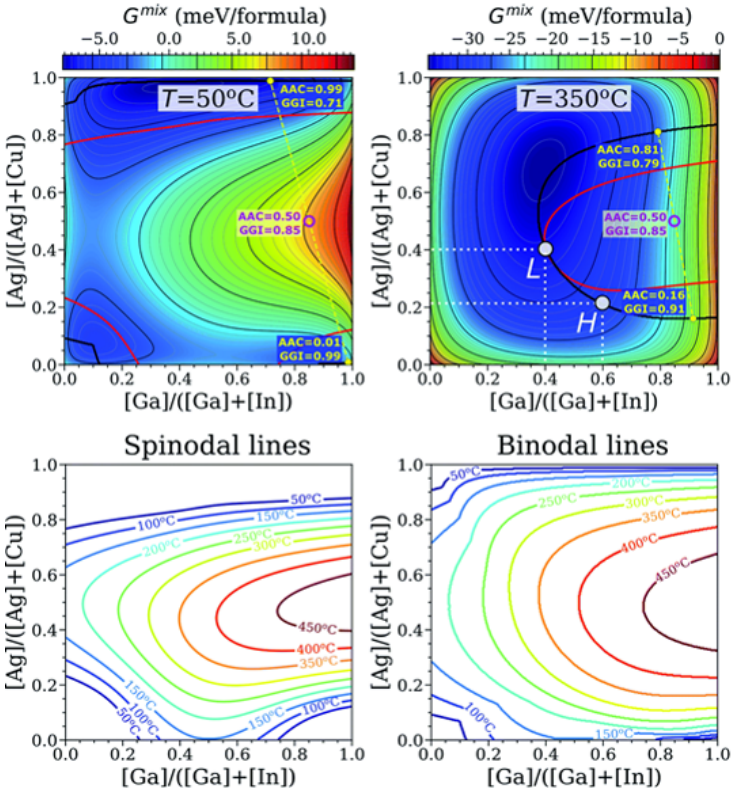

Figure 4.16: Thermodynamic stability of ACIGS alloy at different temperatures. Reproduced from Sopiha et al.[106]

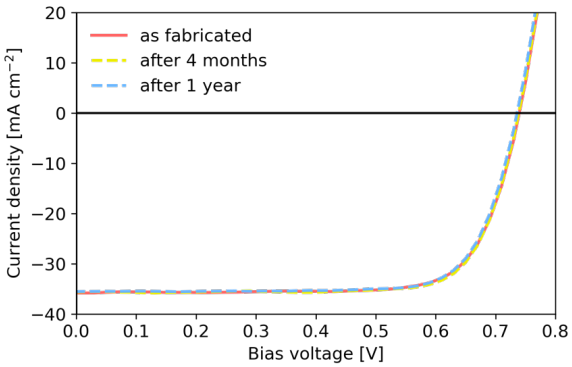

	V_{OC} (mV)	J_{SC} (mAcm^{-2})	FF (%)	PCE (%)
as fabricated	740	35.8	75.8	20.1
after 4 months	739	35.7	77.0	20.3
after 1 year	736	35.5	76.6	20.0

Figure 4.17: The J-V curves of ACIGS devices processed with 15 nm Ag precursor layer: as fabricated, after 4 months and after 1 year.

4.7 The role of Ag during grain growth

By utilizing the Ag precursor layer method, the film initiates from a group-I rich state, which is immediately followed by a group-I poor state during the first stage. This transition

is different from standard three-stage process, which starts directly from group-I poor state. Despite it is likely to have an impact on the nucleation of grains and possibly also on the texture of the films, more refined experiments such as real-time X-ray diffraction [37] are required in order to reveal the evolution of the crystal structure during film growth.

However, based on an internal study conducted by Dr. Shiro Nishiwaki within the same research group, it appears unlikely that the initial group-I rich state with precursor layer method is solely responsible for the enhanced device performance. In **Table 4.1**, a comparison of the J-V parameters for three samples with similar [I]/[III] ratios of 0.88 - 0.89, fabricated using different approaches - standard CIGS co-evaporation, Cu precursor layer method, and Ag precursor layer method - is provided. All the samples were provided by Dr. Shiro Nishiwaki, and the results indicate that there is no significant difference in device performance between the standard CIGS co-evaporation and Cu precursor layer method. However, the Ag precursor layer method outperforms the others, suggesting that the improvement is not due to the initial group-I rich state, but rather from Ag itself. Moreover, a comparison between Ag-precursor layer (starting from group-I rich) and co-evaporation methods (starting from group-I poor) in [8] shows no detectable differences, further supporting this conclusion.

Instead, it is more likely that the effect of Ag is particularly significant during the transition from the second to the third stage. When the process exceeds the stoichiometric point, i.e., (Ag + Cu)/(Ga + In)> 1, the grain size of the film is substantially increased. At this stage, either Ag or Cu should segregate out to the grain boundary. Unlike Cu-Se binary system that starts to form through the liquid phase of $Cu_{2-x}Se$ at 523°C [107] as shown in **Figure 4.18**, the Ag-Se system can form a $Ag_{2-x}Se$ liquid phase at much lower temperature of 221°C [108] under the oversupply of Se, as shown in **Figure 4.19**. The

Table 4.1: A comparison of the best P-V parameters among samples fabricated using different deposition approaches, all of which were fabricated by Dr. Shiro Nishiwaki. The data presented here has been authorized for sharing by Dr. Shiro Nishiwaki.

PDT	Deposition method	V_{OC}(V)	J_{SC}(mA/cm^2)	FF (%)	PCE (%)
Na PDT	standard co-evaporation	0.684	34.36	75.79	17.76
	Cu 10.3 nm	0.684	34.18	74.16	17.33
	Ag 15 nm	0.699	34.33	76.11	18.27

liquid $Ag_{2-x}Se$ phase at grain boundaries might provide mobile channels for atom diffusion, and Ga can easily diffuse toward the film surface along the grain boundaries, facilitating the CIGS recrystallization process throughout the film. [55]

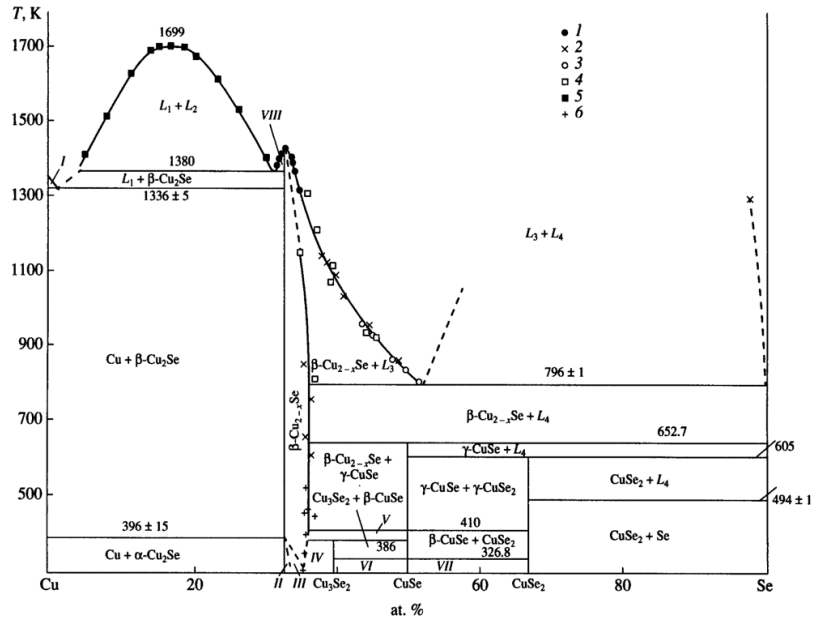

Figure 4.18: Cu-Se phase diagram, reproduced from [107].

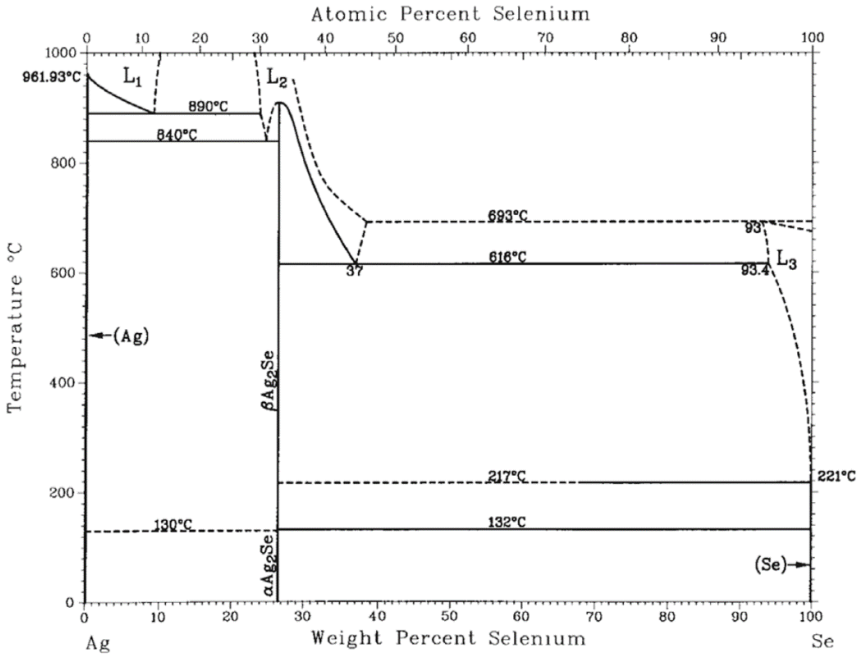

Figure 4.19: Ag-Se phase diagram, reproduced from [108].

4.8 From rigid to flexible substrates

Adding Ag into the absorbers can result in a different adhesion strength of the absorbers to the substrates. Also, precursor layer method can change the early stage of the absorber deposition onto the substrates. In particular, the adhsion issue becomes more pronounced on flexible substrates. Therefore, we try to fabricate ACIGS solar cells with Ag precursor layer method on polyimide (PI) substrates as well.

Fig. 4.20(a) shows the SEM cross-sectional images for ACIGS devices on both glass and PI substrates. There is no noticeable difference in view of the morphology and the microstructure betweem glass and PI substrates. In **Fig. 4.20(b)**, the J-V curves of the best cell on glass and PI are also provided. Similar device performance is obtained and the PCE for both types of substrates are higher than 20%.

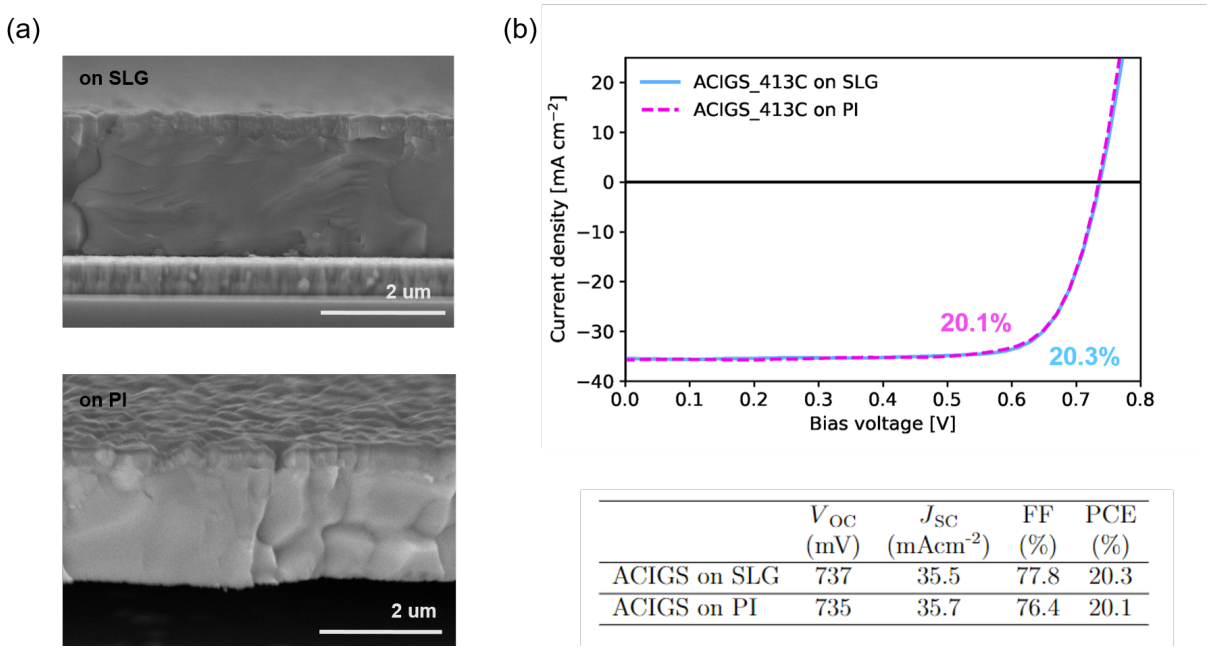

	V_{OC} (mV)	J_{SC} (mAcm^{-2})	FF (%)	PCE (%)
ACIGS on SLG	737	35.5	77.8	20.3
ACIGS on PI	735	35.7	76.4	20.1

Figure 4.20: (a) SEM cross-sectional images of the ACIGS devices on glass and PI substrates. (b) The J-V curves of the best cell of ACIGS devices on glass and PI substrates.

4.9 Conclusion

Alloying small amount of Ag (ACC: 4-5%) into CIGS absorbers improves the overall device performance significantly, which is mainly due to the reduction of the V_{OC} deficit and the increase of FF. Compared with the reference CIGS devices, the PCE of the champion cell for ACIGS devices was improved from 18.9% to 20.4%. From the material properties point of view, Ag not only increases the grain size but also changes the preferred orientation of the grains. In addition, enhanced elemental inter-diffusion is also observed from SIMS depth profilings, which can be linked to the better morphology observed in ACIGS absorbers. In-plane compressive stress was reduced in ACIGS absorbers, which can be beneficial for the applications on flexible substrates. Despite the presence of the metallic Ag layer in the early stage of the CIGS deposition, the formation of the $MoSe_2$ layer at ACIGS/Mo interface is still evidenced, which ensures the quasi-Ohmic contact between ACIGS and Mo back contact in finished devices.

The short-term device stability of ACIGS devices were monitored, as it has been reported by simulation that Ag might worsen the thermodynamic stability of the devices. After one year, no evident degradation in device performance was observed, hinting that ACIGS absorbers with low AAC are kinetically stable upon storage at room temperature. However, long-term stability of the ACIGS devices is still worthy of further investigating.

We have successfully shown that Ag precursor layer method can be easily implemented into our current CIGS co-evaporation system without hardware modification and major process change. Finally, we implemented Ag precursor layer method on PI substrates and similar device performance was obtained, with a PCE of 20.1% from the champion cell.

4.10 Sample references

Ag amount	no Ag	Ag 1nm	Ag 3nm	Ag 5nm	Ag 10nm	15nm
Sample	TL3120	TL3121	TL3122	TL3123	TL3124	TL3125

Table 4.2: Internal sample naming for ACIGS solar cells in Chapter 4

5 Silver promoted low-temperature process

This chapter is adapted from the publication:

Yang, S. C., Sastre, J., Krause, M., Sun, X., Hertwig, R., Ochoa, M., Tiwari, A. N., and Carron, R. (2021). *Silver-Promoted High-Performance (Ag,Cu)(In,Ga)Se_2 Thin-Film Solar Cells Grown at Very Low Temperature*, Solar RRL, 5(5), 2100108. [109]

My own contribution to this publication consisted in: design of the experiments, deposition of CIGS thin films, completion of working solar cells, measurement and analysis of: SIMS, XRF, J-V, EQE, TRPL (in collaboration with Xiaoxiao Sun and Mario Ochoa), and data interpretation. Residual stress measurmeent was performed by Jordi Sastre. SEM was performed by Maximilian Krause.

5.1 Introduction

In Chapter 4, ACIGS has shown improved material properties and better device performance as compared to CIGS devices. Furthermore, low temperature grown ACIGS solar cells show comparable device performance with high temperature grown CIGS solar cells [53], showcasing the possibility of further reduction of ACIGS absorber deposition temperature. However, most studies so far have focused on high deposition temperatures

($\geq$550 °C) and the lower bounds for processing temperatures have not been investigated yet. In this chapter, we take advantage of the aforementioned properties of ACIGS absorbers to explore the processing temperature limits for high performance ACIGS solar cells. The changes in the solar cell performances are discussed in relation to changes in morphology and the opto-electronic properties of the absorbers investigated by SEM, EQE, Urbach tails and TRPL. The influence of Ag on the elemental kinetics during growth would also be discussed via SIMS depth profilings.

5.2 Device performance with low-temperature process

We use the Ag precursor layer method developed in Chapter 4 to alloy Ag and modify the nominal substrate temperature (T_{sub}) of (A)CIGS absorbers in a wide range (from 413 °C to 253 °C), which is measured by thermocouple, in order to assess the beneficial effects from Ag. The nominal T_{sub} of 413 °C corresponds to about 450 °C actual substrate temperature (about 37 °C difference). For T_{sub} below 413 °C, we expect a slightly smaller difference between T_{sub} and the actually substrate temperature.

Figure 5.1 summarizes the J-V parameters of ACIGS and CIGS solar cells with absorbers grown at different T_{sub}. The J-V curves for devices fabricated at 413 °C and 303 °C are shown in **Figure 5.3**. The missing result from CIGS devices fabricated at 253 °C was due to the failure of end-point-detection, which will be discussed in **Section 5.5**. As shown in **Figure 5.1**, the efficiency of CIGS solar cells decreases progressively and drops significantly for T_{sub} <353 °C, mainly because of the reduced V_{OC} and to a lesser extent due to reduced FF. On the contrary, the efficiency of ACIGS solar cells remains above 18.5% for T_{sub} above 303 °C, which is mainly driven by a lesser V_{OC} degradation as compared to CIGS solar cells. Furthermore, we see no clear downward trend in FF and J_{SC} for T_{sub} down to at least 303 °C in ACIGS. A distinct drop in both V_{OC} and FF is observed for ACIGS grown at 253 °C, resulting in a evident decrease in efficiency.

To exclude the influence of E_{g} variations between different samples, we further measured EQE (**Figure 5.4**) to determine the E_{g} value by linear extrapolation of the plot ((photon energy $\times$ EQE)^2 vs photon energy and calculated the V_{OC} deficit (E_{g}/q - V_{OC}), as shown

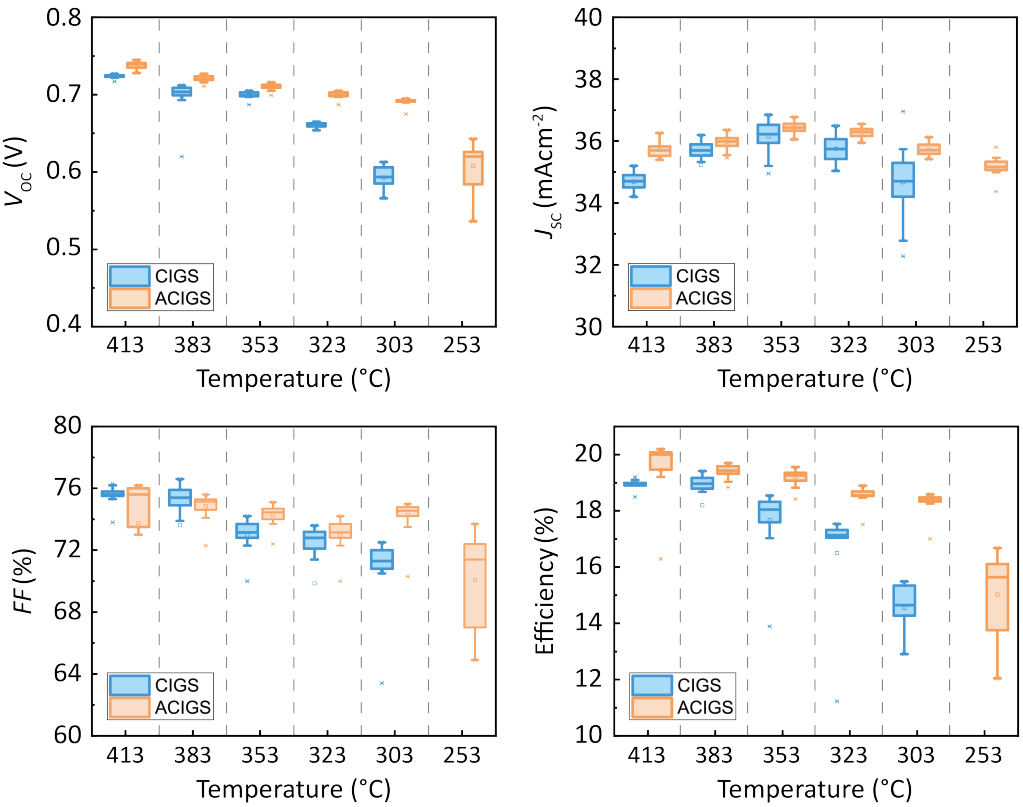

Figure 5.1: The J-V parameters of the (A)CIGS solar cells with absorbers grown at varying nominal T_{sub} from 413 °C to 253 °C. The CIGS absorber could not be synthesized at 253 °C

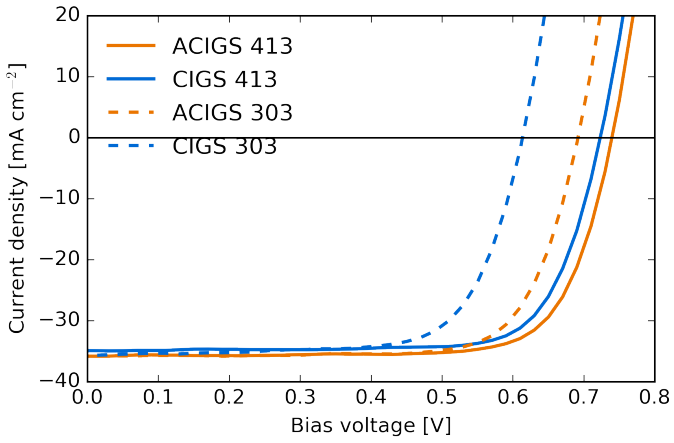

Figure 5.2: The J-V curves of the ACIGS (orange) and CIGS (blue) solar cells with absorbers grown at 413 °C and 303 °C.

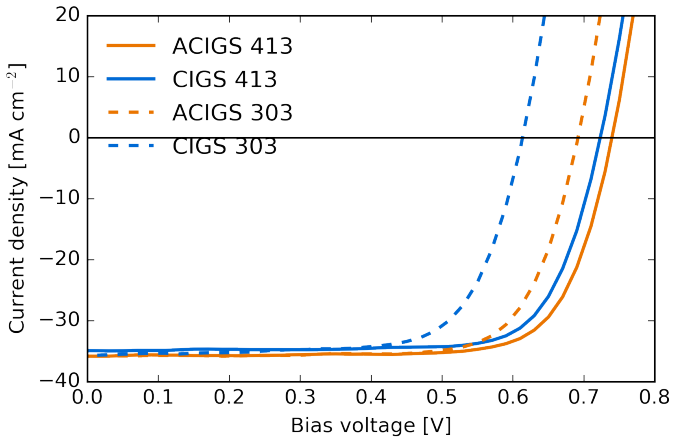

Figure 5.3: The J-V curves of the ACIGS (orange) and CIGS (blue) solar cells with absorbers grown at 413 °C and 303 °C.

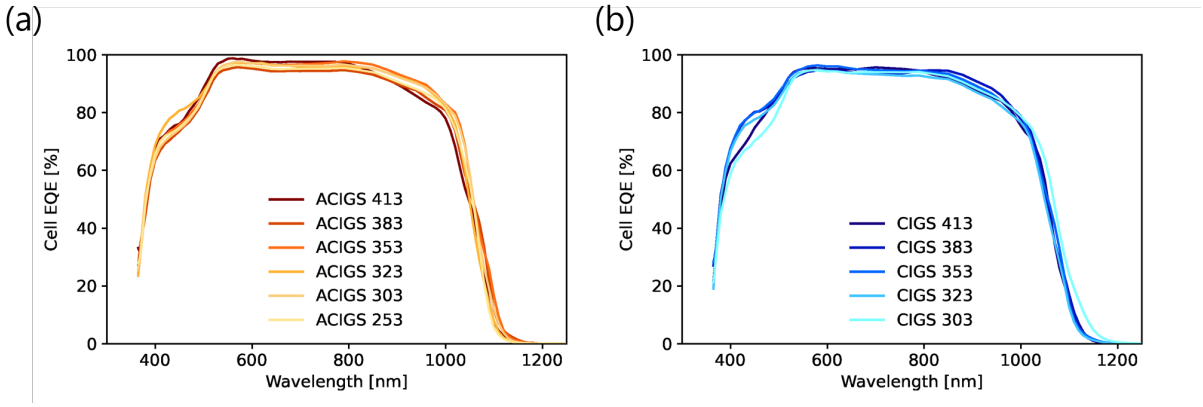

Figure 5.4: External quantum efficiency curves of the (a) ACIGS and (b) CIGS solar cells with absorbers grown at varying nominal T_{sub} from 413 °C to 253 °C.

in **Figure 5.5(a)**. For each T_{sub} investigated, ACIGS exhibits a lower $V_{\mathrm{OC,def}}$ as compared with that of CIGS.

Figure 5.5(b) shows the Urbach energy estimated from the quasi-exponential decay in the long wavelength edge of the EQE curves. For the CIGS solar cells, the E_{U} increases with lower T_{sub}. On the contrary, E_{U} of the ACIGS devices are almost independent from T_{sub}. And the E_{U} values of the ACIGS devices are always below or similar to these of CIGS devices, suggesting a lesser density of structural and electronic defects.

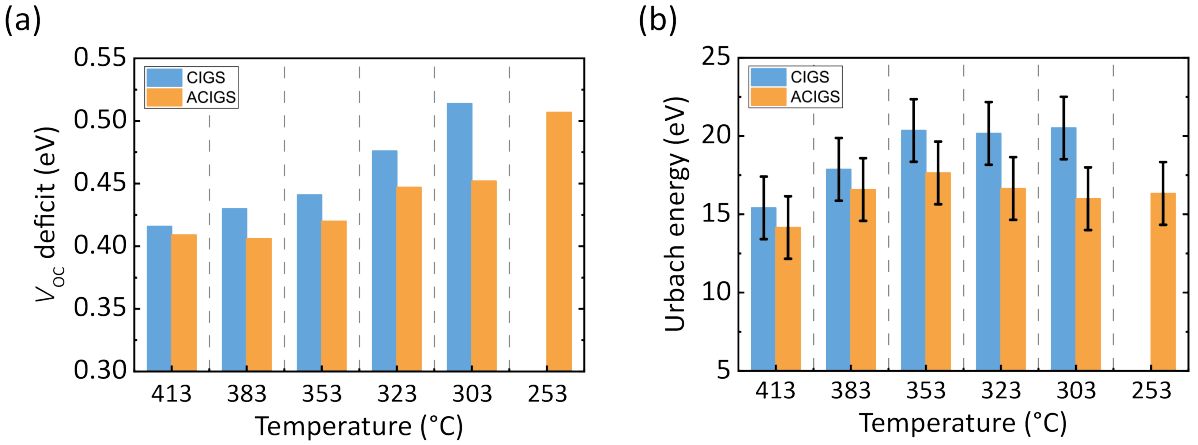

Figure 5.5: (a) $V_{OC,def}$ and (b) Urbach energy (E_U) of (A)CIGS solar cells with absorbers grown at different nominal T_{sub}.

5.3 Influence of T_{sub} on elemental distribution

The GGI depth profiles in **Figure 5.6(a)** show a moderate influence of Ag on the Ga gradings. Ag also slightly flattens the notch region and modifies the front grading. The comparatively weaker influence of Ag on the GGI depth profiles may be related to the lower AAC of 4-5% (as compared to commonly used 20% [56]) and the low T_{sub} ($\leq 450\,°C$) in our study. The SIMS measurements reveal that Ag distribution is uniform throughout the absorbers for all the investigated T_{sub} (see **Figure 5.6(b)**, including at the lowest T_{sub}.

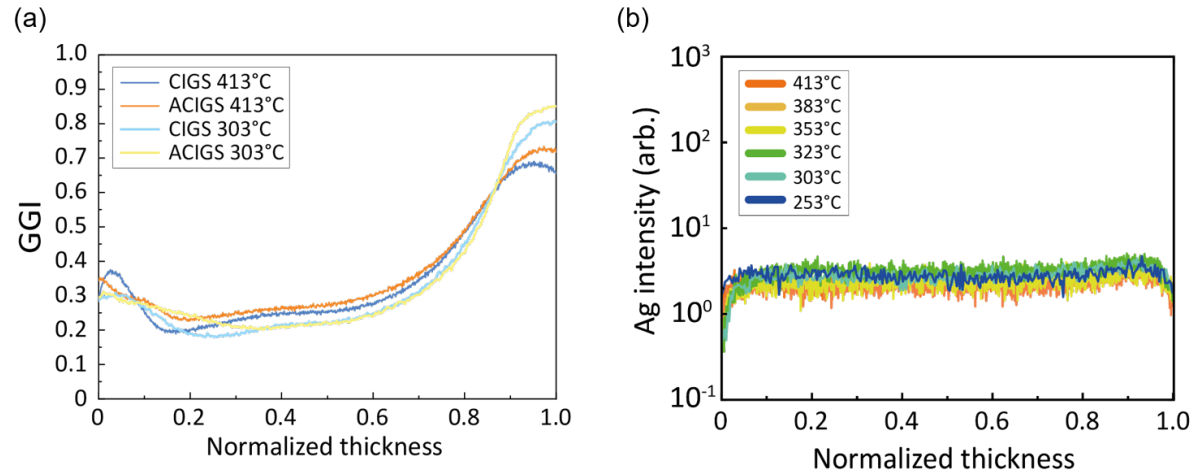

Figure 5.6: (a) GGI depth profiles for (A)CIGS absorbers grown at 413 °C and 303 °C. (b) Depth profiles of Ag in ACIGS absorbers grown at different nominal T_{sub}.

5.4 Influence of T_{sub} on microstructure

To understand the reason for the low $V_{OC,def}$ in ACIGS, the microstructure of the absorbers was imaged by cross-sectional SEM (**Figure 5.7**). We observe three main features of the absorber morphologies. First, ACIGS layers present larger grain sizes than CIGS layers for the same T_{sub}, as expected. Second, the typical small grain sizes found in the high GGI back region of

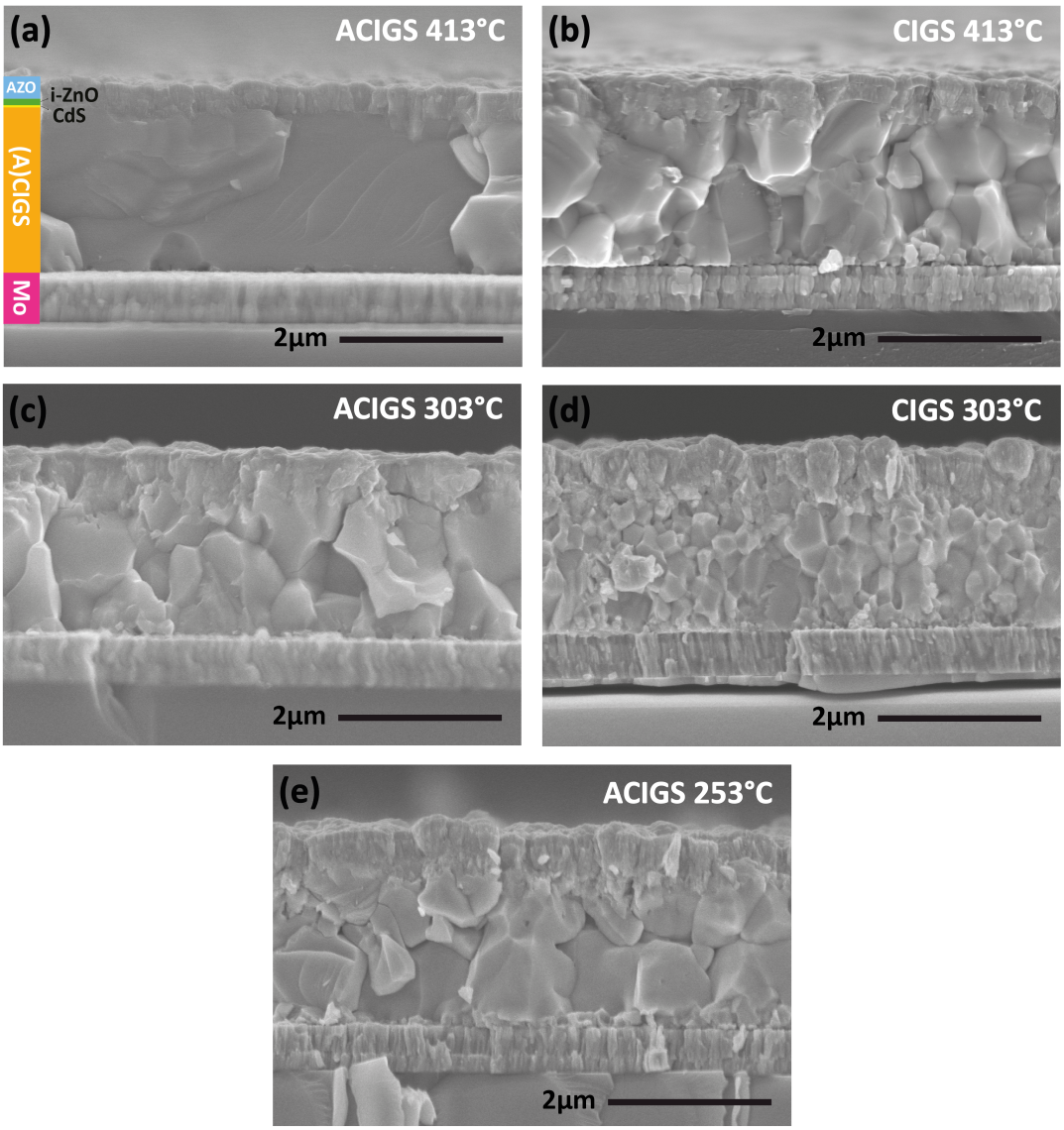

Figure 5.7: SEM cross-sectional images for ACIGS and CIGS absorbers grown at nominal T_{sub} of 413 °C, 303 °C and 253 °C

CIGS is not observed in the ACIGS layers grown at 413 °C. Ag improves the crystallinity even in the high Ga region. Last, the ACIGS layer grown at 253 °C exhibits a larger grain size and a better morphology than the CIGS grown at higher T_{sub} of 303 °C. Similar observations were previously reported between 580 °C grown ACIGS and 650 °C grown CIGS [53].

5.5 Failure of end-point-detection

The CIGS solar cells and layers deposited at 253 °C are missing throughout this chapter because of the failure of the 3-stage process. More specifically, the increase in the substrate heating regulation signal corresponding to the stoichiometric point could not be detected for CIGS grown at 253 °C, as shown in **Figure 5.8(b)**. In contrast, end-point-detection could still be detected for ACIGS grown at 253 °C, as seen in **Figure 5.8(a)**.

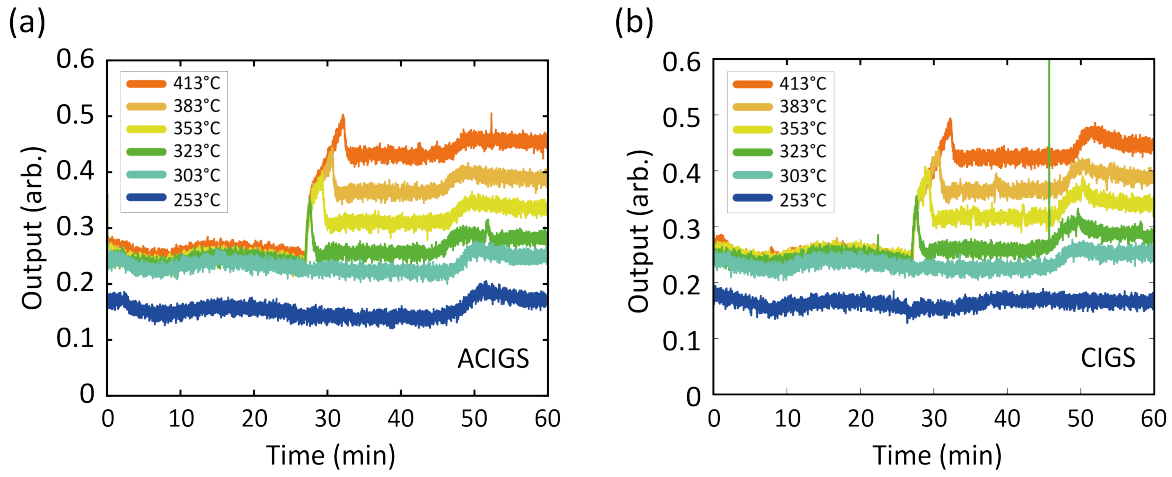

Figure 5.8: Output of the PID controller for the substrate heater during ACIGS and CIGS growth at different nominal T_{sub}. The temperature is increased at the beginning of the 2nd stage (at about 27 min). The first stoichiometric point occurs at around 45 to 50 min.

We further designed an experiment to understand the failure of end-point-detection for CIGS deposition at 253 °C. Two sets of (A)CIGS absorbers were prepared: The depositions were interrupted before the expected stoichiometric points and after the stoichiometric points. The (A)CIGS depositions were interrupted few minutes before and after the expected stoichiometric points arrived, i.e. the main shutter was closed and the substrates

were cooled down immediately followed by unloading. Later we performed SIMS depth profilng analysis on those absorbers in order to understand the kinetics of the elements during low-temperature growth. **Figure 5.9** shows the SIMS profiles for absorbers unloaded few minutes before (**Figure 5.9b**) and after (**Figure 5.9c**) expected stoichiometric point. Despite the supply of Cu in second stage at very low temperature, Cu was still able to diffuse deep inside the absorbers (both before and after stoichiometric point). In addition, it is worth noting that Ag was accumulated on the surface before stoichiometric point while distributing evenly after stoichiometric. This interesting observation still needs to be further investigated and correlated to the growth of ACIGS with precursor layer method.

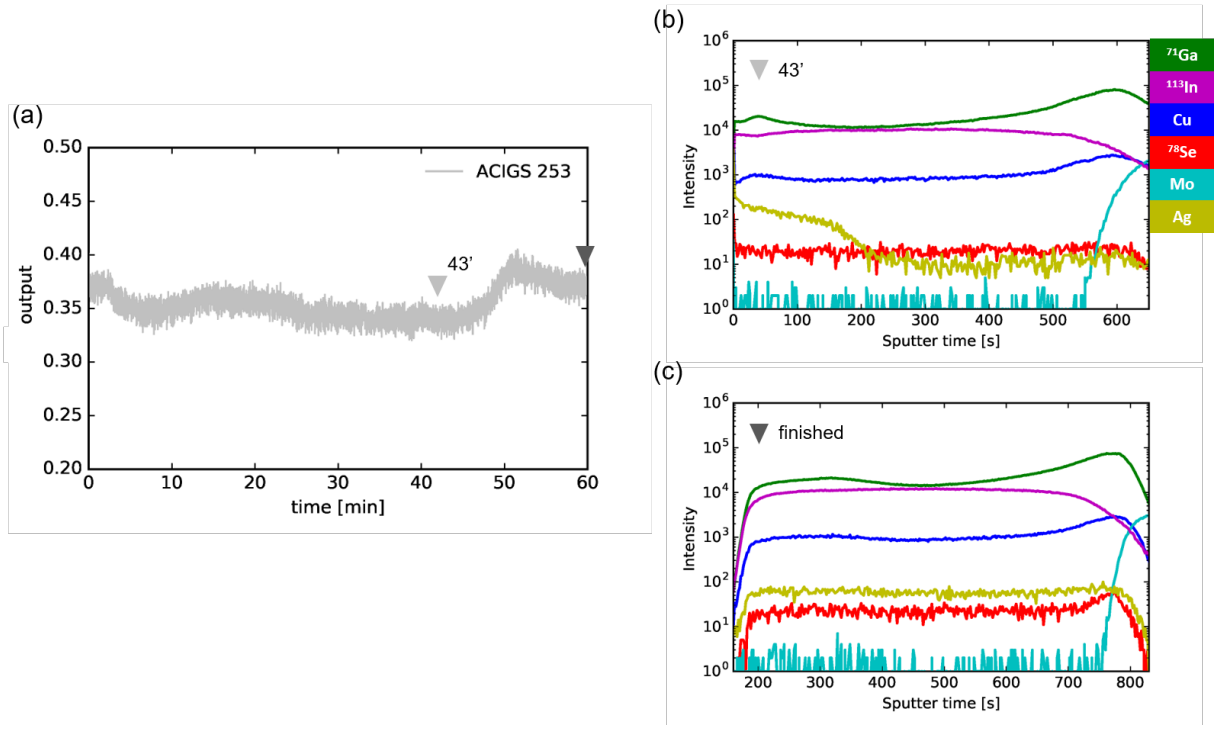

Figure 5.9: (a) Output of the power supply for the substrate heater during ACIGS growth at 253 °C. (b) Elemental distribution of the ACIGS absorbers grown at 253 °C with deposition interruption before detecting stoichiometric point. (c) Elemental distribution of the finished ACIGS absorbers grown at 253 °C.

However, the elemental kinetics of CIGS at low temperature seems very different from that of ACIGS. Similar experiment was performed with Ag-free CIGS, as shown in **Figure 5.10**. We clearly see that Cu strongly accumulated near surface in the second stage

before stoichiometric point. The inefficient Cu diffusion can result in the incomplete recrystallisation of the chalcopyrite phase and be responsible for the failure of end-point-detection. A similar behavior was already reported before [60]. This is because the Cu diffusion rate decreases: at low temperatures, Cu accumulates on the surface as a Cu-Se phase early in the deposition and is not available for the formation and recrystallisation of the chalcopyrite phase. The accumulation of Cu-Se phase on the surface can also explain the small increase in power output at around 32 minutes for the CIGS layer grown at 253 °C. On the contrary, the increase in power output is observed at around 47 minute in the case of ACIGS grown at 253 °C and the layer underwent recrystallization.

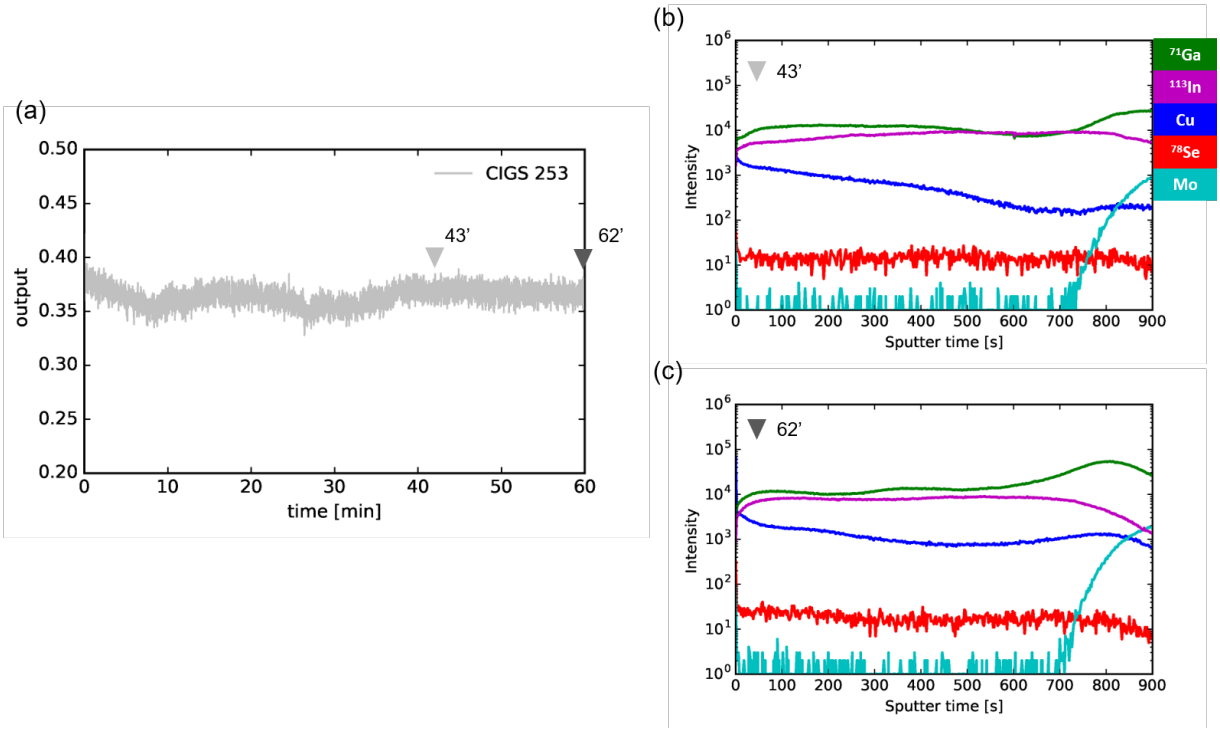

Figure 5.10: (a) Output of the power supply for the substrate heater during CIGS growth at 253 °C. (b) Elemental distribution of the ACIGS absorbers grown at 253 °C terminated before detecting (expected) stoichiometric point. (c) Elemental distribution of the ACIGS absorbers grown at 253 °C terminated after (expected) stoichiometric point.

By adding small amount of Ag, the Cu diffusion rate is increased, extending the lower bound for process temperature of absorber deposition. This lower bound of process temperature relates to the kinetics of Cu diffusion [39]. By increasing Cu diffusion kinetics in the layers during growth, the presence of Ag has the potential to help fast industrial pro-

cesses to achieve complete layer recrystallization with minimized Cu excess requirement.

5.6 V_{OC} loss analysis with TRPL measurements

We performed TRPL measurements to get insights on the electronic properties and carrier dynamics in the (A)CIGS absorbers. **Figure 5.11** displays selected TRPL decays from different absorbers. The decays were fitted with a two-exponential formula ($Y = A_1 \exp(-\frac{t}{\tau_1}) + A_2 \exp(-\frac{t}{\tau_2})$). **Figure 5.12(a)** and **(b)** show the the sum of the prefactors ($A = A_1 + A_2$) for the absorbers and the effective lifetime τ_{eff} calculated as $\tau_{\text{eff}} = \frac{A_1\tau_1 + A_2\tau_2}{A_1 + A_2}$. As shown in **Figure 5.11**, no fast initial decay is observed at early times, such that the sum of prefactors displayed in **Figure 5.12(b)** can be assumed proportional to the doping concentration in the absorbers. Above 353 °C, A for ACIGS absorbers is slightly lower than for CIGS, which is consistent with the reduced carrier concentration in ACIGS reported by other groups [55, 103]. However, CIGS experiences a significant drop in A below 353 °C, even lower than the values of ACIGS. In contrast, A drops for ACIGS only with T_{sub} values below 303 °C. We also performed C-V measurements (**Figure 5.13**) to estimate the apparent doping concentration, as shown in **Figure 5.14**. Similar drops in doping density around 300 °C - 350 °C were observed for both CIGS and ACIGS.

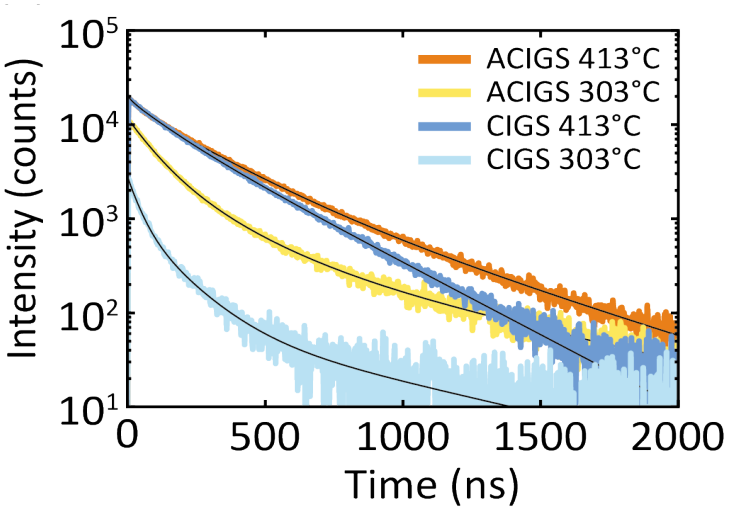

Figure 5.11: TRPL decays for (A)CIGS layers grown at 413 °C and 303 °C.

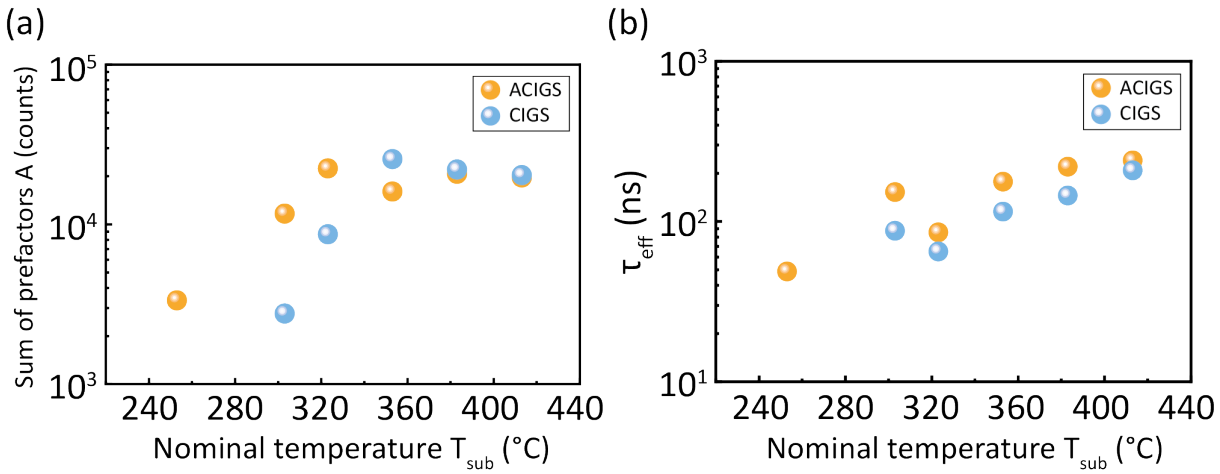

Figure 5.12: (a) Sum of prefactors $A_1 + A_2$ (A) of TRPL decays as a function of nominal T_{sub}. (b) τ_{eff} of TRPL decays as a function of nominal T_{sub}.

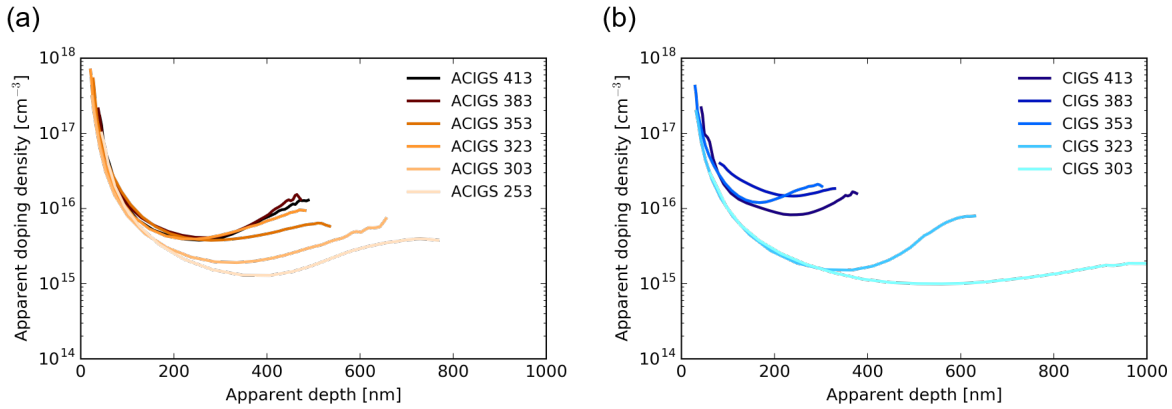

Figure 5.13: Apparent doping density as a function of depth in (a) ACIGS and (b) CIGS absorbers

In **Figure 5.12(b)**, it is shown that τ_{eff} values of ACIGS layers are slightly higher than those of CIGS for all T_{sub}, which we attribute to the improved morphology, reduced grain boundaries, and to the lesser density of structural and electronic defects discussed above.

Following detailed balance principle, the V_{OC} of (A)CIGS solar cells can be related to the external light emitting diode quantum efficiency (EQE_{LED}), as describe by **Equation 3.4**, where V_{OC}^{rad} is the V_{OC} in the radiative limit and $-\frac{kT}{q} ln(EQE_{\text{LED}})$ is associated to the non-radiative voltage losses. Ideally, the TRPL parameters τ_{eff} and A can be connected to EQE_{LED}. Hence, it is possible to calculate the relative difference in V_{OC} losses (ΔV_{OC}) for different samples by their ratio of EQE_{LED}, approached by their ratio of $A_1\ \tau_1 + A_2$

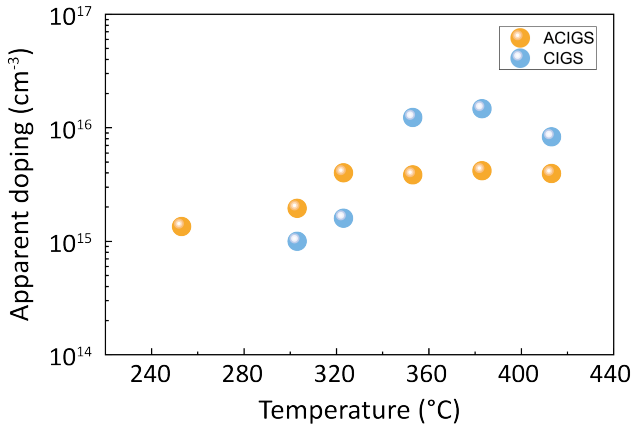

Figure 5.14: Apparent doping estimated from C-V measurements as a function of T_{sub}.

τ_2 (**Equation 3.5**). The ACIGS absorber grown at 253 °C was chosen as the reference providing a ΔV_{OC} of 0 mV. **Figure 5.15** compares the calculated ΔV_{OC} with the device $V_{\mathrm{OC,def}}$. The data closely follow the dashed line with slope of unity representing the expected behavior.

We conclude that TRPL data is a good predictor of the device $V_{\mathrm{OC,def}}$. At higher T_{sub}, the high V_{OC} of ACIGS layers stems from longer τ_{eff} values. In contrast, low doping reduces the V_{OC} of (A)CIGS solar cells grown at low T_{sub}. Ag extends the threshold T_{sub} at which doping starts to drop significantly, widening the T_{sub} process window for ACIGS by about 50 °C.

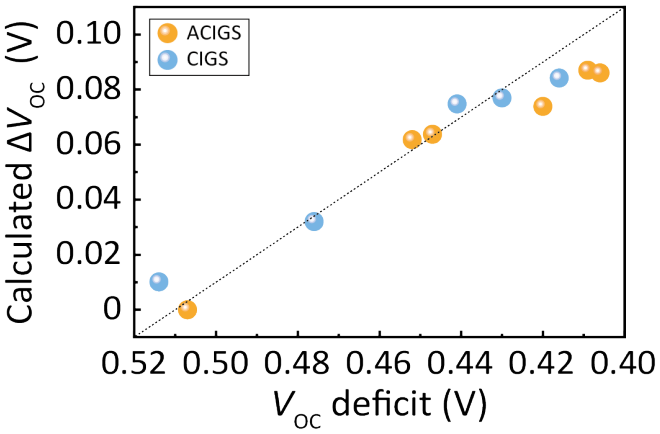

Figure 5.15: Relationship between calculated ΔV_{OC} and the device $V_{\mathrm{OC,def}}$.

5.7 Residual Stress analysis

The XRD residual stress analysis was performed on the ACIGS and CIGS absorbers grown at different T_{sub}. The analysis was carried out on the (112) reflection measured with different ψ angles, defined as the angle between the scattering vector and the sample's normal direction. The residual stress in the films is calculated from the magnitude and direction of the peak shifts. **Figure 5.16** summarizes the residual stress in absorbers grown at different T_{sub}. Both ACIGS and CIGS absorbers have compressive stress rather than tensile stress with three-stage process, in agreement with what was reported before for CIGS absorbers [39, 110]. Ag alloying significantly reduces the compressive stress (by about 50% for most of T_{sub} sample pairs). **Figure 5.17** illustrate how the (112) peak of ACIGS and CIGS absorbers grown at 413 °C, 323 °C and 303 °C shift as a function of the ψ angles. Peaks of both ACIGS and CIGS samples shift to the right with increasing ψ (compressive stress), but the shift is smaller for ACIGS than for CIGS. This makes ACIGS even more promising for a variety of flexible PV applications, for which adhesion issues are critical. It is worth mentioning that the residual stress shown in **Figure 5.16** could be slightly underestimated because of the GGI gradings. The X-ray penetration depth is shallower at larger ψ angles. Thus, the diffraction angle of the (112) reflection may slightly shift towards lower values as a result of the increased sensitivity to the front region with larger lattice constant and smaller GGI. Nevertheless, a qualitative comparison of the residual stress between CIGS and ACIGS grown at the same T_{sub} is still valid because CIGS and ACIGS have quite similar GGI gradings, as shown in **Figure 5.6(a)**, and are therefore similarly affected.

There are two possible explanations for reduced compressive stress in ACIGS absorbers: the compressive stress is thought to be introduced due to the lattice expansion (from Cu-poor to Cu-rich) during increasing Cu concentration in the three-stage process [39]. In the case of adding Ag with precursor layer method, the presence of Ag before adding Cu can be responsible for the reduced compressive stress, i.e. less lattice expansion from Cu-poor to Cu-rich. The other hypothesis is that Ag helps to release the compressive stress due to enhanced elemental diffusion and grain growth, especially during recrystallization.

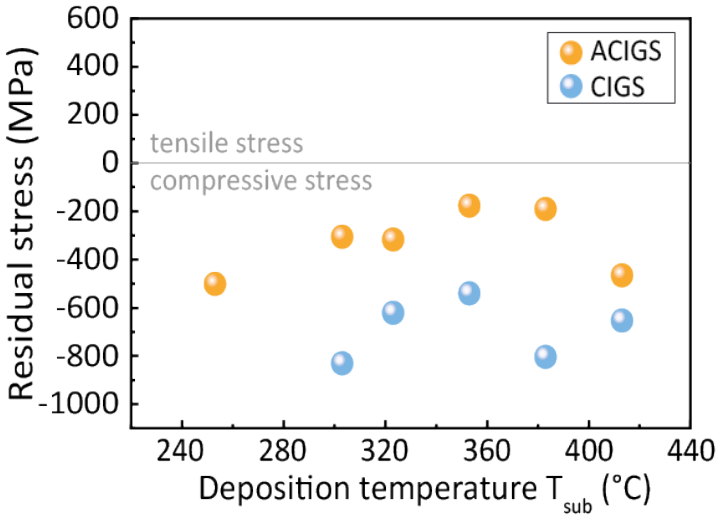

Figure 5.16: Residual stress as a function of nominal T_{sub}.

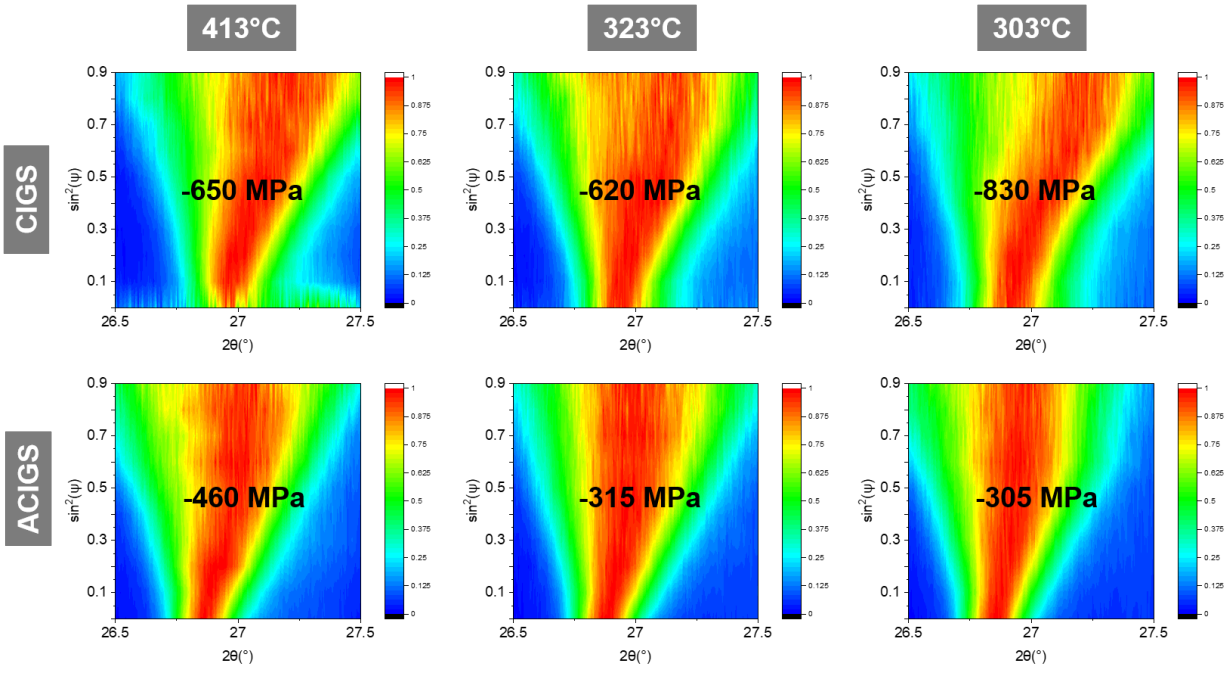

Figure 5.17: (112) peak shift with various ψ angles for ACIGS grown at nominal T_{sub} of 413 °C, 323 °C and 303 °C.

5.8 Conclusion

We successfully fabricated solar cells with (A)CIGS absorbers grown at very low T_{sub} from 413 °C down to 253 °C. ACIGS displayed a number of advantageous characteristics over CIGS summarized below: ACIGS devices outperformed CIGS ones, and high efficiencies were maintained over a wider temperature range: efficiencies of 19.6 % and 18.5 % for T_{sub} of 353 °C and 303 °C. J_{SC} remains essentially constant, while FF plays a role. The loss of efficiency at low T_{sub} is mostly driven by V_{OC} degradation. ACIGS maintains high V_{OC} with substantially lower T_{sub} than that of CIGS due to improved absorber morphology and less deterioration seen in low-temperature grown CIGS. The presence of Ag also reduces the density of structural and electronic defects as evidenced by Urbach energy. Furthermore, TRPL results detailed the causes for changes in $V_{\mathrm{OC,def}}$ and discriminated two T_{sub} regimes: for CIGS, with T_{sub} above 350 °C the moderate $V_{\mathrm{OC,def}}$ degradation is driven by non-radiative recombination reflected by τ_{eff}. For T_{sub} below 350 °C, the strong performance degradation is mainly driven by the decrease in doping density. The threshold between two regimes is lower by 50 °C in presence of Ag. Last, ACIGS absorbers present less residual stress than CIGS ones, which is advantageous in view of flexible applications. Our results suggest several benefits of Ag alloying in industrial production environment. The widened parameter window for T_{sub} relaxes manufacturing constraints, and may contribute to reducing the manufacturing costs.

5.9 Sample references

CIGS	413 °C	383 °C	353 °C	323 °C	303 °C
Sample	TL3154	TL3162	TL3163	TL3168	TL3171

Table 5.1: Internal sample naming for CIGS solar cells Chapter 5

ACIGS	413 °C	383 °C	353 °C	323 °C	303 °C	253 °C
Sample	TL3155	TL3161	TL3160	TL3169	TL3172	TL3173

Table 5.2: Internal sample naming for ACIGS solar cells Chapter 5

6 Bifacial CIGS solar cells

This chapter is adapted from the publication:

Yang, S. C., Lin, T. Y., Ochoa, M., Lai, H., Kothandaraman, R., Fu, F., Tiwari, A. N., and Carron, R. (2022). *Efficiency boost of bifacial Cu(In,Ga)Se_2 thin-film solar cells for flexible and tandem applications with silver-assisted low-temperature process*, Nature Energy, 1-12 [111].

My own contribution to this publication consisted in: design of the experiments, deposition of CIGS thin films, completion of working solar cells, measurement and analysis of: SIMS, XRF, J-V, EQE, TRPL, and data interpretation. Tzu-Ying Lin carried out the STEM and TEM measurements. Mario Ochoa and Romain Carron performed the optical and numerical simulations. Huagui Lai fabricated perovskite top cells and assisted with the bifacial and tandem solar cell measurements. Radha Kothandaraman performed the laser scribing on PI samples. Fan Fu supervised the work on perovskite solar cells.

6.1 Introduction

In **Chapter 4** and **Chapter 5**, we have shown that silver-alloyed CIGS absorbers have better material properties as compared to CIGS absorbers. By adding a small amount of Ag, high-quality absorbers can be obtained with a low-temperature process down to 300°C. Such low-temperature deposition opens the possibility of suppressing the formation

of GaO_x while simultaneously building up strong Ga gradients. In this chapter, we take advantage of the silver-promoted low-temperature process to completely remove GaO_x formation at the CIGS/ITO interface while keeping high absorber quality, steep Ga back bandgap gradient and good optical and electrical properties of ITO. Furthermore, we present different proof-of-concept bifacial devices including flexible bifacial devices and bifacial perovskite/CIGS tandem devices in four-terminal configuration, paving the way for future developments of the next generation of bifacial thin-film tandem devices.

6.2 Reduction of CIGS deposition temperature on ITO

Our approach involves deposition of a 15 nm-thin Ag precursor layer on commercial soda-lime glass substrates covered with a SiO_x alkali diffusion barrier and 200 nm indium tin oxide (ITO) layer. A modified multi-stage coevaporation process developed in **Chapter 3** was used in order to maximize the GGI near the back interface of the 2 µm thick absorber. The amount of Ag in the absorbers corresponds to about 4-5% AAC ratio. NaF and RbF post-deposition treatment were applied in-situ. The device structure of bifacial CIGS solar cells and its SEM cross-sectional image are shown in **Fig. 6.1**. To investigate the GaO_x interlayer formation at different substrate temperature, CIGS deposition were performed at four different T_{sub} from 453°C to 303°C, with corresponding sample names T453, T413, T353 and T303. The GGI depth profiles obtained from SIMS for those absorbers are shown in **Fig. 6.2**. The back grading heights ΔGGI are defined as the difference between the maximum GGI at the back and the minimum GGI at the notch (for example: indicated with the red dashed line in T453). Higher T_{sub} enhances elemental inter-diffusion, and significantly reduces Ga back gradient, especially for T453, with a ΔGGI of only 0.3. On the contrary, both T303 and T353 have ΔGGIs of around 0.55 to 0.6.

The CIGS/ITO interface was carefully investigated by STEM (scanning transmission electron microscopy) and EDS (energy-dispersive X-ray spectroscopy) to find the presence of the GaO_x interlayer in the different samples. **Fig. 6.3** shows EDS mappings of Ga and O signals for samples T453, T413, and T353. High Ga signal at the interface was

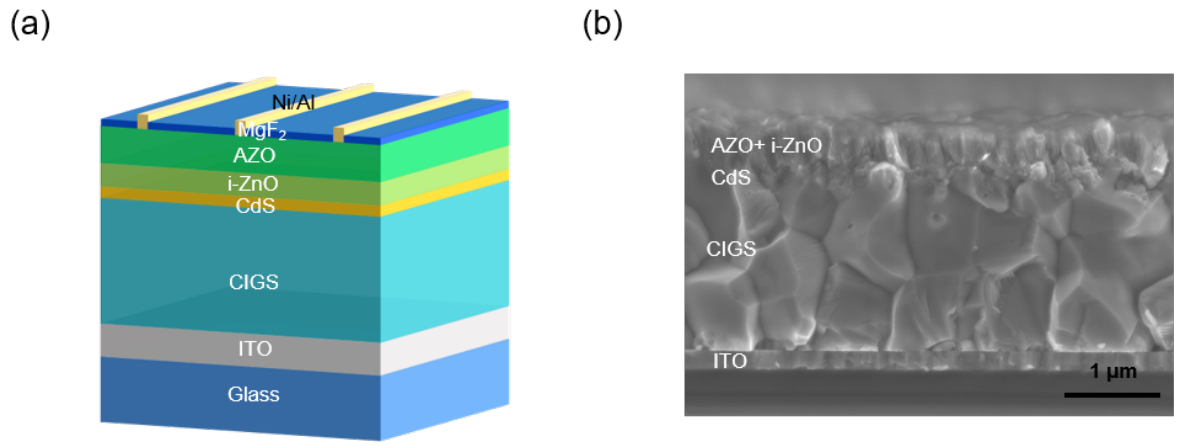

Figure 6.1: (a) Device structure of the bifacial CIGS solar cells on ITO coated glass substrates. (b) SEM cross-sectional image of the device with the absorber fabricated at 353°C

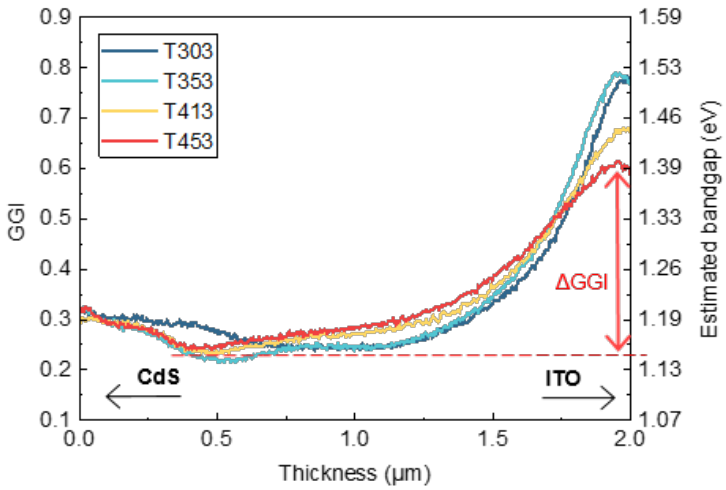

Figure 6.2: GGI and bandgap depth profiles of absorbers grown at different temperatures.

detected in T453 and T413, but not in T353. EDS line scans of Ga and O across the interfaces are provided in **Fig. 6.4**. A 2-5 nm-thick GaO_x interlayer is present at the CIGS/ITO interface of T453, confirmed by the Ga accumulation and the early O signal increase. For T413, a very thin GaO_x interlayer (1-2 nm) is still present. In contrast, no interlayer could be evidenced in T353, convincingly suggesting the low temperature CIGS

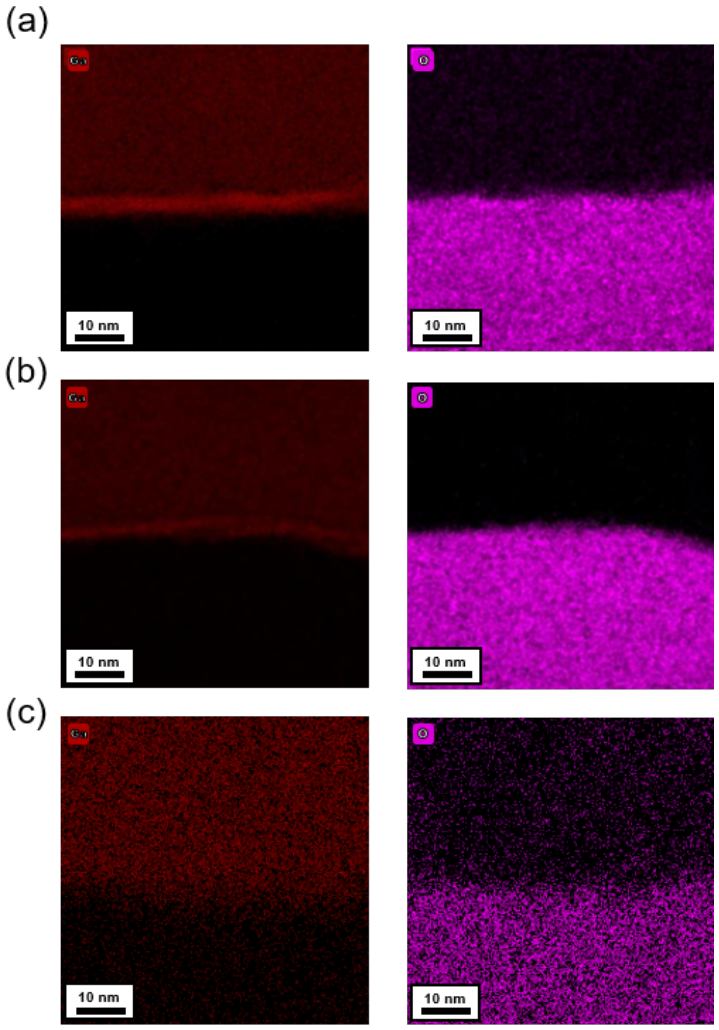

Figure 6.3: STEM EDS mapping of Ga and O for (a) T453, (b) T413, and (c) T353.

deposition is effective to reduce/avoid the formation of GaO_x interlayer.

Fig. 6.5a and **Fig. 6.5b** show bright-field (BF) and high-angle annular dark-field (HAADF) STEM images for samples T453 and T353. High resolution BF images and the fast Fourier transform (FFT) of the evidenced areas (red square region) near the interface are also provided. In T453, an amorphous interlayer is evidenced with a thickness of around 2 nm. Instead, high resolution STEM image of T353 reveals a sharp interface between ITO and CIGS. Crystalline phases with specific orientations are present on the two sides of the interface. The corresponding FFT around the interface also supports this observation. Other STEM images for T303 are also provided in **Fig. 6.6**. Therefore, we

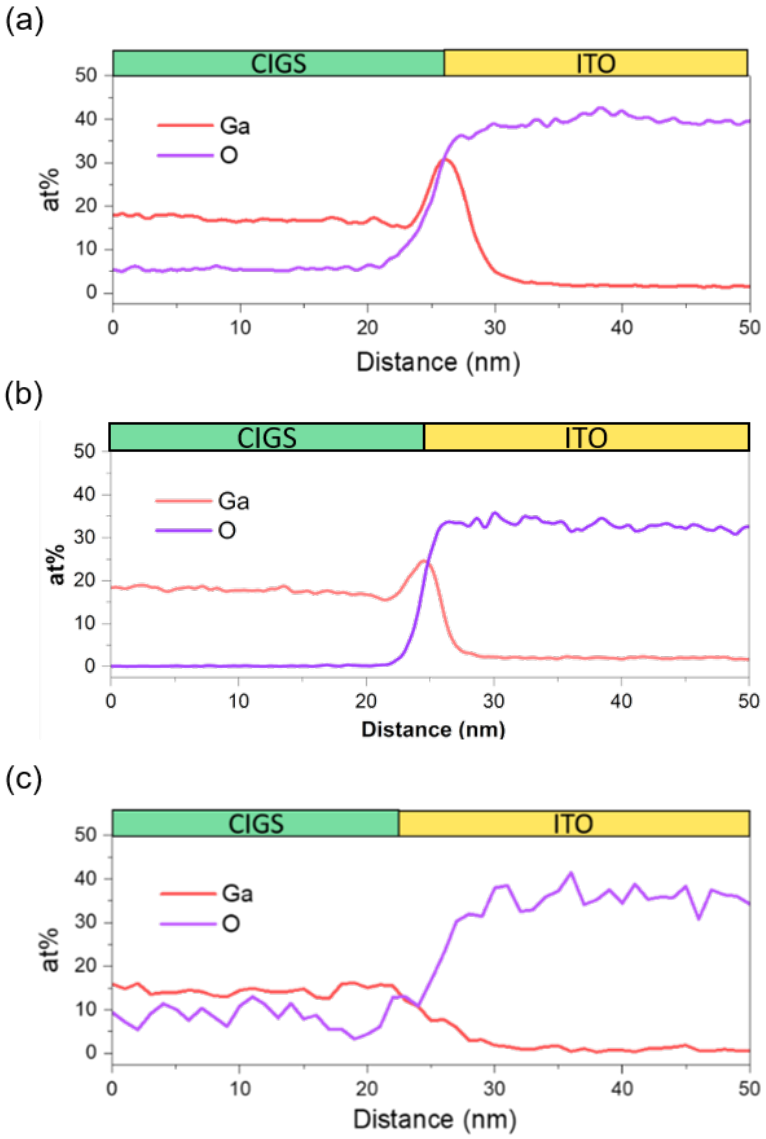

Figure 6.4: STEM EDS linescans of Ga and O across CIGS/ITO interface for (a) T453, (b) T413, and (c) T353.

conclude that low T_{sub} effectively suppresses the GaO_x formation despite very high GGI (about 0.8, as shown in **Fig. 6.2**) near the back interface. It enables building up a stronger effective electric field with pronounced Ga gradients while avoiding formation of undesired GaO_x. In addition, the SiO_x barrier layer used in those samples might also play a role in reducing GaO_x since the presence of Na during absorber growth can promote the GaO_x formation [112].

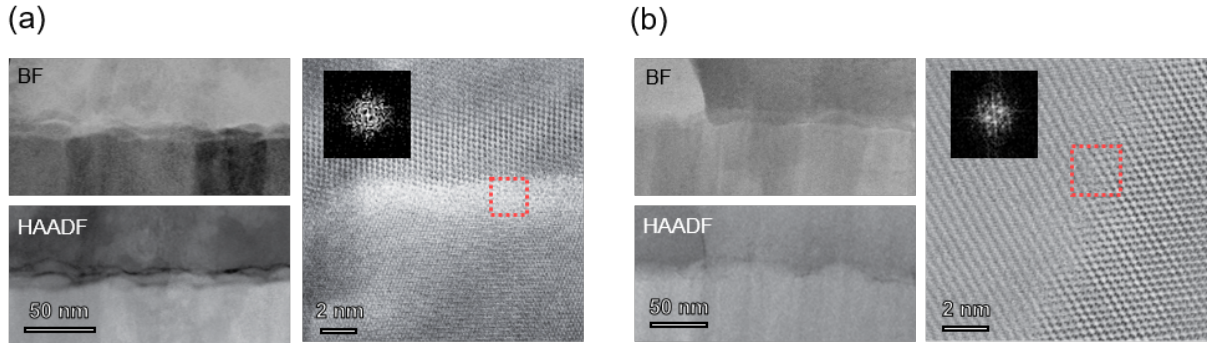

Figure 6.5: (a) Bright-field and dark-field STEM images near the CIGS/ITO interface of T453, and (b) of T353, together with high resolution images of the interface region including FFT of the evidenced interface area

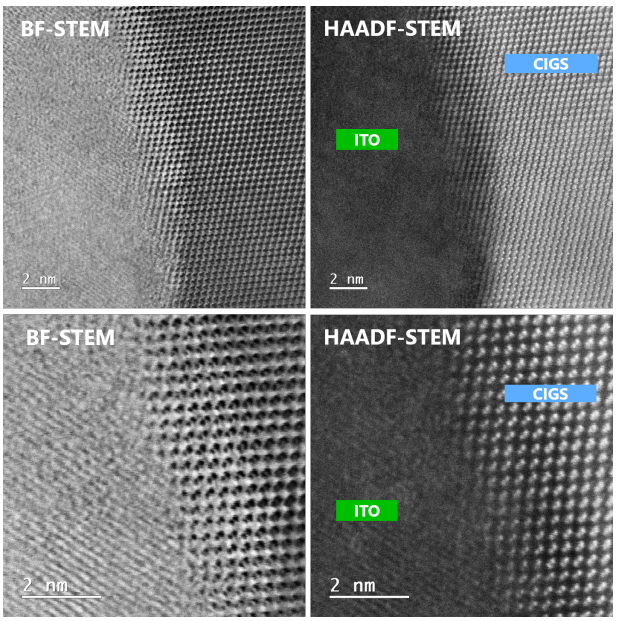

Figure 6.6: Bright-field and high-angle annular dark-field STEM image near the CIGS/ITO interface of sample T303.

Due to the absence of GaO_x interlayer in T353, we observe not only local expitaxy of CIGS on ITO back contacts but also "misfit dislocations" on CIGS side to accommodate the lattice mismatch between ITO and CIGS, as shown in **Fig. 6.7**. The red marks in **Fig. 6.7c** indicated where the misfit dislocations are. During the growth of CIGS absorbers, dislocations form to reduce the total energy as the strain energy increases with increased absorber thickness. By considering the mismatch of (211) interplanar spacing (d-spacing) in ITO layer (about 0.41 nm) and (112) d-spacing in CIGS (about 0.33 nm),

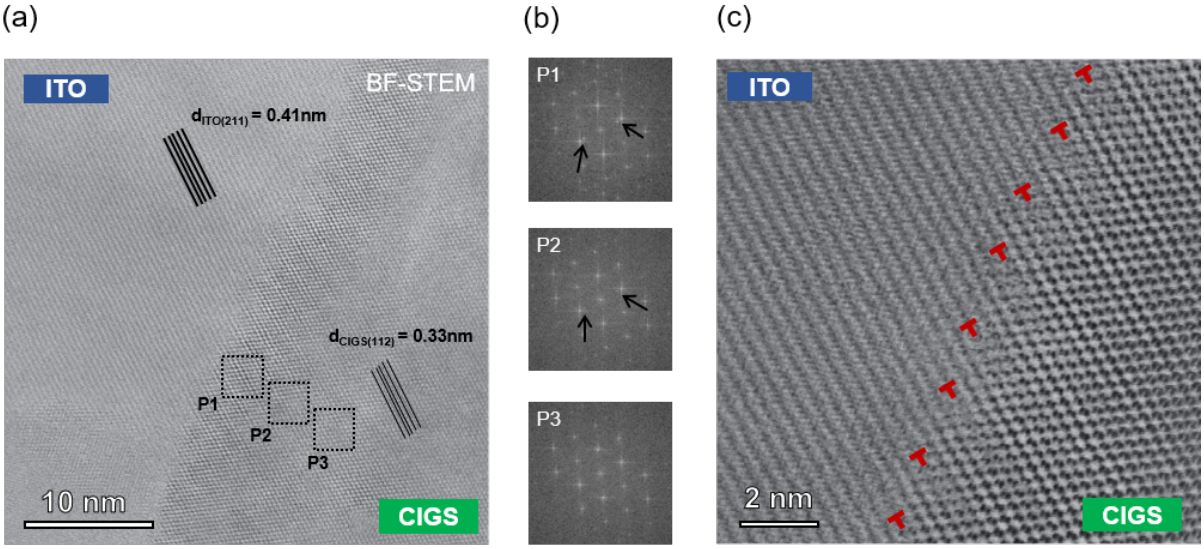

Figure 6.7: (a) Bright-field STEM image near the CIGS/ITO interface of sample T353. The crystal orientation of both ITO and CIGS layers are labeled. (b) FFT of areas P1, P2 and P3 showing additional diffraction points disappearing at some distance from the interface. (c) Misfit dislocations with alternating distances ($5\times d_{112}$ and $4\times d_{112}$) evidenced in the CIGS, near the ITO/CIGS interface.

the observed alternating distances between misfit dislocations (5 and 4 atomic spacings) near the interface are well explained by **Eq. 6.1**. One period ($9\times d_{112}$) on CIGS side is equivalent to $7\times d_{211}$ in ITO. These observation hints at the possibility of epitaxial CIGS deposition on ITO substrates with GaO_x free interface, for example to trigger formation of CIGS layers with large grains.

$$d_{\text{ITO }(211)} \times 7 = 2.87nm \approx 2.97nm = d_{\text{CIGS }(112)} \times 9 \tag{6.1}$$

6.3 Device efficiency under front illumination

CIGS solar cells with Mo back contact usually yield higher PCE owing to better material quality with increased T_{sub} [109, 113]. However, for our CIGS solar cells on ITO back contact, we identified an optimal T_{sub} for highest PV performance. **Fig. 6.8a** shows the the J-V curves under front illumination for samples T303, T353, T413 and T453. Sample T353 yields the best PCE of 17.7% without noticeable current blocking, while a mild blocking behavior starts to appear in T453. With higher T_{sub}, FF limits the device

efficiency due to higher apparent series resistance (R_s). We attribute the difference to the formation of the highly resistive GaO_x interlayer. Owing to their band alignment, the p-CIGS/n^+-ITO interface is supposed to form a Schottky, reverse diode contact. In absence of GaO_x interlayer like in T353, it was postulated that easy charge transport can occur through the Schottky barrier by trap-assisted tunneling of holes mediated by Na-induced defects near the interface, as illustrated in **Fig. 6.9** [74, 76, 114]. In turn, GaO_x is assumed to be a highly resistive n^+ material with a large valence band edge offset to CIGS. Therefore the existence of a GaO_x interlayer should considerably increase the height of the hole barrier and hinder the charge transport. This explains why the presence of GaO_x at interface can play a crucial role in FF and device performance under front illumination. However, it is worth noting that good FF might still be achieved [77] by changing the properties of GaO_x or different supply of Na. Also, the coverage and thickness uniformity of GaO_x can also play a role. While the above mentioned factors strongly depends on different group's equipment, process and so on and are more difficult to control and reproduce in different research groups, we believe our strategy of complete removal of GaO_x is more robust.

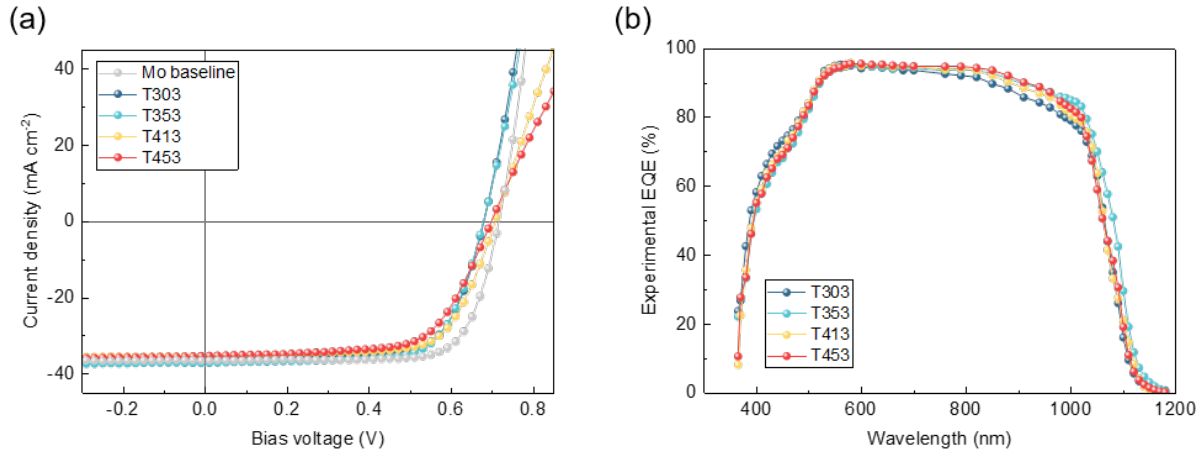

Figure 6.8: (a) J-V curves for bifacial CIGS solar cells grown at different T_{sub} under one sun front illumination. (b) Corresponding EQE curves.

On the other hand, reduced T_{sub} of T303 degrades the absorber quality and increases V_{OC} deficit, despite a slightly higher FF, as shown in **Table 6.1**. We further performed

EQE measurements as shown in **Fig. 6.8b**. The samples show quite similar response, except for slightly reduced EQE response at long wavelengths for sample T303. This decrease is tentatively attributed to the degraded absorber quality and worse collection of charge carriers. Due to the trade-off between absorber quality for high V_{OC} and the formation of GaO_x limiting FF, sample T353 yields the best PCE under front illumination.

Solar Cells	V_{OC} (V)	J_{SC} (mA/cm^2)	FF (%)	PCE (%)	V_{OC} deficit (V)
T303	0.679	35.8	71.5	17.4	0.459
T353	0.678	37.0	70.0	17.7	0.442
T413	0.707	35.2	69.4	17.3	0.425
T453	0.698	35.2	65.4	16.1	0.431

Table 6.1: J-V parameters of the best cell in T303, T353, T413 and T453 under front illumination.

Solar Cells	T303	T353	T413	T453
Before CIGS deposition	10 Ω/sq			
After CIGS deposition	9.1 Ω/sq	8.7 Ω/sq	8.9 Ω/sq	9.0 Ω/sq

Table 6.2: Sheet resistance of ITO before and after CIGS depositions.

To bridge the PCE gap with Mo-based devices, we further optimized the amount of RbF PDT and CGI composition ratio. It is well-known that such optimizations are important for V_{OC} and device performance [85] improvement. **Fig. 6.10** shows samples with higher CGI and optimized RbF with the lowest V_{OC} deficit achieved (about 410 mV). Finally, we improved the cell electrical connection to compensate for the high sheet resistance of the 200 nm-thick ITO (about 10 ohms per square) by applying a conductive paste directly around the cell area. The best cell yields 19.7% under front illumination, very similar to baseline process for cells using Mo contact. Hence, we demonstrate solar cells with ITO back contact with almost no additional loss as compared to their Mo counterpart.

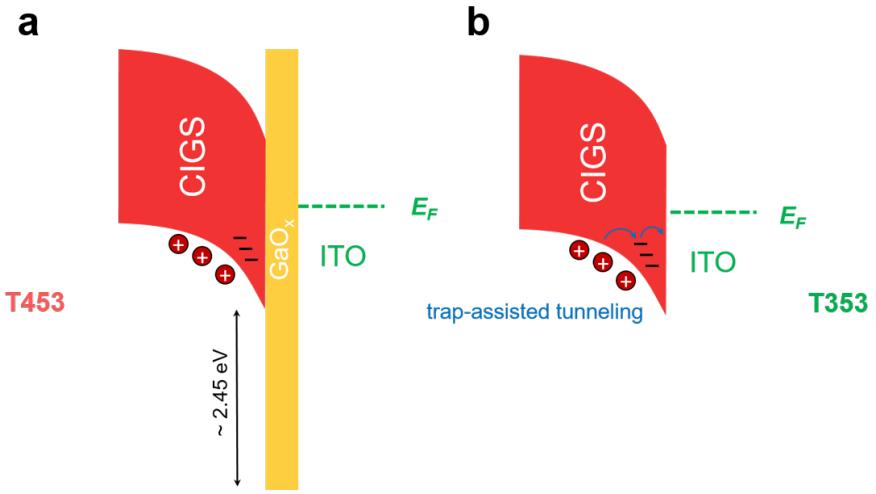

Figure 6.9: The illustration of the possible band diagram for CIGS/ITO interface in (a) T453 with GaO_x interlayer formation and (b)T353 without GaO_x interlayer formation.

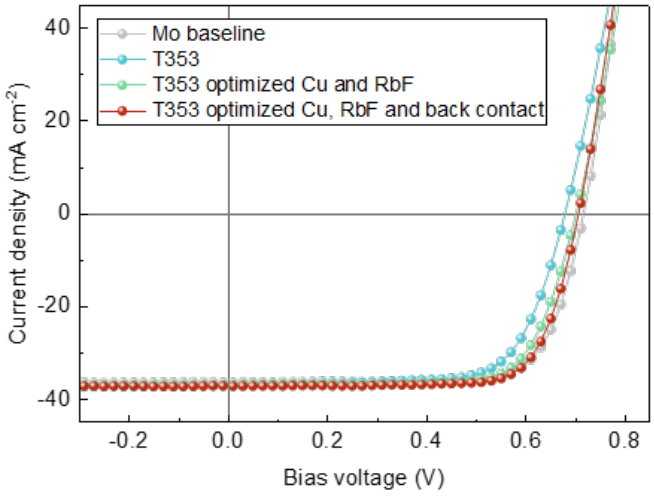

Figure 6.10: J-V curves of bifacial cells grown at 353°C under one sun front illumination, after optimization of deposition and cell processing

To visualize the importance of Rs, we plot in **Fig. 6.11** the PCE versus FF of individual cells of different samples, with the size of bubbles representing Rs values. The Rs values increases consistently with deposition temperature. It is clear that PCE is mainly driven by FF, and that Rs is the key limiting factor to high FF. To exclude that higher Rs might originate from degradation of ITO during CIGS deposition, we measured the sheet resistance (R_{sheet}) of ITO before and after CIGS deposition, by mechanically removing of

all layers above ITO in finished devices (see **Fig. 6.2**). R_{sheet} of ITO is almost unchanged upon absorber deposition for all investigated T_{sub}, although its optical properties are degraded as described below.

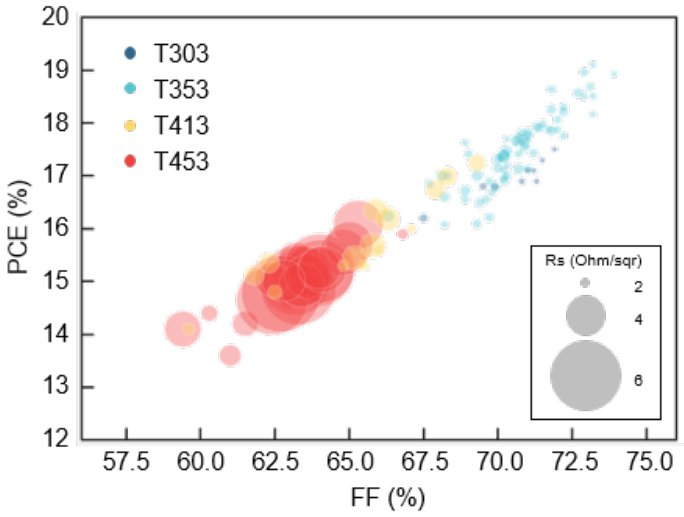

Figure 6.11: R_s bubble chart with respect to PCE and FF. All the samples fabricated in this study are included.

6.4 Device efficiency under rear illumination

Fig. 6.12a shows the J-V curves of bifacial CIGS solar cells under 1-sun rear illumination. Same as front illumination, sample T353 yields the highest PCE, mainly due to higher J_{SC}. The other PV parameters are in reasonable agreement with measurements from the front side (see **Table 6.3**). EQE measurements under rear illumination are provided in **Fig. 6.12b**. The low EQE response at short wavelengths is mainly due to back interface recombination and short photon penetration depth [115]. Below we investigate the EQE response at long wavelengths to distinguish different loss mechanisms. We measured the cell back reflectance R_{back} (**Fig. 6.13**, little differences), and the absorptance of ITO/SLG A_{ITO} after mechanical removal of absorber and front window layers (**Fig. 6.14a**). Then, we calculated the internal quantum efficiency (IQE) as EQE/[(1-R_{back})(1-A_{ITO})] shown in **Fig. 6.14b**. Despite similar and unchanged ITO R_{sheet} values after CIGS deposition, the ITO optical parasitic absorption increases with higher T_{sub}. The root-cause is not clear

yet, however it can be speculated that the amount of oxygen vacancies in ITO may change during the high temperature CIGS deposition [116, 117] in Se ambient.

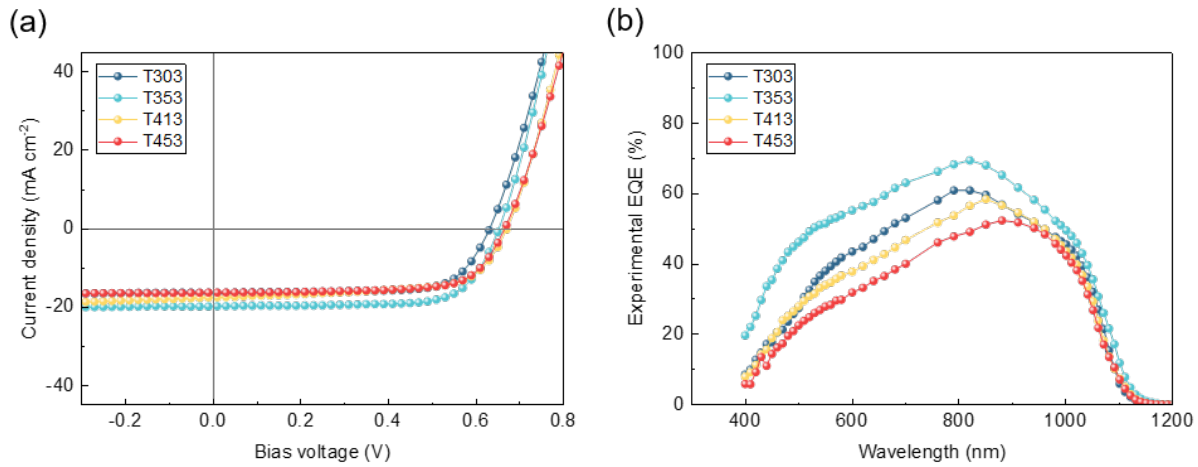

Figure 6.12: (a) J-V curves for bifacial CIGS solar cells grown at different T_{sub} under one sun rear illumination. (b) Corresponding EQE curves.

Solar Cells	V_{oc} (V)	J_{sc} (mA/cm^2)	FF (%)	PCE (%)	V_{oc} deficit (V)
T303	0.632	16.4	72.4	7.4	0.506
T353	0.653	19.9	71.8	9.3	0.467
T413	0.671	17.6	65	7.7	0.461
T453	0.666	16.4	70.6	7.7	0.463

Table 6.3: J-V parameters of the best cell in T303, T353, T413 and T453 under rear illumination.

In long wavelength range ($>$ 950 nm), IQEs are similar except for sample T303, as shown in **Fig. 6.14b**. The lower IQE of T303 is explained by inferior absorber quality and is in line with the degraded long-wavelength EQE under front illumination (**Fig. 6.8b**). Below 950 nm, one observes a maximum in the IQE curves, followed by decreased values at shorter wavelengths. The IQE peak wavelength depends on T_{sub}. Through optical transfer-matrix TMM simulations, we show that this behavior arises from recombination at the CIGS/ITO interface and depends on the absorber GGI gradient.

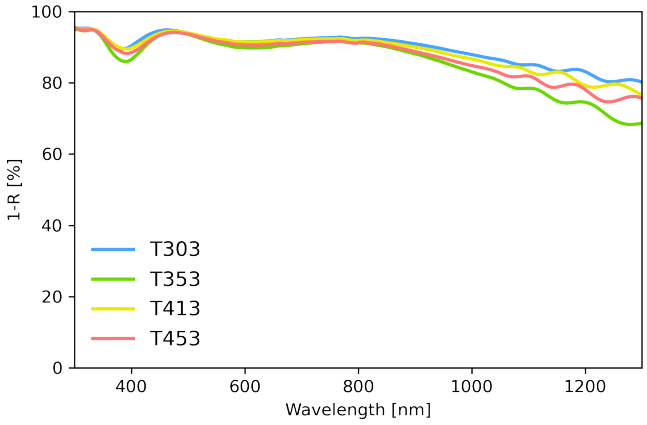

Figure 6.13: 1 - R (reflectance of full cell from back side) for all devices

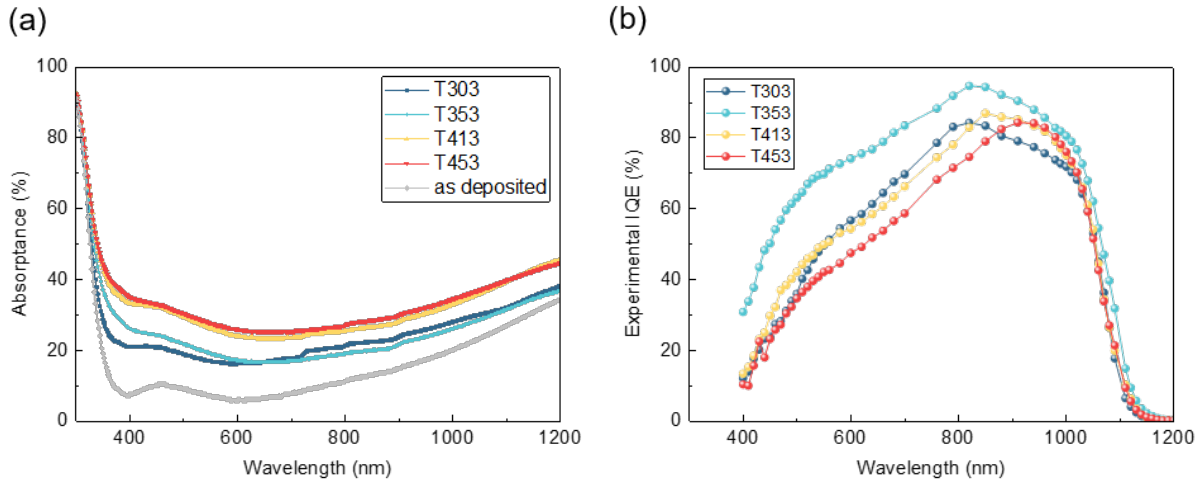

Figure 6.14: (a) Absorptance of the ITO/SLG layers before and after CIGS deposition at different T_{sub}, after removal of CIGS and top layers. (b) IQE curves under rear illumination, accounting for cell reflectance and absorptance of the ITO back contact.

Fig. 6.15a and **Fig. 6.15b** show the absorber gradients of samples T353 and T453, discretized into 20 nm-thick sublayers and colorized (in blue) with the expected optical absorption of a 850 nm illumination from the back, using composition-dependent refractive indices [25]. The illumination direction and its photogenerated electrons/holes in the absorbers are also depicted with the wavy arrows and the yellow/red round symbols. At that specific wavelength, the GGI profile has a strong impact on the initial distribution of photogenerated carriers. For sample T353, photons with wavelength $>$ 850nm are absorbed relatively deep in the absorber due to the locally high GGI and bandgap, and subsequently

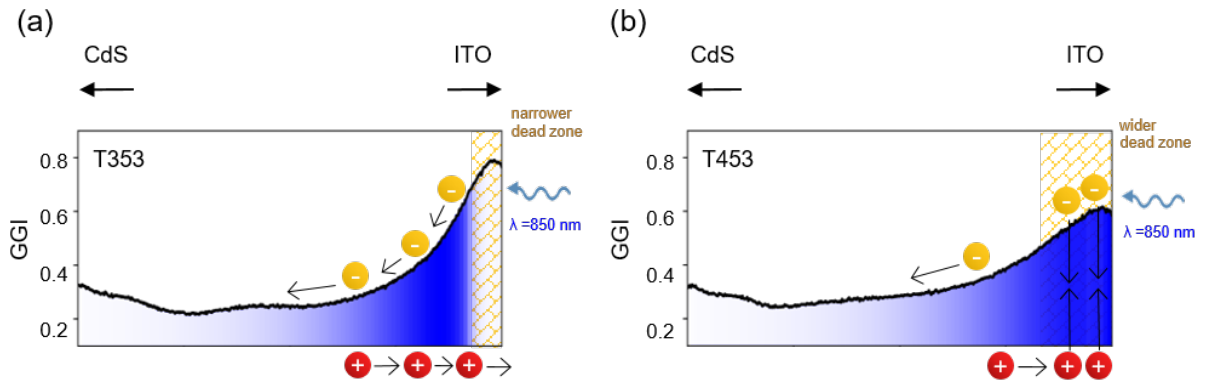

Figure 6.15: Optical TMM simulations of the progressive absorption of an incident rear illumination with a wavelength of 850 nm, as a function of absorber depth. The compositional gradients correspond to samples T353 and T453

mostly avoid carriers recombination at/near the interface (depicted with vertical black arrows). In contrast, high T_{sub} reduces the bandgap near the back interface, resulting in significantly higher absorption near the back interface and more loss of photogenerated carriers for 850nm excitation.

We further calculate the IQEs in **Fig. 6.16** from the optical simulations, defined as the numerically integrated optical absorption in all CIGS sublayers (i.e. assuming collection probability is unity). We introduce a 'dead zone' (illustrated as orange mesh regions in **Fig. 6.15a** and **Fig. 6.15b**) within a certain depth from the back interface, in which photogenerated carriers are considered lost due to fast recombination (collection probability zero) [118]. This very simple model reproduces well the wavelength of the experimental IQE maximum, which is limited on the one side by incomplete absorption, and on the other side by carrier recombination at the back interface. The wavelength of the IQE maximum is primarily determined by the absorber bandgap at the back interface.

Further, we considered two different depths of the dead zone (150 nm and 80 nm). The simulations shown in **Fig. 6.16** also reproduce qualitatively well the shape of the experimental IQE below 800 nm photon wavelength (**Fig. 6.14**). The width of the dead zone can be correlated to the steepness of GGI back gradients. Steeper GGI gradients correspond to stronger effective electric field assisting electrons transport towards the front interface, therefore a narrower dead zone. With a narrower dead zone (steeper gradient),

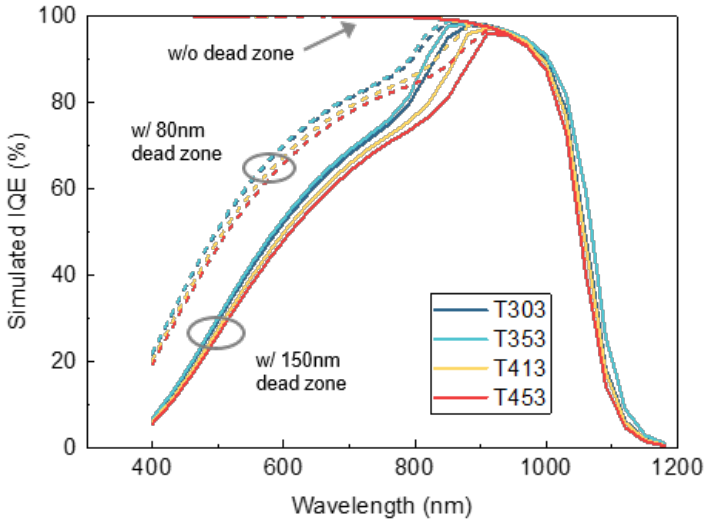

Figure 6.16: Optical TMM simulations of IQE using the experimental gradients of the four CIGS samples, with a dead zone of different width near the rear interface. Carriers photogenerated in this dead zone are considered lost.

the IQE response at short wavelength range is improved thanks to better carrier collection. The collection at shorter wavelength in sample T353 is the best owing to the most favorable GGI gradients. For sample T303, we expect inferior bulk absorber quality that degrades charge transport to the front interface despite a favorable GGI back gradient. Similarly as concluded from front illumination measurements, the absorber of T353 strikes a good balance between pronounced GGI back gradient and material quality.

Fig. 6.17 shows TRPL decays of T353 and T453 in low injection under front the rear illumination with a 635 nm pulsed laser. Measurements were performed after removal of the front TCO layer to prevent the extraction of the charge carriers from the absorbers. In both configurations, T453 shows longer lifetime, in line with its smaller V_{OC} deficit and better bulk quality due to high T_{sub}. Under front excitation, T353 and T453 show similar intensities immediately after laser pulse, evidencing similar $\Delta n \times p_0$ product in the potential minimum (i.e. notch). Under rear excitation, T353 shows higher initial intensity than T453. It can be explained by higher Δn by a factor about 2 in the notch due to less absorption in ITO and suppressed recombination at the back interface in T353, in good agreement with EQE at the 635 nm wavelength.

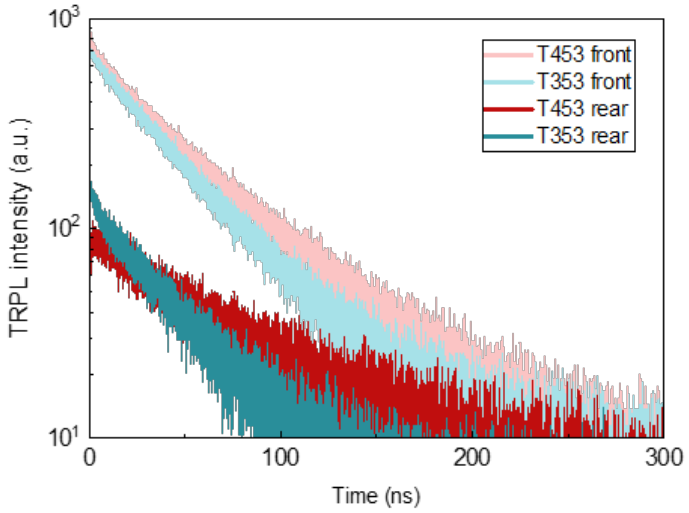

Figure 6.17: TRPL decays for T353 and T453 under front and rear excitation

6.5 Strategies to improve the short-circuit current

The main bottleneck limiting the PCE under rear illumination is the low J_{SC}. Therefore, we investigate and quantify the different current loss mechanisms and discuss strategies to improve J_{SC}. As shown in **Fig. 6.18a** and **Fig. 6.18b**, the highest loss arises from parasitic absorption in the ITO back contact. Less degradation in optical transparency of ITO after CIGS growth in T353 accounts for a maximum current gain of 3.5 mA/cm^2 as compared to T453 (assuming unity collection and no parasitic absorption). Further efforts are needed to tune the ITO deposition process to minimize degradation of optical transparency during CIGS deposition. Replacing ITO with IO:H or IZO could help reducing the optical absorption while maintaining similar R_{sheet} [119]. The advantages of silver promoted low-temperature process should be transferable to other TCOs. The second highest loss of J_{SC} stems from uncollected (recombined) carriers. Mitigating the recombination at the back could be done by a steeper back gradient or by inserting a rear passivation layer [78] which has to be developed. Compared with T453, a current gain of 4.4 mA/cm^2 was obtained with more pronounced back gradient in T353. Last but not least, J_{SC} loss from the back reflection can be reduced by optical management strategies. An anti-reflection

layer on the backside of glass, and interlayers such as a thin Al_2O_3 between ITO and glass may provide further J_{SC} increases.

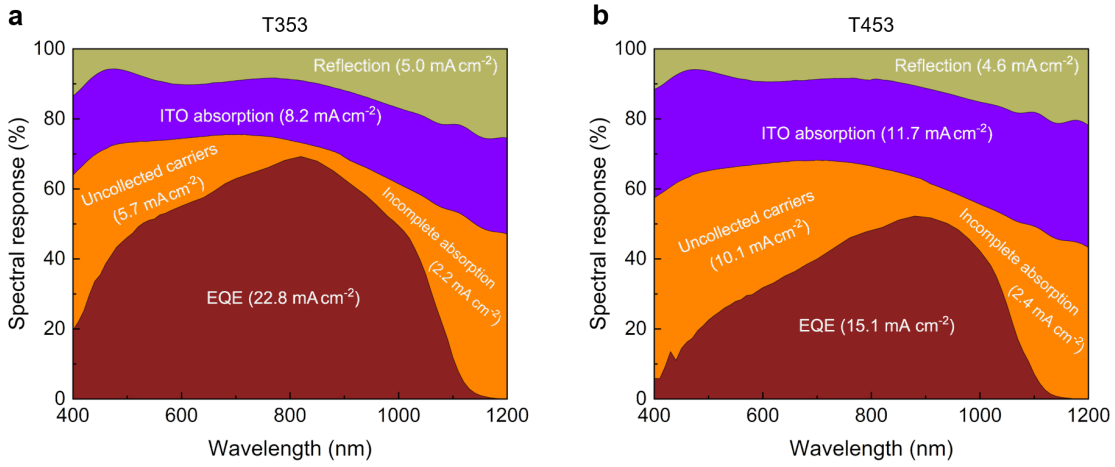

Figure 6.18: (a) Optical and J_{SC} loss analysis for sample T353 under rear illumination. (b) Analysis for sample T453. The loss mechanisms considered are reflection at the back, ITO absorption, uncollected carriers and incomplete optical absorption in CIGS. The J_{SC} losses are calculated in the wavelength range from 365 nm to 1150 nm. The 900 nm wavelength was chosen as the boundary for J_{SC} loss calculation between uncollected carriers and incomplete absorption.

6.6 Champion bifacial device with a significant PCE boost

A bifacial CIGS solar cell was obtained with efficiencies of 19.77% and 10.89% under front and rear one sun illumination, as independently certified by Fraunhofer ISE (see **Fig. 6.19a**). To the best of our knowledge, both values are the highest efficiencies reported for bifacial CIGS devices. For higher PCE under rear illumination, usual strategies used up to now relied on absorber thinning ($\leq 1000\,\mathrm{nm}$) to bring the space-charge region closer to the front interface, which in turn sacrifices the PCE under front illumination (see **Fig. 6.20**). Our results demonstrate an alternative design leading to high performance under both front and back illumination. Under 30% albedo (average albedo considering different ground surfaces), a power generation density of 23.0 $\mathrm{mW/cm^2}$ $\mathrm{BiFi_{300}}$ is foreseen.

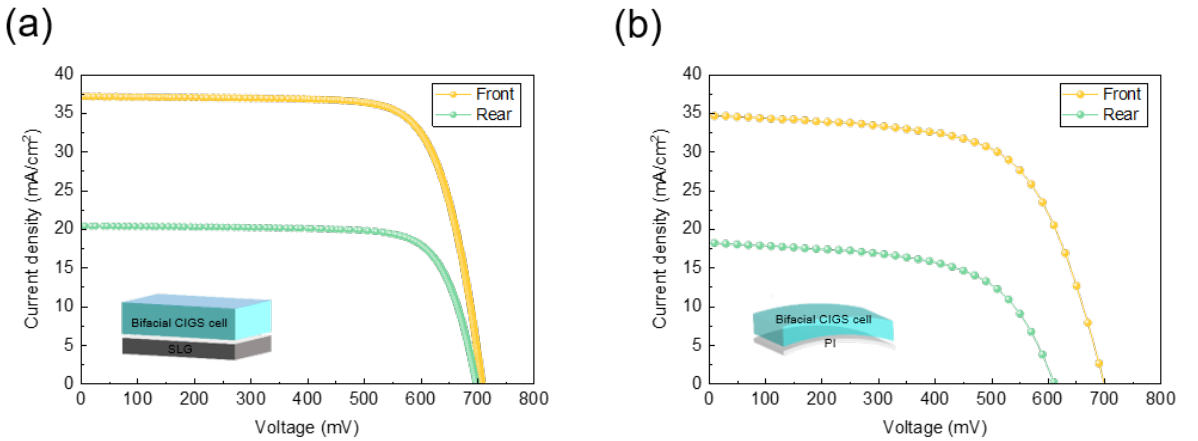

Illumination	V_{OC} (mV)	J_{SC} (mA/cm²)	FF (%)	PCE (%)
Front	707.85	37.13	75.23	19.77
Rear	697.67	20.41	76.46	10.89

Illumination	V_{OC} (mV)	J_{SC} (mA/cm²)	FF (%)	PCE (%)
Front	699.60	34.65	63.34	15.36
Rear	611.35	18.22	59.37	6.61

Figure 6.19: Champion cells and comparison with state-of-the-art. (a) The certification results from Fraunhofer ISE for a bifacial CIGS device on glass. The simplified device architecture on glass substrate is also provided. *Both J_{SC} and PCE under rear illumination are underestimated as an illumination mask area of 0.6247 cm^2 was used during certification while the actual cell area is 0.5629 cm^2. For in-house measurement, a PCE of 12% was reached. (b) J-V curves of a bifacial CIGS device on polyimide under front and rear illumination. The simplified device architecture on polyimide substrate is also provided.

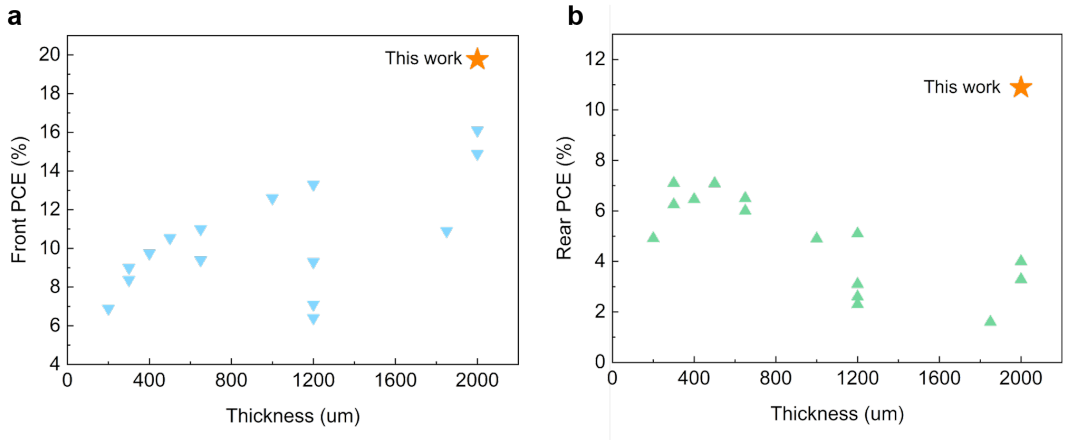

Figure 6.20: Comparison with state-of-the-art (a) Front PCE vs. absorber thickness (b) Rear PCE vs. absorber thickness

6.7 Potential for different bifacial device architectures

Upon the demonstration of high efficiency CIGS bifacial solar cells on a glass substrate, we explore two different device architectures as proof of concepts, namely bifacial CIGS solar cells on flexible substrates and 4-terminal perovskite/CIGS tandem solar cells.

To the best of our knowledge, all reported flexible bifacial CIGS devices rely on a lift-off process [120, 121, 122, 123, 124], which is not considered attractive from an industry perspective, especially for large area and roll-to-roll manufacturing process. Instead, we directly deposited CIGS onto ITO-coated flexible substrates (polyimide). The polyimide foils we used have a yellow-brown appearance with a reasonable near-infrared transparency. J-V curves of the best cell are shown in **Fig. 6.19b**, with PCEs of 15.36% and 6.61% under front and rear illumination, respectively. It is worth mentioning that V_{OC} under front illumination is close to that on SLG substrate, evidencing comparable absorber quality. However, we experienced the shunting issue related to experimental difficulties in cell definition on the polyimide substrate at the early stage of development due to poor adhesion of ITO on PI substrates. We expect this issue to have strong impact on V_{OC} under rear illumination. As compared to SLG substrate, J_{SC} under rear illumination is further degraded by the optical absorption in the polyimide substrate. Besides thinner polyimide foils, more transparent flexible substrates such as colorless polyimide (CPI) may be suitable candidates to improve J_{SC}.

In **Fig. 6.21**, we compare our best results on glass and PI with the-state-of-the-art bifacial solar cells of different PV technologies [63, 73, 74, 115, 120, 121, 122, 123, 124, 125, 126, 127, 128, 129, 130, 131, 132, 133, 134, 135, 136, 137, 138]. In the past, only silicon, perovskite and GaAs could reach simultaneously high bifaciality and high PCE. For high bifaciality, CIGS and CdTe always needed to trade off PCE. With the help of Ag and an optimal T_{sub}, we obtained significant boosts in PCEs for bifacial CIGS solar cells on both glass and PI substrates. Such efficiency boost may open pathways towards the implementation of CIGS bifacial solar cells for unexplored applications up to now.

Recently, bifacial tandem solar cells have drawn a lot of attention due to the best use of

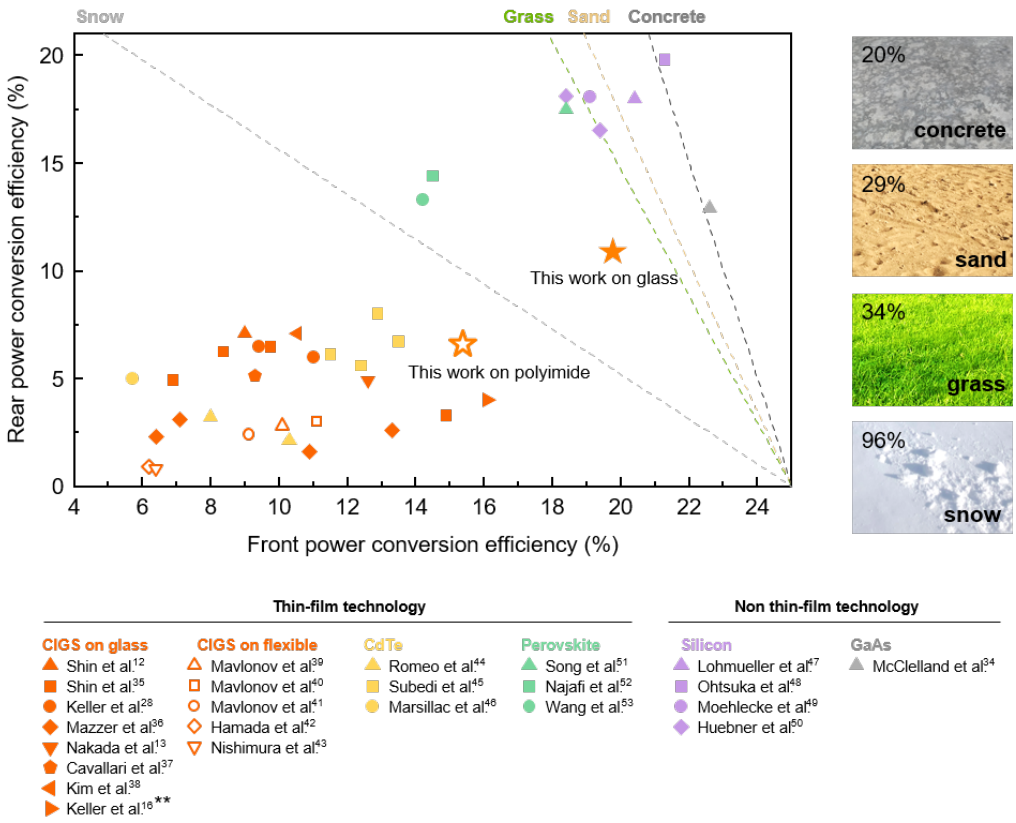

Figure 6.21: Champion cells and comparison with state-of-the-art. Comparison between this work and state-of-the-art bifacial solar cells. The dash lines are corresponding to 25% bifacial efficiency calculated by: front PCE + rear PCE×albedo. The albedo values for different ground conditions are shown in the corresponding figures.

the sunlight and better overall performance [139, 140, 141]. Especially, all-thin-film bifacial tandem solar cells have many advantages like lighter weight and the potential for roll-to-roll process. Despite thin film CIGS is one of the most promising bottom cells with good long-term stability, low bifacial PCE hindered its development. With a bifacial PCE boost presented in this study, we further demonstrate high performance four terminal bifacial perovskite/CIGS tandem solar cells. The J-V curves, EQE curves, and P-V parameters are shown in **Fig. 6.22** and **Table 6.4**. Due to different areas of our perovskite and CIGS cells, the CIGS bottom cells were measured with an optical filter prepared simultaneously with the perovskite top cells, with the same layer sequences and thicknesses. Overall, a power generation density of 28.0 mW/cm^2 $BiFi_{300}$ is obtained, with a power density gain of about 8.9 mW/cm^2 as compared to the performance of the stand-alone CIGS cell the

stand-alone CIGS cell.

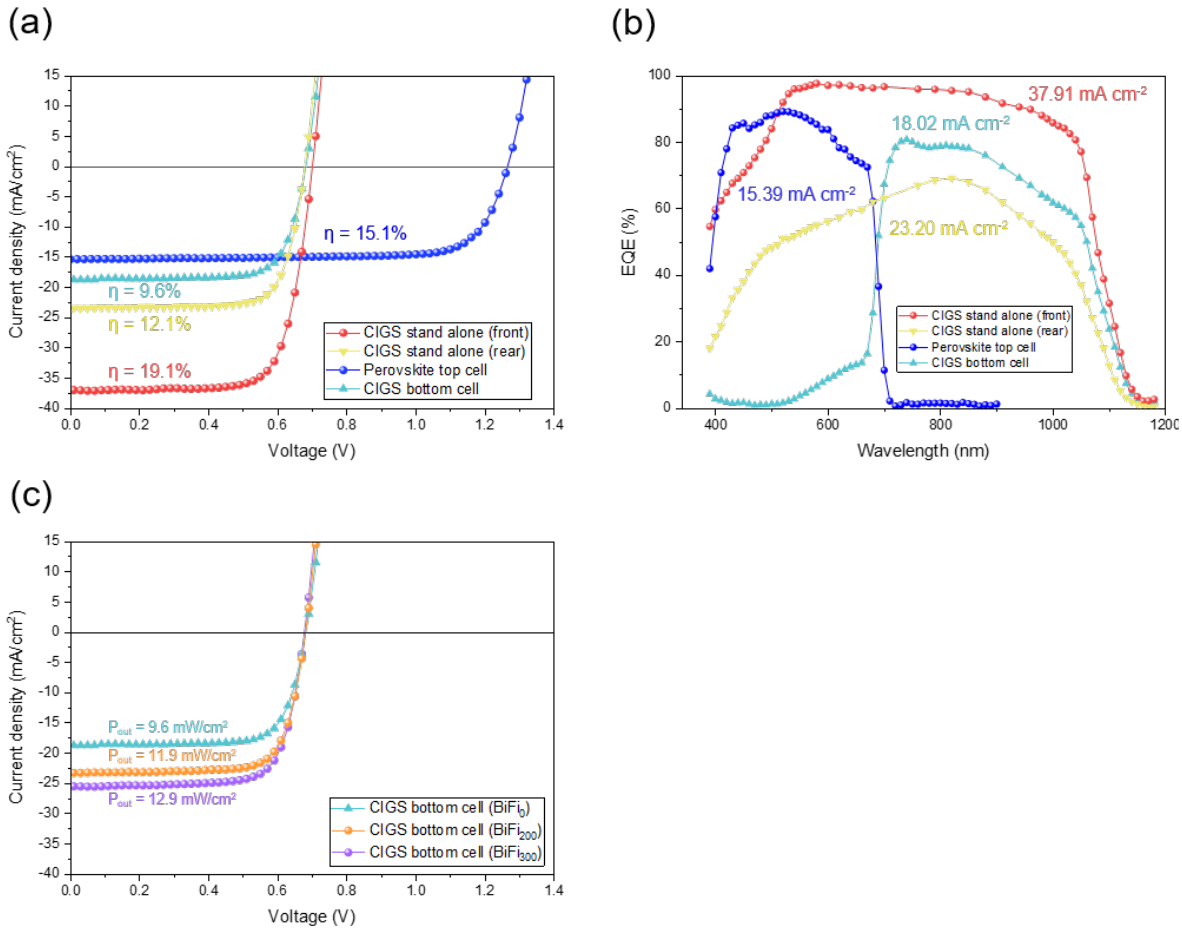

Figure 6.22: Bifacial perovskite/CIGS tandem in four terminal configuration. (a) J-V curves and the corresponding power conversion efficiencies (b) EQE curves and the corresponding EQE J_{SC} of a perovskite/CIGS bifacial 4-T tandem solar cells as well as of its individual subcells. (c) J-V curves and the corresponding power conversion efficiencies of the CIGS cell as the bottom cell under 0%, 20% and 30% rear albedo illumination.

A further application of bifacial CIGS cells is all-thin-film 2-terminal bifacial perovskite/CIGS tandem solar devices. With monofacial tandem devices, perovskite with wide-bandgap (> 1.65 eV) are favored to satisfy the current matching condition. However, such layers typically suffer from halide segregation [142, 143], making its long-term stability more challenging. With a bifacial tandem structure, the additional rear illumination can boost the J_{SC} in the bottom cell and satisfy the current matching condition with

Solar Cells	V_{OC} (V)	J_{SC} (mA/cm^2)	FF (%)	η (%)	Power density relative to front incident irradiance of 100 mW/cm^2 (%)	gain (mW/cm^2)
Perovskite top cell	1.268	15.33	77.9	15.1		
CIGS (stand alone)	0.693	36.99	74.4	19.1		
CIGS bottom cell	0.674	18.90	75.7	9.6		
CIGS rear illumination (1 sun)	0.679	23.40	76.1	12.1		
CIGS bottom cell with 20% albedo ($BiFi_{200}$)	0.680	23.28	75.3		11.9	
CIGS bottom cell with 30% albedo ($BiFi_{300}$)	0.678	25.51	74.5		12.9	
Perovskite/CIGS 4-terminal bifacial tandems ($BiFi_{200}$)					27.0	7.9
Perovskite/CIGS 4-terminal bifacial tandems ($BiFi_{300}$)					28.0	8.9

Table 6.4: J-V parameters of the bifacial tandem solar cells

a perovskite top cell with reduced bandgap. Anticipated high performance and potentially improved stability of bifacial monolithic perovskite/CIGS tandem solar cells could feature a prominent place in future photovoltaics markets.

6.8 Conclusion

We have demonstrated a record bifacial CIGS solar cell with efficiencies of 19.77% and 10.89% under the front and rear illumination. A power generation density of 23.0 mW/cm^2 $BiFi_{300}$ is foreseen, which is comparable to the CIGS record for mono-facial configuration.

By adding a small amount of Ag (4-5% AAC), absorbers with high quality were obtained with a low-temperature deposition process. The low-temperature process induces a range of benefits to device performance. First, it prevents the formation of detrimental GaO_x at the CIGS/ITO interface, which solves the issues with FF and R_s. Second, it enables the use of µm-thick absorbers with pronounced Ga back gradients. Large gradients help suppress carrier recombination near/at the back interface, thus increasing V_{OC} under both front and back illumination, and also increase the penetration depth of light under rear illumination, mitigating carrier loss and boosting J_{SC}. Further, low-temperature CIGS deposition processes mitigate the degradation of optical parasitic absorption in the ITO back contact. Overall, the developed process significantly improves the device PCE and J_{SC} under rear illumination, with little to no compromise on device performance under

front illumination. However, under rear illumination, J_{SC} remains the bottleneck to higher performance, limited by parasitic absorption losses in the transparent back contacts and carrier recombination at back interface due to non-passivated back contacts.

Finally, we demonstrated a bifacial perovskite/CIGS tandem device in 4-terminal configuration, achieving power generation densities of 27.0 mW/cm^2 $BiFi_{200}$ and 28.0 mW/cm^2 $BiFi_{300}$, respectively. The potential for high performance and improving stability in 2-terminal bifacial perovskite/CIGS tandem devices is also discussed. Last but not least, we directly fabricate a bifacial CIGS device on the flexible substrate without a lift-off process. This demonstration is the first step toward technology transfer to roll-to-roll industrial processing. Further improvement in device performance and upscaling development are the next steps for bringing this technology to the commercial market.

6.9 Sample references

CIGS	T303	T353	T413	T453	Certified	PI
Sample	TL3205	TL3206	TL3223	TL3224	TL3230	TL3235

Table 6.5: Internal sample naming for ACIGS solar cells in Chapter 6

	Sample
303 °C	TL3205
353 °C	TL3206, TL3220, TL3221, TL3225 TL3226, TL3228, TL3229, TL3230
413 °C	TL3209, TL3223
453 °C	TL3210, TL3224

Table 6.6: Samples used in **Figure 6.11**

7 Conclusion remarks and outlook

In this thesis different key components for high performance bifacial CIGS solar cells were developed and investigated. Based on the data presented in this thesis, the key findings in view of the aims stated in Section 1.5 are summarized as follows.

- Modified Ga and In evaporation rates in the first stage of co-evaporation process and the early stage In-free process successfully introduce steeper and higher [Ga]/([Ga]+[In]) (GGI) back gradings in CIGS absorbers. Both SEM cross-sectional images and Urbach tails show no noticeable degradation in the morphology and material quality of the absorbers. For ΔGGI between 0.2 and 0.5, TRPL carrier lifetime and V_{OC} deficit of the devices present a high dependency on ΔGGI. The results show that a ΔGGI value of at least 0.5 is required to effectively suppress the back interface recombination, highlighting the importance of the grading control in high-performance CIGS solar cells.

- The Ag precursor layer method can be implemented into our current CIGS co-evaporation system without modification to CIGS deposition equipment nor major process change. By adding a small amount of Ag (about 4% - 5% in AAC), larger grain size and enhanced elemental inter-diffusion are observed. Compared with the reference CIGS devices, the efficiency of the champion cell of ACIGS devices on glass substrates was improved from 18.9% to 20.4%, mainly driven by reduced V_{OC} deficit and increased *FF*. Furthermore, the transferability of the Ag precursor layer method

to PI substrates is also demonstrated. A CIGS solar cell with PCE of 20.1% was obtained on PI substrate.

- With the help of Ag alloying, the CIGS deposition temperature can be significantly reduced while still maintaining high material quality. The process temperature window of absorber deposition for high performance CIGS solar cells is widened by around 50 °C. Only 0.5% and 1.6% reduction in absolute efficiencies are observed by reducing T_{sub} by 60 °C and 110 °C, respectively. High efficiencies for such low-temperature fabricated CIGS is driven by less V_{OC} degradation. As compared to Ag-free CIGS, the lower V_{OC} degradation is attributed to better morphology and large grain size even for low T_{sub}. From the electronics prospective, less doping reduction for low T_{sub} is the main reason for less V_{OC} degradation.

- Normally the Cu diffusion rate is a bottleneck for low-temperature CIGS deposition process. The accumulation of Cu on the surface hinders the use of end-point detection and the recrystallization. With the presence of Ag, Cu diffusion is increased, extending the lower bound of process temperature of absorber deposition. Ag increases the Cu diffusion kinetics in the layers during growth, showing the potential for fast industrial processes to achieve complete layer recrystallization with minimized Cu excess requirement.

- For bifacial CIGS devices, the GaO_x formation at the CIGS/ITO interface is the main limiting factor for the performance under front illumination. Thanks to silver-promoted low-temperature process, the formation of the GaO_x interlayer can be suppressed while maintaining good absorber quality. No GaO_x was observed in both STEM images and EDX depth profilings with T_{sub} below 353 °C. Without the GaO_x formation at CIGS/ITO interface, increased *FF* from reduced R_{s} results in higher PCE under front illumination.

- Under rear illumination, the low J_{SC} due to short diffusion length and high back interface recombination is the main limiting factor for the performance of bifacial CIGS solar cells. Ag promoted low-temperature process enables even higher and

steeper Ga back gradings, which not only suppresses carrier recombination near/at the back interface with stronger effective electrical field, but also increasees the penetration depth of the light, therfore, mitigating the loss of the photogenerated charge carriers. Moreover, low-temperature processes mitigate the degradation of optical parasitic absorption in the ITO back contact. In total, a gain of close to 8 mA/cm^2 in J_{SC} with T_{sub} of 353 was obtained as compared to high temperature process (453 °C).

- With small amount of Ag (about 4% - 5% in AAC), an optimal T_{sub} of around 350 °C strikes a good balance between:
  - ITO/CIGS interface properties
  - absorber quality
  - suitable Ga gradient
  - better optical/electrical properties in ITO back contact

  A record bifacial device was obtained with efficiencies of 19.77% and 10.89% under front and rear one sun illumination, as independently certified by Fraunhofer ISE. A bifaciality of 55% is achieved. Under 30% albedo, a power generation density of 23.0 mW/cm^2 BiFi_{300} is foreseen.

- Direct fabrication of bifacial CIGS solar cells on flexible substrates is demonstrated for the first time. To further increase J_{SC} under rear illumination limited by absorption in the substartes, more transparent flexible substrates like CPIs are possible candidates. However, some engineering issues from laser scribing still need to be solved.

- The first bifacial perovskite/CIGS tandem solar cell in a 4-terminal configuration is presented, achieving a power generation density of 28.0 mW/cm^2 BiFi_{300} with a gain of 8.9 mW/cm^2 as compared to the performance of the stand-alone CIGS cell.

Outlook

Fast industrial deposition process

Ag-alloying successfully widened the deposition process window of CIGS absorbers by increasing Cu diffusion at low temperature. The increased Cu diffusion in presence of Ag suggested that the deposition rates of Cu in the second stage of the three-stage co-evaporation process may be increased. It shows the potential of both increasing the throughput and reducing the thermal budget in industrial deposition process. In addition, the requirements on the Cu excess at the end of the second stage may be relaxed while ensuring complete layer recrystallization in fast industrial deposition processes.

Improvement of the bifaciality

Despite improved J_{SC} of bifacial CIGS solar cells under rear illumination was presented in this thesis, the J_{SC} loss due to high back interface recombination is still substantial, which remains the main reason for low bifaciality ($\approx 55\%$) as compared to other technology like silicon ($> 90\%$). To reduce the back interface recombination rate, there are two main strategies: one is to reduce the carrier concentration near the back interface; the other is to directly reduce the recombination velocity at the interface, such as interface engineering via passivation or material engineering with selective contacts. While the former is the strategy chosen in this thesis, the latter is normally considered more effective. There are already some studies dedicated to the interface engineering, however, lack of works focusing on material engineering. One of the possible material engineering strategies is to ultilize the hole selective contacts to reduce the back interface recombination. It is worthy to note that commonly used hole selective layers in other technologies are oxide-based materials like MoO_x, VO_x, WO_x, and NiO_x. If those oxides were also used as hole selective layers in bifacial CIGS solar cells, the silver-promoted low-temperature process developed in this thesis may still play an important role to suppress the GaO_x formation at the CIGS/hole selective layer interface.

Other device architectures

Apart from 4-T bifacial tandem and flexible bifacial CIGS devices presented in this thesis, other promising device architectures which were limited by the formation of GaO_x interlayer are now worthy of revisiting, for example, semi-transparent CIGS and reflective-back-contact devices. A further application of bifacial CIGS cells is 2-terminal bifacial perovskite/CIGS tandem solar devices. With a bifacial tandem structure, the additional albedo from the rear side can increase the J_{SC} in the bottom cell and satisfy the current matching condition with a perovskite top cell with reduced bandgap, therefore, less halide segregation issue. Anticipated high performance and potentially improved stability of bifacial monolithic perovskite/CIGS tandem solar cells could feature a prominent place in future photovoltaics markets.

8 Acknowledgments

First and foremost, I would like to thank the thin film and photovoltaic group for fostering a welcoming and stimulating environment. It was a pleasure to work alongside experts who were always willing to share their knowledge and expertise. The group's collaborative spirit was a constant source of motivation and encouragement. And a warm thanks for the unconditional support goes to my family, especially my twin brother, and friends in Taiwan, Switzerland, and around the world.

I am particularly indebted to Professor Ayodhya N. Tiwari for granting me the opportunity of pursuing PhD and for his guidance, both as a experienced researcher and as a thoughtful human being, over the past 4.5 years. I am also grateful to Dr. Romain Carron, whose unwavering support and encouragement have created the ideal environment for my research to thrive. His confidence in my abilities and willingness to allow me to explore new ideas without constraints were instrumental to the success of this thesis. I would like to extend my thanks to Dr. Stephan Bücheler, who initially brought me into the group and supervised my work during the first year of my PhD. I am also thankful to Prof. Jürg Leuthold from ETH Zürich and Prof. Marika Edoff from Uppsala University for examining my work.

I owe a debt of gratitude to my colleagues in the thin-film chalcogenide sub-group, especially Maximilian Krause and Dr. Ramis Hertwig. Their camaraderie and support were invaluable both professionally and personally. Also thanks to Simon Moser for being an awesome office mate. I would like to thank Dr. Shiro Nishiwaki for his assistance whenever I had troubles from MBE in the lab, as well as former group members Dr. Mario Ochoa, Dr. Thomas Feurer, Dr. Johannes Löckinger, and Dr. Enrico Avancini for their patience and support during my first year of research. In particular, I am grateful to Dr. Mario Ochoa for continuing to engage in daily discussions on my research even after leaving the group.

Thanks to all former and present members of the thin film and photovoltaic group. I always feel privileged to have shared these past years with those exceptional people, both inside and outside the lab. Special thanks to Abdessalem Aribia, who offered lots of company during my best and worst time in my PhD. And for Severin Siegrist, that we had so much great beer, coffee, brunch, and fun together. And definitely also Dr. Jordi Sastre, Dr. Thierry Moser, Dr. Moritz Futscher, Dr. Galo Torres Sevilla, Andre Müller, Beatriz Alvarez Restrepo, Huagui Lai, Radha Kothandaraman, Nicolas Osenciat, Dr. Yan Jiang, Dr. Xiaoxiao Sun, Dr. Evgeniia Gilshtein, Joel Casella, Marek Chrapa and others. I am also extremely thankful to Prof. Tzu-Ying Lin for having such a great collaboration in my publication and giving me lots of valuable suggestions. Furthermore, I would like to extend my deepest gratitude to David Stalder for his invaluable contribution in establishing and maintaining the laboratory tools and machines that were vital for the success of this research. Additionally, I want to acknowledge the unwavering support of Dr. Yaroslav Romanyuk in resolving various issues that arose in our daily operations. And a heartfelt thanks goes to Jolanda Beaton for her outstanding work in managing administrative tasks and for creating a conducive work environment for us all. Without her efforts, we wouldn't be able to achieve our goals.

Last but not least, I offer my sincerest thanks to myself - the one who kept pushing forward despite the obstacles and doubts. This journey has been a rollercoaster of ups and downs, a tango of highs and lows, a bittersweet symphony of joy and sorrow. Those moments of struggle and confusion, when the path ahead seemed hazy and uncertain, now reveal their true purpose in retrospect. Each challenge, every setback, and every failure - now I can connect those dots looking backforwards. Through it all, now I truly believe that every cloud has a **silver** lining.

9 Curriculum vitae

Shih-Chi Yang

Date of birth: 28.12.1989
Place of birth: Yilan, Taiwan
Nationality: Taiwanese

06/2018 - 02/2023	**PhD student**, Laboratory for Thin Films and Photovoltaics, Empa, Dübendorf, Switzerland
01/2018 - 03/2018	**Senior panel process engineer**, Apple, Taiwan
03/2016 - 12/2017	**R&D process engineer**, Applied Materials, Taiwan
08/2012 - 06/2014	**Master of Science in Eletronics Engineering**, National Taiwan University, Taiwan
08/2008 - 06/2012	**Bachelor of Science in Material Science and Engineering**, National Taiwan University, Taiwan

10 List of publications

Publications

1. Krause, Maximilian, Shih-Chi Yang, Simon Moser, Shiro Nishiwaki, Ayodhya N. Tiwari, and Romain Carron. "Silver-alloyed low bandgap $CuInSe_2$ solar cells for tandem applications." *Solar RRL* (2023): 2201122.

2. Yang, Yuxuan, Tao Zhao, Ming-Hua Li, Xiaoxue Wu, Mingyue Han, Shih-Chi Yang, Qiaoling Xu et al. "Passivation of positively charged cationic defects in perovskite with nitrogen-donor crown ether enabling efficient perovskite solar cells." *Chemical Engineering Journal* 451 (2023): 138962.

3. Yang, Shih-Chi, Tzu-Ying Lin, Mario Ochoa, Huagui Lai, Radha Kothandaraman, Fan Fu, Ayodhya N. Tiwari, and Romain Carron. "Efficiency boost of bifacial $Cu(In,Ga)Se_2$ thin-film solar cells for flexible and tandem applications with silver-assisted low-temperature process." *Nature Energy* (2022): 1-12.

4. Carron, Romain, Shiro Nishiwaki, Shih-Chi Yang, Mario Ochoa, Xiaoxiao Sun, Thomas Feurer, and Ayodhya Tiwari. "Heat-light soaking treatments for high-performance CIGS solar cells on flexible substrates." *Preprint* (2022).

5. Zhang, Tiankai, Feng Wang, Hak-Beom Kim, In-Woo Choi, Chuanfei Wang, Eunkyung Cho, Rafal Konefal, Yuttapoom Puttisong, Kosuke Terado, Libor Kobera, Mengyun Chen, Mei Yang, Sai Bai, Bowen Yang, Jiajia Suo, Shih-Chi Yang, Xianjie Liu, Fan Fu et al. "Ion-modulated radical doping of spiro-OMeTAD for more efficient and stable perovskite solar cells." *Science* 377, no. 6605 (2022): 495-501.

6. Moser, Thierry, Radha Kothandaraman, Shih-Chi Yang, Arnaud Walter , Severin Siegrist, Huagui Lai, Evgeniia Gilshtein, Ayodhya N. Tiwari and Fan Fu. "Understanding the Formation Process of Perovskite Layers Grown by Chemical Vapour Deposition." *Frontiers in Energy Research* 10 (2022): 883882.

7. Bolat, Sami, Evangelos Agiannis, Shih-Chi Yang, Moritz H. Futscher, Abdesselam Aribia, Ivan Shorubalko, and Yaroslav E. Romanyuk. "Engineering Bilayer $AlO_x/YAlO_x$ Dielectric Stacks for Hysteresis-Free Switching in Solution-Processed Metal-Oxide Thin-Film Transistors." *Frontiers in Electronics* 2 (2022): 26.

8. Ochoa, Mario, Shih-Chi Yang, Shiro Nishiwaki, Ayodhya N. Tiwari, and Romain Carron. "Charge carrier lifetime fluctuations and performance evaluation of Cu(In,Ga)Se_2 absorbers via time-resolved-photoluminescence microscopy." *Advanced Energy Materials* 12, no. 3 (2022): 2102800.

9. Siegrist, Severin, Shih-Chi Yang, Evgeniia Gilshtein, Xiaoxiao Sun, Ayodhya N. Tiwari, and Fan Fu. "Triple-cation perovskite solar cells fabricated by a hybrid PVD/blade coating process using green solvents." *Journal of Materials Chemistry A* 9, no. 47 (2021): 26680-26687.

10. Teng, Pengpeng, Sebastian Reichert, Weidong Xu, Shih-Chi Yang, Fan Fu, Yatao Zou, Chunyang Yin et al. "Degradation and self-repairing in perovskite light-emitting diodes." *Matter* 4, no. 11 (2021): 3710-3724.

11. Ochoa, Mario, Shiro Nishiwaki, Shih-Chi Yang, Ayodhya N. Tiwari, and Romain Carron. "Lateral Charge Carrier Transport in Cu(In,Ga)Se_2 Studied by Time-Resolved Photoluminescence Mapping." *physica status solidi (RRL)-Rapid Research Letters* 15, no. 10 (2021): 2100313.

12. Yang, Shih-Chi, Jordi Sastre, Maximilian Krause, Xiaoxiao Sun, Ramis Hertwig, Mario Ochoa, Ayodhya N. Tiwari, and Romain Carron. "Silver-Promoted High-Performance (Ag,Cu)(In,Ga)Se_2 Thin-Film Solar Cells Grown at Very Low Temperature." *Solar RRL* 5, no. 5 (2021): 2100108.

13. Yang, Shih-Chi, Mario Ochoa, Ramis Hertwig, Abdessalem Aribia, Ayodhya N. Tiwari, and Romain Carron. "Influence of Ga back grading on voltage loss in low-temperature co-evaporated Cu(In,Ga)Se_2 thin film solar cells." *Progress in Photovoltaics: Research and Applications* 29, no. 6 (2021): 630-637.

14. Jiang, Yan, Shih-Chi Yang, Quentin Jeangros, Stefano Pisoni, Thierry Moser, Stephan Buecheler, Ayodhya N. Tiwari, and Fan Fu. "Mitigation of vacuum and illumination-induced degradation in perovskite solar cells by structure engineering." *Joule* 4, no. 5 (2020): 1087-1103.

15. Hertwig, Ramis, Shiro Nishiwaki, Mario Ochoa, Shih-Chi Yang, Thomas Feurer, Evgeniia Gilshtein, Ayodhya N. Tiwari, and Romain Carron. "ALD-ZnMgO and absorber surface modifications to substitute CdS buffer layers in co-evaporated CIGSe solar cells." *EPJ Photovoltaics* 11 (2020):12.

16. Carron, Romain, Shiro Nishiwaki, Thomas Feurer, Ramis Hertwig, Enrico Avancini, Johannes Löckinger, Shih-Chi Yang, Stephan Buecheler, and Ayodhya N. Tiwari. "Advanced alkali treatments for high-efficiency Cu(In,Ga)Se_2 solar cells on flexible substrates." *Advanced Energy Materials* 9, no. 24 (2019): 1900408.

Conference contributions

1. MRS Spring Meeting 2023
   10-14.04.2023 in San Francisco, USA
   Oral presentation
   "High performance bifacial Cu(In,Ga)Se_2 thin film solar cells and its application in tandem devices with high power generation density"

2. PVSEC-33
   13-17.11.2022 in Nagoya, Japan
   Oral presentation
   "Advances in ACIGS Thin Film Photovolatics For Bifacial Flexible And Tandem Applications"
3. WCPEC-8
   26-30.09.2022 in Milan, Italy
   Oral presentation **(Best Student Award)**
   "Efficiency boost of bifacial Cu(In,Ga)Se_2 thin-film solar cells for flexible and tandem applications with silver-assisted low-temperature process"
4. EMRS Spring
   30.05-03.06.2022 Online
   Oral presentation
   "ACIGS thin film solar cells with more than 23% bifacial efficiencies under 30% albedo condition"
5. MRS Spring Meeting 2022
   09-13.05.2022 in Honolulu, USA
   Oral presentation
   "A Novel Strategy for Boosting Bifacial Efficiency of Cu(In,Ga)Se_2 Solar Cells"
6. Nationale Photovoltaik-Tagung 2022
   29-30.03.2022 in Bern, Switzerland
   Poster presentation
   "Thin thin solar cell research at EMPA"
7. EUPVSEC 2021
   06-10.09.2021 Online
   Visual presentation
   "Impact of silver alloying on the device performance and stability in low temperature grown ACIGS Solar Cells"
8. Nationale Photovoltaik-Tagung 2021
   01-02.07.2021 in Bern, Switzerland
   Poster presentation
   "Thin thin Cu(In,Ga)Se_2 for flexible and lightweight photovoltaic applications"
9. EMRS Spring
   31.05-04.06.2021 Online
   Oral presentation
   "Silver promoted high performance ACIGS thin film solar cells grown at very low temperature"
10. EUPVSEC 2020
    07-11.09.2020 Online
    Oral presentation
    "(Ag,Cu)(In,Ga)Se_2 Solar Cells Grown at Low Temperature with Ag Precursor Layer Method"
11. EMRS Spring Meeting 2020
    25-29.05.2020 Online
    Oral presentation

"Investigation of back grading influence on voltage loss in low-temperature co-evaporated Cu(In,Ga)Se2 thin films"

12. IW-CIGSTech 10
    23-24.05.2019 in Paris, France
    Poster presentation
    "Gallium grading modifications for effective passivation of molybdenum back contact in Cu(In,Ga)Se_2 solar cells"

Bibliography

[1] Christiana Figueres et al. “Three years to safeguard our climate”. In: *Nature* 546.7660 (2017), pp. 593–595.

[2] IEA. “Solar PV power generation in the Net Zero Scenario, 2000-2030”. In: *Solar-PV* (2021), https://www.iea.org/data-and-statistics/data-tools/net-zero-by-2050-data\bibrangedashexplorer.

[3] Marta Victoria et al. “Solar photovoltaics is ready to power a sustainable future”. In: *Joule* 5.5 (2021), pp. 1041–1056.

[4] IEA. “Solar PV power generation in the Net Zero Scenario, 2000-2030”. In: *Solar-PV* (2021), https://www.iea.org/data-and-statistics/charts/solar-pv-power-generation-in-the-net-zero-scenario-2000\bibrangedash2030.

[5] Thomas Feurer et al. “Progress in thin film CIGS photovoltaics–Research and development, manufacturing, and applications”. In: *Progress in Photovoltaics: Research and Applications* 25.7 (2017), pp. 645–667.

[6] Motoshi Nakamura et al. “Cd-Free Cu(In,Ga)(Se,S) $_2$ Thin-Film Solar Cell With Record Efficiency of 23.35%”. en. In: *IEEE J. Photovoltaics* 9.6 (Nov. 2019), pp. 1863–1867. ISSN: 2156-3381, 2156-3403. DOI: 10.1109/JPHOTOV.2019.2937218.

[7] Avancis. “New world record for CIGS efficiency”. In: *Press release* (2022), https://www.avancis.de/en/magazine/pr\bibrangedashefficiency.

[8] EMPA. “Flexible solar cells with record efficiency of 22.2%”. In: *Press release* (2022), https://www.empa.ch/web/s604/solarzellen\bibrangedashrekord.

[9] JC Mikkelsen. “Ternary phase relations of the chalcopyrite compound CuGaSe2”. In: *Journal of Electronic Materials* 10.3 (1981), pp. 541–558.

[10] Y. Zhong. “Study on the application of surface copper indium gallium selenium thin films in solar cells”. In: *the Master Degree Dissertation of National Cheng Kung University* (2009).

[11] Roland Scheer and Hans-Werner Schock. *Chalcogenide photovoltaics: physics, technologies, and thin film devices*. John Wiley & Sons, 2011.

[12] Billy J Stanbery. "Copper indium selenides and related materials for photovoltaic devices". In: *Critical reviews in solid state and materials sciences* 27.2 (2002), pp. 73–117.

[13] Nowshad Amin. "Promises of Cu (In, Ga) Se2 thin film solar cells from the perspective of material properties, fabrication methods and current research challenges". In: *Journal of Applied Sciences* 11.3 (2011), pp. 401–410.

[14] Thomas Dittrich. *Materials concepts for solar cells*. World Scientific, 2015.

[15] David J Schroeder, Gene D Berry, and Angus A Rockett. "Gallium diffusion and diffusivity in CuInSe2 epitaxial layers". In: *Applied Physics Letters* 69.26 (1996), pp. 4068–4070.

[16] M Souilah et al. "Structural investigation of the Cu2Se–In2Se3–Ga2Se3 phase diagram, X-ray photoemission and optical properties of the Cu1- z (In0. 5Ga0. 5) 1+ z/3Se2 compounds". In: *Journal of Solid State Chemistry* 183.10 (2010), pp. 2274–2280.

[17] SB Zhang et al. "Defect physics of the CuInSe 2 chalcopyrite semiconductor". In: *Physical Review B* 57.16 (1998), p. 9642.

[18] SB Zhang, Su-Huai Wei, and Alex Zunger. "Stabilization of ternary compounds via ordered arrays of defect pairs". In: *Physical review letters* 78.21 (1997), p. 4059.

[19] JCW Folmer et al. "Structural and solar conversion characteristics of the (Cu2Se) x (In2Se3) 1- x system". In: *Journal of The Electrochemical Society* 132.6 (1985), p. 1319.

[20] R Herberholz et al. "Phase segregation, Cu migration and junction formation in Cu (In, Ga) Se2". In: *The European Physical Journal-Applied Physics* 6.2 (1999), pp. 131–139.

[21] Clas Persson et al. "n-type doping of CuIn Se 2 and CuGa Se 2". In: *Physical Review B* 72.3 (2005), p. 035211.

[22] Tsuyoshi Maeda and Takahiro Wada. "Characteristics of chemical bond and vacancy formation in chalcopyrite-type CuInSe2 and related compounds". In: *physica status solidi c* 6.5 (2009), pp. 1312–1316.

[23] Su-Huai Wei and Alex Zunger. "Band offsets and optical bowings of chalcopyrites and Zn-based II-VI alloys". In: *Journal of Applied Physics* 78.6 (1995), pp. 3846–3856.

[24] Susanne Siebentritt et al. “The electronic structure of chalcopyrites—bands, point defects and grain boundaries”. In: *Progress in Photovoltaics: Research and Applications* 18.6 (2010), pp. 390–410.

[25] Romain Carron et al. “Refractive indices of layers and optical simulations of Cu (In, Ga) Se2 solar cells”. In: *Science and Technology of advanced MaTerialS* 19.1 (2018), pp. 396–410.

[26] Rongzhen Chen and Clas Persson. “Band-edge density-of-states and carrier concentrations in intrinsic and p-type CuIn1- x Ga x Se2”. In: *Journal of Applied Physics* 112.10 (2012), p. 103708.

[27] LL Kazmerski et al. “Growth and properties of vacuum deposited CuInSe2 thin films”. In: *Journal of Vacuum Science and Technology* 13.1 (1976), pp. 139–144.

[28] Reid A Mickelsen and Wen S Chen. *Apparatus for forming thin-film heterojunction solar cells employing materials selected from the class of I-III-VI2 chalcopyrite compounds*. US Patent 4,392,451. July 1983.

[29] Reiner Klenk et al. “A model for the successful growth of polycrystalline films of CuInSe2 by multisource physical vacuum evaporation”. In: *Advanced Materials* 5.2 (1993), pp. 114–119.

[30] Daniel Abou-Ras et al. “Innovation highway: Breakthrough milestones and key developments in chalcopyrite photovoltaics from a retrospective viewpoint”. In: *Thin Solid Films* 633 (2017), pp. 2–12.

[31] Andrew M Gabor et al. “High-efficiency CuIn x Ga1- x Se2 solar cells made from (In x, Ga1- x) 2Se3 precursor films”. In: *Applied physics letters* 65.2 (1994), pp. 198–200.

[32] Naoki Kohara et al. “Preparation of device-quality Cu (In, Ga) Se2 thin films deposited by coevaporation with composition monitor”. In: *Japanese journal of applied physics* 34.9A (1995), p. L1141.

[33] John Kessler, J Scholdstrom, and Lars Stolt. “Rapid Cu (In, Ga) Se/sub 2/growth using" end point detection"”. In: *Conference Record of the Twenty-Eighth IEEE Photovoltaic Specialists Conference-2000 (Cat. No. 00CH37036)*. IEEE. 2000, pp. 509–512.

[34] John Kessler et al. “Cu (In, Ga) Se2 thin films grown with a Cu-poor/rich/poor sequence: growth model and structural considerations”. In: *Progress in Photovoltaics: Research and Applications* 11.5 (2003), pp. 319–331.

[35] D Rudmann et al. “Na incorporation into Cu (In, Ga) Se 2 for high-efficiency flexible solar cells on polymer foils”. In: *Journal of Applied Physics* 97.8 (2005), p. 084903.

[36] Adrian Chirilă et al. “Potassium-Induced Surface Modification of Cu(In,Ga)Se 2 Thin Films for High-Efficiency Solar Cells”. en. In: *Nature Materials* 12.12 (Dec. 2013), pp. 1107–1111. ISSN: 1476-4660. DOI: 10.1038/nmat3789.

[37] Humberto Rodriguez-Alvarez et al. “Formation of CuInSe2 and CuGaSe2 Thin-Films Deposited by Three-Stage Thermal Co-Evaporation: A Real-Time X-Ray Diffraction and Fluorescence Study”. In: *Advanced Energy Materials* 3.10 (2013), pp. 1381–1387.

[38] Paul Pistor et al. “Real time observation of phase formations by XRD during Ga-rich or In-rich Cu (In, Ga) Se2 growth by co-evaporation”. In: *physica status solidi (a)* 212.9 (2015), pp. 1897–1904.

[39] R Mainz et al. “Sudden stress relaxation in compound semiconductor thin films triggered by secondary phase segregation”. In: *Physical Review B* 92.15 (2015), p. 155310.

[40] H Stange et al. “Effect of Na presence during CuInSe2 growth on stacking fault annihilation and electronic properties”. In: *Applied Physics Letters* 107.15 (2015), p. 152103.

[41] M.A. Contreras et al. “High Efficiency Cu(In,Ga)Se/Sub 2/-Based Solar Cells: Processing of Novel Absorber Structures”. In: *Proceedings of 1994 IEEE 1st World Conference on Photovoltaic Energy Conversion - WCPEC (A Joint Conference of PVSC, PVSEC and PSEC)*. Vol. 1. Dec. 1994, 68–75 vol.1. DOI: 10.1109/WCPEC.1994.519811.

[42] T. Dullweber et al. “Back Surface Band Gap Gradings in Cu(In,Ga)Se2 Solar Cells”. en. In: *Thin Solid Films*. Proceeedings of Symposium N on Thin Film Photovoltaic-materials of the E-MRS Spring Conference 387.1 (May 2001), pp. 11–13. ISSN: 0040-6090. DOI: 10.1016/S0040-6090(00)01726-0.

[43] Thomas Feurer et al. “Single-Graded CIGS with Narrow Bandgap for Tandem Solar Cells”. en. In: *Science and Technology of Advanced Materials* 19.1 (Dec. 2018), pp. 263–270. ISSN: 1468-6996, 1878-5514. DOI: 10.1080/14686996.2018.1444317.

[44] Alex Niemegeers et al. “Model for electronic transport in Cu (In, Ga) Se2 solar cells”. In: *Progress in Photovoltaics: Research and Applications* 6.6 (1998), pp. 407–421.

[45] Reiner Klenk. "Characterisation and modelling of chalcopyrite solar cells". In: *Thin solid films* 387.1-2 (2001), pp. 135–140.

[46] Giovanna Sozzi, Fabrizio Troni, and Roberto Menozzi. "On the combined effects of window/buffer and buffer/absorber conduction-band offsets, buffer thickness and doping on thin-film solar cell performance". In: *Solar energy materials and solar cells* 121 (2014), pp. 126–136.

[47] M. Gloeckler and J.R. Sites. "Band-Gap Grading in Cu(In,Ga)Se2 Solar Cells". en. In: *Journal of Physics and Chemistry of Solids* 66.11 (Nov. 2005), pp. 1891–1894. ISSN: 00223697. DOI: 10.1016/j.jpcs.2005.09.087.

[48] Markus Gloeckler. "Device Physics of Copper(Indium,Gallium)Selenide(2) Thin-Film Solar Cells". English. Ph.D. United States – Colorado: Colorado State University, 2005. ISBN: 9780542268434.

[49] C Frisk et al. "Optimizing Ga-Profiles for Highly Efficient Cu(In, Ga)Se $_2$ Thin Film Solar Cells in Simple and Complex Defect Models". en. In: *J. Phys. D: Appl. Phys.* 47.48 (Dec. 2014), p. 485104. ISSN: 0022-3727, 1361-6463. DOI: 10.1088/0022-3727/47/48/485104.

[50] JH Boyle et al. "Structural and optical properties of (Ag, Cu)(In, Ga) Se2 polycrystalline thin film alloys". In: *Journal of Applied Physics* 115.22 (2014), p. 223504.

[51] Jan Keller et al. "Wide-gap (Ag, Cu)(In, Ga) Se2 solar cells with different buffer materials—A path to a better heterojunction". In: *Progress in Photovoltaics: Research and Applications* 28.4 (2020), pp. 237–250.

[52] Gregory M Hanket, Jonathan H Boyle, and William N Shafarman. "Characterization and device performance of (AgCu)(InGa) Se 2 absorber layers". In: *2009 34th IEEE Photovoltaic Specialists Conference (PVSC)*. IEEE. 2009, pp. 001240–001245.

[53] Lei Chen, JinWoo Lee, and William N Shafarman. "The Comparison of (Ag,Cu)(In,Ga)Se_2 and Cu(In,Ga)Se_2 Thin Films Deposited by Three-Stage Coevaporation". In: *IEEE Journal of Photovoltaics* 4.1 (2013), pp. 447–451.

[54] Peter T Erslev et al. "The electronic structure of Cu(In1-xGax) Se2 alloyed with silver". In: *Thin Solid Films* 519.21 (2011), pp. 7296–7299.

[55] Gayeon Kim et al. "Thin Ag Precursor Layer-Assisted Co-Evaporation Process for Low-Temperature Growth of Cu (In, Ga) Se2 Thin Film". In: *ACS applied materials & interfaces* 11.35 (2019), pp. 31923–31933.

[56] Marika Edoff et al. “High V oc in (Cu, Ag)(In, Ga) Se 2 Solar Cells”. In: *IEEE Journal of Photovoltaics* 7.6 (2017), pp. 1789–1794.

[57] Yunhai Zhao et al. “High efficiency CIGS solar cells by bulk defect passivation through Ag substituting strategy”. In: *ACS applied materials & interfaces* 12.11 (2020), pp. 12717–12726.

[58] MiaSolé. “MIASOLÉ ACHIEVES FLEXIBLE SUBSTRATE THIN-FILM SOLAR CELL EFFICIENCY OF 20.56 PERCENT”. In: *Press release* (2019), http://miasole.com/miasole-achieves-flexible-substrate-thin-film-solar-cell-efficiency-of-20-56\bibrangedashpercent/.

[59] M Balestrieri et al. “Structural characterization of coevaporated Cu (In, Ga) Se2 absorbers deposited at low temperature”. In: *Journal of Alloys and Compounds* 794 (2019), pp. 654–661.

[60] Shiro Nishiwaki et al. “Preparation of Cu (In, Ga) Se 2 thin films at low substrate temperatures”. In: *Journal of Materials Research* 16.2 (2001), pp. 394–399.

[61] Li Zhang et al. “Effects of substrate temperature on the structural and electrical properties of Cu (In, Ga) Se2 thin films”. In: *Solar Energy Materials and Solar Cells* 93.1 (2009), pp. 114–118.

[62] Massimo Mazzer et al. “Progress on low-temperature pulsed electron deposition of CuInGaSe2 solar cells”. In: *Energies* 9.3 (2016), p. 207.

[63] M Mazzer et al. “Bifacial CIGS solar cells grown by low temperature pulsed electron deposition”. In: *Solar Energy Materials and Solar Cells* 166 (2017), pp. 247–253.

[64] P Kuppusami and VS Raghunathan. *Status of pulsed laser deposition: challenges and opportunities*. 2006.

[65] B. Bissig. “Micro- and macroscopic characterization of recombination losses in high efficiency Cu(In,Ga)Se2 thin film solar cells”. In: *PhD thesis* (2018).

[66] Chintam Hanmandlu et al. “Bifacial perovskite solar cells featuring semitransparent electrodes”. In: *ACS applied materials & interfaces* 9.38 (2017), pp. 32635–32642.

[67] Sami Jouttijärvi et al. “Benefits of bifacial solar cells combined with low voltage power grids at high latitudes”. In: *Renewable and Sustainable Energy Reviews* 161 (2022), p. 112354.

[68] Odysseas Alexandros Katsikogiannis, Hesan Ziar, and Olindo Isabella. “Integration of bifacial photovoltaics in agrivoltaic systems: A synergistic design approach”. In: *Applied Energy* 309 (2022), p. 118475.

[69] R Kopecek and J Libal. "Towards large-scale deployment of bifacial photovoltaics". In: *Nature Energy* 3.6 (2018), pp. 443–446.

[70] Radovan Kopecek and Joris Libal. "Bifacial photovoltaics 2021: Status, opportunities and challenges". In: *Energies* 14.8 (2021), p. 2076.

[71] TS á Liang et al. "JP áSingh, W. áLuo, Y. áWang, AG áAberle, YS áKhoo". In: *Energy Environ. Sci* 12 (2019), p. 116.

[72] ITRPV. "International Technology Roadmap for Photovoltaic (ITRPV) - Results 2017". In: (2018), https://itrpv.net/Reports/Downloads/.

[73] Min Jeong Shin et al. "Semitransparent and bifacial ultrathin Cu (In, Ga) Se2 solar cells via a single-stage process and light-management strategy". In: *Nano Energy* 82 (2021), p. 105729.

[74] Tokio Nakada et al. "Novel device structure for Cu (In, Ga) Se2 thin film solar cells using transparent conducting oxide back and front contacts". In: *Solar energy* 77.6 (2004), pp. 739–747.

[75] Marc Daniel Heinemann et al. "Cu (In, Ga) Se2 superstrate solar cells: prospects and limitations". In: *Progress in Photovoltaics: Research and Applications* 23.10 (2015), pp. 1228–1237.

[76] Yu-Seung Son et al. "Control of structural and electrical properties of indium tin oxide (ITO)/Cu (In, Ga) Se2 interface for transparent back-contact applications". In: *The Journal of Physical Chemistry C* 123.3 (2019), pp. 1635–1644.

[77] Jan Keller et al. "Using hydrogen-doped In2O3 films as a transparent back contact in (Ag, Cu)(In, Ga) Se2 solar cells". In: *Progress in Photovoltaics: Research and Applications* 26.3 (2018), pp. 159–170.

[78] Takahito Nishimura et al. "Device design for high-performance bifacial Cu (In, Ga) Se2 solar cells under front and rear illuminations". In: *Solar Energy* 218 (2021), pp. 76–84.

[79] Cong Chen et al. "Interfacial engineering of a thiophene-based 2D/3D perovskite heterojunction for efficient and stable inverted wide-bandgap perovskite solar cells". In: *Nano Energy* 90 (2021), p. 106608.

[80] Daniel Abou-Ras, Thomas Kirchartz, and Uwe Rau. *Advanced characterization techniques for thin film solar cells*. Vol. 2. Wiley Online Library, 2011.

[81] T Walter et al. "Determination of defect distributions from admittance measurements and application to Cu (In, Ga) Se2 based heterojunctions". In: *Journal of applied physics* 80.8 (1996), pp. 4411–4420.

[82] LC Kimerling. “Influence of deep traps on the measurement of free-carrier distributions in semiconductors by junction capacitance techniques”. In: *Journal of Applied Physics* 45.4 (1974), pp. 1839–1845.

[83] Technical University of Munich Chair of Experimental Semiconductor Physics Walter Schottky Institute. “High-Resolution X-ray Diffraction”. In: (2020), https://www.ph.tum.de/academics/org/labs/fopra/docs/userguide\bibrangedash08.en.pdf.

[84] Shih-Chi Yang et al. “Influence of Ga back grading on voltage loss in low-temperature co-evaporated Cu (In, Ga) Se2 thin film solar cells”. In: *Progress in Photovoltaics: Research and Applications* 29.6 (2021), pp. 630–637.

[85] Romain Carron et al. “Advanced Alkali Treatments for High-Efficiency Cu(In,Ga)Se2 Solar Cells on Flexible Substrates”. en. In: *Advanced Energy Materials* 9.24 (2019), p. 1900408. ISSN: 1614-6840. DOI: 10.1002/aenm.201900408.

[86] Takuya Kato et al. “Record Efficiency for Thin-Film Polycrystalline Solar Cells Up to 22.9% Achieved by Cs-Treated Cu(In,Ga)(Se,S)2”. In: *IEEE Journal of Photovoltaics* 9.1 (Jan. 2019), pp. 325–330. ISSN: 2156-3403. DOI: 10.1109/JPHOTOV.2018.2882206.

[87] Philip Jackson et al. “Properties of Cu(In,Ga)Se2 Solar Cells with New Record Efficiencies up to 21.7%”. en. In: *physica status solidi (RRL) – Rapid Research Letters* 9.1 (2015), pp. 28–31. ISSN: 1862-6270. DOI: 10.1002/pssr.201409520.

[88] Mario Ochoa et al. “Challenges and Opportunities for an Efficiency Boost of next Generation Cu(In,Ga)Se2 Solar Cells: Prospects for a Paradigm Shift”. en. In: *Energy Environ. Sci.* (May 2020). ISSN: 1754-5706. DOI: 10.1039/D0EE00834F.

[89] T. Klinkert et al. “Ga Gradients in Cu(In,Ga)Se $_2$: Formation, Characterization, and Consequences”. en. In: *Journal of Renewable and Sustainable Energy* 6.1 (Jan. 2014), p. 011403. ISSN: 1941-7012. DOI: 10.1063/1.4866255.

[90] Romain Carron et al. “Refractive Indices of Layers and Optical Simulations of Cu(In,Ga)Se2 Solar Cells”. In: *Science and Technology of Advanced Materials* 19.1 (Dec. 2018), pp. 396–410. ISSN: 1468-6996. DOI: 10.1080/14686996.2018.1458579.

[91] Sunghun Jung et al. “Effects of Ga Contents on Properties of CIGS Thin Films and Solar Cells Fabricated by Co-Evaporation Technique”. en. In: *Current Applied Physics* 10.4 (July 2010), pp. 990–996. ISSN: 1567-1739. DOI: 10.1016/j.cap.2009.11.082.

[92] Jakapan Chantana et al. “Examination of Relationship between Urbach Energy and Open-Circuit Voltage Deficit of Flexible Cu(In,Ga)Se2 Solar Cell for Its Improved Photovoltaic Performance”. In: *ACS Appl. Energy Mater.* 2.11 (Nov. 2019), pp. 7843–7849. DOI: 10.1021/acsaem.9b01271.

[93] Uwe Rau. “Reciprocity Relation between Photovoltaic Quantum Efficiency and Electroluminescent Emission of Solar Cells”. In: *Phys. Rev. B* 76.8 (Aug. 2007), p. 085303. DOI: 10.1103/PhysRevB.76.085303.

[94] Thomas P. Weiss et al. “Bulk and Surface Recombination Properties in Thin Film Semiconductors with Different Surface Treatments from Time-Resolved Photoluminescence Measurements”. en. In: *Scientific Reports* 9.1 (Mar. 2019), p. 5385. ISSN: 2045-2322. DOI: 10.1038/s41598-019-41716-x.

[95] Bart Vermang et al. “Development of Rear Surface Passivated Cu(In,Ga)Se2 Thin Film Solar Cells with Nano-Sized Local Rear Point Contacts”. en. In: *Solar Energy Materials and Solar Cells*. Dye Sensitized Solar Cells, Organic, Hybrid Solar Cells and New Concepts 117 (Oct. 2013), pp. 505–511. ISSN: 0927-0248. DOI: 10.1016/j.solmat.2013.07.025.

[96] Benjamin Bissig. “Micro- and Macroscopic Characterization of Recombination Losses in High Efficiency Cu(In,Ga)Se2 Thin Film Solar Cells”. en. Doctoral Thesis. ETH Zurich, 2018. DOI: 10.3929/ethz-b-000294337.

[97] Benjamin Bissig et al. “Surface Passivation for Reliable Measurement of Bulk Electronic Properties of Heterojunction Devices”. eng. In: *Small* 12.38 (Oct. 2016), pp. 5339–5346. ISSN: 1613-6829. DOI: 10.1002/smll.201601575.

[98] Sentaurus. ““Sentaurus Device User Guide.” p. Version P-2019.3”. en. In: (2019).

[99] Kihwan Kim et al. “Ag incorporation in low-temperature grown Cu (In, Ga) Se2 solar cells using Ag precursor layers”. In: *Solar Energy Materials and Solar Cells* 146 (2016), pp. 114–120.

[100] Yunxiang Zhang et al. “Silver surface treatment of Cu (In, Ga) Se2 (CIGS) thin film: a new passivation process for the CdS/CIGS heterojunction interface”. In: *Solar RRL* 4.10 (2020), p. 2000290.

[101] Chaojie Wang et al. “Wide bandgap CIGS thin films via Ag-PDT to ameliorate the interface quality of CIGS/CdS heterojunction”. In: *Journal of Materials Science: Materials in Electronics* 33.14 (2022), pp. 11055–11066.

[102] Lei Chen et al. "Secondary phase formation in (Ag, Cu)(In, Ga) Se2 thin films grown by three-stage co-evaporation". In: *Solar Energy Materials and Solar Cells* 166 (2017), pp. 18–26.

[103] Nicholas Valdes, JinWoo Lee, and William Shafarman. "Comparison of Ag and Ga alloying in low bandgap CuInSe2-based solar cells". In: *Solar Energy Materials and Solar Cells* 195 (2019), pp. 155–159.

[104] Kuo-Jui Hsiao et al. "Electrical impact of MoSe 2 on CIGS thin-film solar cells". In: *Physical Chemistry Chemical Physics* 15.41 (2013), pp. 18174–18178.

[105] Philipp Tonndorf et al. "Photoluminescence emission and Raman response of monolayer MoS 2, MoSe 2, and WSe 2". In: *Optics express* 21.4 (2013), pp. 4908–4916.

[106] Kostiantyn V Sopiha et al. "Thermodynamic stability, phase separation and Ag grading in (Ag, Cu)(In, Ga) Se 2 solar absorbers". In: *Journal of materials chemistry A* 8.17 (2020), pp. 8740–8751.

[107] VM Glazov, AS Pashinkin, and VA Fedorov. "Phase equilibria in the Cu-Se system". In: *Inorganic materials* 36 (2000), pp. 641–652.

[108] I Karakaya and William T Thompson. "The Ag-Se (silver-selenium) system". In: *Bulletin of Alloy Phase Diagrams* 11.3 (1990), pp. 266–271.

[109] Shih-Chi Yang et al. "Silver-Promoted High-Performance (Ag, Cu)(In, Ga) Se2 Thin-Film Solar Cells Grown at Very Low Temperature". In: *Solar RRL* 5.5 (2021), p. 2100108.

[110] Yi-Cheng Lin et al. "Residual stress in CIGS thin film solar cells on polyimide: simulation and experiments". In: *Journal of Materials Science: Materials in Electronics* 25.1 (2014), pp. 461–465.

[111] Shih-Chi Yang et al. "Efficiency boost of bifacial Cu (In, Ga) Se2 thin-film solar cells for flexible and tandem applications with silver-assisted low-temperature process". In: *Nature Energy* (2022), pp. 1–12.

[112] MD Heinemann et al. "The importance of sodium control in CIGSe superstrate solar cells". In: *IEEE Journal of Photovoltaics* 5.1 (2014), pp. 378–381.

[113] Mario Ochoa et al. "Lateral Charge Carrier Transport in Cu (In, Ga) Se2 Studied by Time-Resolved Photoluminescence Mapping". In: *physica status solidi (RRL)–Rapid Research Letters* 15.10 (2021), p. 2100313.

[114] Tokio Nakada, Yutaka Hirabayashi, and Takehito Tokado. "Cu (In1-x, Gax) Se2-based thin film solar cells using transparent conducting back contacts". In: *Japanese Journal of Applied Physics* 41.11A (2002), p. L1209.

[115] Jan Keller et al. “Bifacial Cu (In, Ga) Se2 solar cells using hydrogen-doped In2O3 films as a transparent back contact”. In: *Progress in Photovoltaics: Research and Applications* 26.10 (2018), pp. 846–858.

[116] Artorn Pokaipisit, Mati Horprathum, and Pichet Limsuwan. “Influence of oxygen flow rate on properties of indium tin oxide thin films prepared by ion-assisted electron beam evaporation”. In: *Sonklanakarin Journal of Science and Technology* 31.5 (2009), p. 577.

[117] Yang Ren et al. “The key of ITO films with high transparency and conductivity: Grain size and surface chemical composition”. In: *Journal of Alloys and Compounds* 893 (2022), p. 162304.

[118] Yu-Han Chang et al. “Insights from Transient Absorption Spectroscopy into Electron Dynamics Along the Ga-Gradient in Cu (In, Ga) Se2 Solar Cells”. In: *Advanced Energy Materials* 11.8 (2021), p. 2003446.

[119] Yan Jiang et al. “High-mobility In2O3: H electrodes for four-terminal perovskite/CuInSe2 tandem solar cells”. In: *ACS nano* 14.6 (2020), pp. 7502–7512.

[120] Abdurashid Mavlonov et al. “Superstrate-type flexible and bifacial Cu (In, Ga) Se2 thin-film solar cells with In2O3: SnO2 back contact”. In: *Solar Energy* 211 (2020), pp. 725–731.

[121] Takahito Nishimura et al. “Application of two-dimensional MoSe2 atomic layers to the lift-off process for producing light-weight and flexible bifacial Cu (In, Ga) Se2 solar cells”. In: *ACS Applied Energy Materials* 3.10 (2020), pp. 9504–9508.

[122] Abdurashid Mavlonov et al. “Effect of an Ohmic back contact on the stability of Cu (In, Ga) Se2-based flexible bifacial solar cells”. In: *Applied Physics Letters* 119.10 (2021), p. 103903.

[123] Naoto Hamada et al. “Fabrication of flexible and bifacial Cu (In, Ga) Se2 solar cell with superstrate-type structure using a lift-off process”. In: *Solar Energy* 199 (2020), pp. 819–825.

[124] Abdurashid Mavlonov et al. “Back-contact barrier analysis to develop flexible and bifacial Cu (In, Ga) Se2 solar cells using transparent conductive In2O3: SnO2 thin films”. In: *Solar Energy* 211 (2020), pp. 1311–1317.

[125] RW McClelland et al. “High-efficiency thin-film GaAs bifacial solar cells”. In: *IEEE Conference on Photovoltaic Specialists*. IEEE. 1990, pp. 145–147.

[126] Min Jeong Shin et al. “Bifacial photovoltaic performance of semitransparent ultra-thin Cu (In, Ga) Se2 solar cells with front and rear transparent conducting oxide contacts”. In: *Applied Surface Science* 535 (2021), p. 147732.

[127] Nicholas Cavallari et al. “Low temperature deposition of bifacial CIGS solar cells on Al-doped Zinc Oxide back contacts”. In: *Applied Surface Science* 412 (2017), pp. 52–57.

[128] Dongryeol Kim et al. “Flexible and semi-transparent ultra-thin CIGSe solar cells prepared on ultra-thin glass substrate: a key to flexible bifacial photovoltaic applications”. In: *Advanced Functional Materials* 30.36 (2020), p. 2001775.

[129] A Romeo et al. “Bifacial configurations for CdTe solar cells”. In: *Solar energy materials and solar cells* 91.15-16 (2007), pp. 1388–1391.

[130] Kamala Khanal Subedi et al. “Enabling bifacial thin film devices by developing a back surface field using CuxAlOy”. In: *Nano Energy* 83 (2021), p. 105827.

[131] S Marsillac, VY Parikh, and AD Compaan. “Ultra-thin bifacial CdTe solar cell”. In: *Solar energy materials and solar cells* 91.15-16 (2007), pp. 1398–1402.

[132] Elmar Lohmüller et al. “Towards 90% bifaciality for p-type Cz-Si solar cells by adaption of industrial PERC processes”. In: *2018 IEEE 7th World Conference on Photovoltaic Energy Conversion (WCPEC)(A Joint Conference of 45th IEEE PVSC, 28th PVSEC & 34th EU PVSEC)*. IEEE. 2018, pp. 3727–3731.

[133] H Ohtsuka et al. “Bifacial silicon solar cells with 21 · 3% front efficiency and 19 · 8% rear efficiency”. In: *Progress in Photovoltaics: Research and Applications* 8.4 (2000), pp. 385–390.

[134] A Moehlecke, I Zanesco, and A Luque. “Practical high efficiency bifacial solar cells”. In: *Proceedings of 1994 IEEE 1st World Conference on Photovoltaic Energy Conversion-WCPEC (A Joint Conference of PVSC, PVSEC and PSEC)*. Vol. 2. IEEE. 1994, pp. 1663–1666.

[135] Andreas Hübner, Armin G Aberle, and Rudolf Hezel. “Novel cost-effective bifacial silicon solar cells with 19.4% front and 18.1% rear efficiency”. In: *Applied physics letters* 70.8 (1997), pp. 1008–1010.

[136] Zhaoning Song et al. “Assessing the true power of bifacial perovskite solar cells under concurrent bifacial illumination”. In: *Sustainable Energy & Fuels* 5.11 (2021), pp. 2865–2870.

[137] Mehrdad Najafi et al. “Highly efficient and stable semi-transparent p-i-n planar perovskite solar cells by atmospheric pressure spatial atomic layer deposited ZnO”. In: *Solar Rrl* 2.10 (2018), p. 1800147.

[138] Hao Wang et al. “Bifacial, color-tunable semitransparent perovskite solar cells for building-integrated photovoltaics”. In: *ACS applied materials & interfaces* 12.1 (2019), pp. 484–493.

[139] Sangho Kim et al. “Over 30% efficiency bifacial 4-terminal perovskite-heterojunction silicon tandem solar cells with spectral albedo”. In: *Scientific Reports* 11.1 (2021), pp. 1–10.

[140] Michele De Bastiani et al. “Efficient bifacial monolithic perovskite/silicon tandem solar cells via bandgap engineering”. In: *Nature Energy* 6.2 (2021), pp. 167–175.

[141] Gianluca Coletti et al. “Bifacial four-terminal perovskite/silicon tandem solar cells and modules”. In: *ACS Energy Letters* 5.5 (2020), pp. 1676–1680.

[142] Jixian Xu et al. “Triple-halide wide–band gap perovskites with suppressed phase segregation for efficient tandems”. In: *Science* 367.6482 (2020), pp. 1097–1104.

[143] Marko Jošt et al. “Monolithic perovskite tandem solar cells: A review of the present status and advanced characterization methods toward 30% efficiency”. In: *Advanced Energy Materials* 10.26 (2020), p. 1904102.